Nonlinear Microscopy as a Tool for Histological Examinations

Alexei Kazarine

Doctor of Philosophy

Department of Chemistry

McGill University

Montréal, Québec

January 2019

A thesis submitted to McGill University

In partial fulfillment of the requirements for the degree of Doctor of Philosophy

Abstract

Histological analysis is a fundamental technique in modern medical diagnostics. In this thesis, we present novel imaging techniques based on nonlinear microscopy to provide a most needed update to classical histological methods, some of which were initially developed a hundred years ago. Nonlinear microscopy, a form of advanced laser scanning microscopy, enables three-dimensional imaging within tissue using multiple complementary nonlinear contrast mechanisms including multiphoton fluorescence, second harmonic generation (SHG) and third harmonic generation (THG) each with inherent optical sectioning capabilities. The technique can be applied to both labelled and unlabeled samples, allowing for greater flexibility.

This thesis first presents a new histological malaria detection method, third harmonic generation imaging scanning cytometry (THGISC). This technique is based on the combination of THG imaging, high speed motorized scanning and automated software processing. THG is a nonlinear optical process in which three incident photons interact with specific materials to combine into one photon that possesses the sum of their energies resulting in emission that is three times the incident light frequency. Hemozoin, a metabolic byproduct of the malaria parasite, has been shown to present a strong THG signal. We applied THGISC to lab-cultured parasites and malaria infected patient blood samples. We demonstrated that our technique is comparable in effectiveness to the gold standard of malaria detection by manual observation of Giemsa staining while significantly improving throughput thanks to rapid scanning and automated software-based parasitemia determination.

A novel multimodal approach for virtual histology of rabbit vocal folds by label-free nonlinear microscopy and nano computed tomography is presented to investigate vocal fold regeneration after injury. Traditionally, vocal fold histology was conducted through mechanical sectioning of tissue into thin slices and conventional histological staining of the slices. Our method enables us to visualize the tissue microarchitecture, particularly extracellular matrix elements such as collagen and elastin, which are critical for the proper functioning of vocal folds. We visualize collagen through SHG and elastin via two photon fluorescence; we are also able to observe other features of interest in whole vocal folds such as muscle, chondrocytes and blood vessels through two photon fluorescence. The resulting images were used to create detailed three-dimensional models of vocal fold tissue that can be computationally cross-sectioned in software for easy visualization.

Lastly, we investigate common histological dyes as THG harmonophores, enabling high resolution selective imaging of specific histological tissue features. We first verified the third order nonlinear susceptibility of hematoxylin within hematoxylin and eosin stained human skin and liver tissue sections, demonstrating highly selective nuclear staining by THG. We then identified two new THG harmonophores in common histological stains: Verhoeff-Van-Gieson and picrosirius red. We observe that the iron hematoxylin component of the Verhoeff stain acts as a selective THG harmonophore in tissue, binding to elastic fibers and nuclei. We also showed for the first time a significant nonlinear emission from picrosirius red, enabling highly specific, high contrast collagen detection by THG imaging.

The application of nonlinear microscopy to histological investigations provides powerful alternatives to conventional methods. The inherent optical sectioning capability of nonlinear microscopy extends histology into the third dimension while the multimodal approach allows for simultaneous visualization of structures of interest in both unlabeled tissue and through labelling with highly selective harmonophores. We anticipate that these techniques will be adopted in the future of modern biomedical diagnostics.

Résumé

L'analyse histologique est une technique fondamentale du diagnostic médical moderne. Dans cette thèse, nous présentons de nouvelles techniques d'imagerie basées sur la microscopie non linéaire pour apporter une mise à jour indispensable des méthodes histologiques classiques, dont certaines ont été développées il y a cent ans. La microscopie non linéaire, une forme de microscopie avancée à balayage laser, permet une imagerie tridimensionnelle dans un tissu en utilisant de multiples mécanismes de contraste non linéaires complémentaires, notamment la fluorescence multiphotonique, la génération de seconde harmonique (GSH) et la génération de troisième harmonique (GTH), chacun ayant une capacité intrinsèque de sectionnement optique. Cette technique peut être appliquée aux échantillons marqués et sans marqueur, permettant une plus grande flexibilité.

Cette thèse présente d'abord une nouvelle méthode de détection histologique du paludisme, la cytométrie de balayage par imagerie de la génération de troisième harmonique (CBIGTH). Cette technique repose sur la combinaison de l'imagerie par GTH, du balayage motorisé à grande vitesse et du traitement logiciel automatisé. La GTH est un processus optique non linéaire dans lequel trois photons incidents interagissent avec des matériaux spécifiques pour se combiner en un photon possédant la somme de leurs énergies, produisant une émission de lumière ayant une fréquence trois fois supérieure à celle de la lumière incidente. L'hémozoïne, un sous-produit métabolique du parasite du paludisme, s'est avéré présenter un fort signal de GTH. Nous avons appliqué la CBIGTH à des parasites cultivés en laboratoire et à des échantillons de sang obtenus de patients infectés par le paludisme. Nous avons démontré que l'efficacité de notre technique était comparable à celle de la détection du paludisme par l'observation manuelle de la coloration

au Giemsa tout en améliorant considérablement le rendement grâce au balayage rapide et à la détermination automatisée de la parasitémie basée sur logiciel.

Une nouvelle approche multimodale pour l'histologie virtuelle des cordes vocales de lapin par microscopie non linéaire sans marqueur et nano-tomodensitométrie est présentée afin d'étudier la régénération des cordes vocales après une blessure. Traditionnellement, l'histologie des plis vocaux était réalisée par sectionnement mécanique du tissu en fines tranches suivi de coloration histologique conventionnelle. Notre méthode nous permet de visualiser la microarchitecture tissulaire, en particulier les éléments de la matrice extracellulaire tels que le collagène et l'élastine, qui sont essentiels au bon fonctionnement des cordes vocales. Nous visualisons le collagène par GSH et l'élastine par fluorescence à deux photons; nous sommes également en mesure d'observer d'autres caractéristiques intéressantes dans des cordes vocales entières telles que le muscle, les chondrocytes et les vaisseaux sanguins grâce à la fluorescence à deux photons. Les images résultantes ont été utilisées pour créer des modèles tridimensionnels détaillés des plis vocaux pouvant être sectionnés par traitement informatique pour une visualisation aisée.

Enfin, nous étudions les colorants histologiques courants en tant qu'harmonophores de GTH, permettant une imagerie sélective à haute résolution de caractéristiques tissulaires histologiques spécifiques. Nous avons d'abord vérifié la sensibilité non linéaire de troisième ordre de l'hématoxyline dans les coupes de tissu humain de la peau et du foie colorées à l'hématoxyline et à l'éosine, démontrant une coloration nucléaire hautement sélective par la GTH. Nous avons ensuite identifié deux nouveaux harmonophores de GTH dans des colorants histologiques communs: Verhoeff-Van-Gieson et rouge picrosirius. Nous observons que le composant d'hématoxyline de fer de la coloration de Verhoeff agit comme un harmonophore de GTH sélectif

dans le tissu qui se lie aux fibres élastiques et aux noyaux cellulaires. Nous avons également montré pour la première fois une émission non linéaire significative du rouge picrosirius, permettant une détection hautement spécifique du collagène à contraste élevé par imagerie de GTH.

L'application de la microscopie non linéaire aux investigations histologiques fournit de puissantes alternatives aux méthodes conventionnelles. La capacité de sectionnement optique intrinsèque à la microscopie non linéaire étend l'histologie à la troisième dimension, tandis que l'approche multimodale permet la visualisation simultanée des structures d'intérêt dans les tissus non marqués et par marquage à l'aide d'harmonophores hautement sélectifs. Nous anticipons que ces techniques seront adoptées dans le futur du diagnostic biomédical moderne.

Statement of Originality

The author claims that the following aspects of the thesis constitute original scholarship and an advancement of knowledge. The author of this thesis contributed in all sample preparation, imaging and image analysis steps presented.

- Chapter 2 demonstrates the use of a new technique for malaria detection: third harmonic generation image scanning cytometry (THGISC), in the form of a published manuscript. This manuscript is the first use of this technique on cultured parasite samples and whole blood patient samples. The author conceptualized the technique, performed the thin blood smears, subsequent sample preparation for imaging (nuclear staining), nonlinear microscopy of the samples and wrote the code for the automated image analysis application. The author also performed image and data analysis and wrote the manuscript.
- Chapter 3 employs a novel approach to virtual histology of rabbit vocal folds utilizing nonlinear microscopy and nano computed tomography. The author designed and planned the experiments and performed the initial nonlinear microscopy experiments on rabbit vocal fold tissue (published in Kazarine et al, SPIE Proceedings Volume 10069, Multiphoton Microscopy in the Biomedical Sciences XVII; 100692E (2017)). The author also established the optical tissue clearing protocol used and conducted preliminary tissue clearing and nonlinear imaging experiments on thick vocal fold tissue slices. The author supervised the optical clearing of whole vocal fold tissue and its subsequent nonlinear imaging. The author performed 3D image analysis and rendering of the nonlinear microscopy and nano-computed tomography images for manuscript figures and wrote the manuscript. This manuscript has been submitted (December 2018).

- Chapter 4 identifies new THG harmonophores from common histological dyes and presents full multimodal nonlinear imaging for hematoxylin & eosin (H&E), Verhoff-Van-Gieson and picrosirius red stained human tissue sections. The author designed and planned the experiments and performed histological staining and nonlinear microscopy of the tissue sections.

Due to the interdisciplinary nature of biomedical research, most of the work presented here was completed in collaboration with other researchers.

- Chapter 2:

-Fadi Baakdah (Georges Lab, Institute of Parasitology, McGill University) cultivated the malaria parasites in packed red blood cells, synchronized the culture at different parasite lifecycle stages, fixed the culture and contributed to the writing of the manuscript.

-Dr. Angelica Gopal (Wiseman Lab, Department of Chemistry, McGill University) contributed to image and data analysis and writing of the manuscript.

-Prof. Wellington Oyibo (ANDI Centre of Excellence for Malaria Diagnosis, College of Medicine, University of Lagos, Nigeria) collected the patient blood samples, determined parasitemia in the field and contributed to the writing of the manuscript.

- Chapter 3:

-Ksenia Kolosova (Wiseman Lab, Department of Physics, McGill University) performed the optical tissue clearing and nonlinear imaging of whole rabbit vocal folds under the supervision of

the author and prepared samples for nano-computed tomography, which she conducted with the technician who operated the instrument.

-Dr. Angelica Gopal (Wiseman Lab, Department of Chemistry; Mandl Lab, Department of Physiology; McGill University) contributed to establishing the optical tissue clearing methodology used and performed the initial tissue clearing experiments of thick sections of rabbit vocal fold alongside the author. Dr. Gopal also advised in 3D image analysis and rendering of nonlinear microscopy images and contributed to the writing of the manuscript.

-Huijie Wang (Li-Jessen Lab, School of Communication Sciences and Disorders; Mongeau Lab, Department of Mechanical Engineering; McGill University) dissected the rabbit tissue for sample preparation.

-Dr. Rui Tahara (Redpath Museum, McGill University) performed the sample preparation for nano-computed tomography and subsequent nano-computed tomography experiments of rabbit vocal fold tissue.

-Dr. Almoaidbellah Rammal (Kost Lab, Department of Otolaryngology, McGill University) performed vocal fold surgery on the rabbit.

-Prof. Luc Mongeau and Prof. Nicole Li-Jessen contributed to the writing of the manuscript.

- Chapter 4:

-Dr. Angelica Gopal (Wiseman Lab, Department of Chemistry; Mandl Lab, Department of Physiology; McGill University) contributed to conceptualizing the experiments and performed histological staining alongside the author.

Acknowledgements

This thesis is the culmination of several years of new experiences, skills, friends and microscopes. First, I would like to express my deepest gratitude to my supervisor, Dr. Paul Wiseman, who dared to take me on as his student. Without his support, guidance and resources, this PhD would not have been possible. He encouraged me to take on challenging interdisciplinary collaborations and promoted an independent research environment for young students to explore biophotonics, biophysics and everything in between from the depths of a chemistry department. His infinite supply of stories provided endless amusement during my PhD and I will always admire his remarkable networking skills.

I offer my heartfelt thanks to my best friend in the Wiseman Lab, Dr. Vincent Rouger, who threw me headfirst into the realm of optics and mentored me through many microscopes, optical tables and pallets. I will always appreciate our office conversations and beers, as well as the time we spent putting together countless microscopy setups and aligning all sizes of lasers. I am very glad that our arrivals in the Wiseman Lab coincided, and that I was able to do the majority of my PhD with you in the lab.

Thank you to Melissa Wong for your hard work during your undergraduate summer project. I had a blast introducing you to your first CNC mill and teaching you CAD. I would like to thank Timothy Toplak for introducing me to cold caffeinated beverages after group meeting, in addition to his friendship and wisdom. I thank all the Wiseman group members, past and present, whom I had the pleasure of working with, especially Dr. Sarah Aufmkolk, who brought endless enthusiasm and science knowledge into our office.

I also thank the Verdi V18 for surviving at least until the end of my PhD, and the Coherent service team. I acknowledge funding during my PhD from an FRQNT Doctoral Scholarship, which allowed me to focus on science and research.

I would like to thank Fadi Baakdah for his patience and expertise in culturing malaria parasites, without whom my foray into malaria detection would not have been possible. I thank all my other collaborators for their hard work in our interdisciplinary projects, particularly Neda Latifi, Dr. Sarah Bouhabel, Dr. Nicole Li-Jessen and Dr. Luc Mongeau for introducing me to the challenging world of vocal fold regeneration.

I thank my Masters' supervisor, Dr. Eric Salin, who introduced me to research and teaching. I learned a lot from you while you were at McGill and I will always cherish the time I was in your lab and the experiences I gained there. I thank Dr. Sam Sewall for being an awesome supervisor during my TAships and letting me demonstrate CHEM 367/377 instrumental analysis undergraduate teaching labs for countless semesters.

I express my gratitude to the staff of the Chemistry department, especially Chantal Marotte, the graduate studies coordinator, who guided me through both of my graduate degrees at McGill.

I would like to thank my best man, Rufino Ansara, for being a source of unwavering support for the past 20 years. I thank Timothy Mack for being my friend and colleague since the start of our McGill journey nearly 10 years ago. We have come a long way since our programming class in 2009. I thank Dr. Erika Wee, Dr. Erin Templeton, Patricio Artusa and Amanda Fiore for their friendship.

My deepest thanks to my family: my parents, Alexei and Lioudmila, and my sister, Alice, for their love and support during my studies. I would also like to thank my in-laws: Allan and Brigitte Gopal, as well as my brother-in-law, Dr. Alan Gopal, for their support and encouragement during my PhD.

Finally, I would like to give my eternal love and gratitude to my wife and partner-in-crime, Dr. Angelica Gopal, who has supported me unconditionally throughout my graduate studies. Your presence by my side during long days and nights of research has been a constant source of motivation. This thesis would not have been possible without you. Thank you for your patience, understanding, and love. You are the light of my life.

Table of Contents

List of Figures

List of Abbreviations

2D: two-dimensional

3D: three-dimensional

ACT: artemisinin-based combination therapy

AO: acridine orange

AP: alkaline phosphatase

BA: benzyl alcohol

BB: benzyl benzoate

CARS: coherent anti-Stokes Raman spectroscopy

CLSM: confocal laser scanning microscopy

Cryo-SEM: cryogenic scanning electron microscope

CT: computed tomography

CW: continuous wave

DAPI: 4′,6-diamidino-2-phenylindole

DFG: difference frequency generation

DM: dichroic mirror

DNA: deoxyribonucleic acid

DPE: diphenyl ether

E: eosin

EGFP: enhanced green fluorescent protein

EM: electron microscopy

GUI: graphical user interface

H&E: hematoxylin & eosin

H: hematoxylin

HRP: horseradish peroxidase

IHC: immunohistochemistry

IR: infrared

LP: long pass

MBF: malaria blood film

MPF: multiphoton fluorescence

MRI: magnetic resonance imaging

NA: numerical aperture

Nano-CT: nano computed tomography

NM: nonlinear microscopy

OCT: optimal cutting temperature compound

OPO: optical parametric oscillator

PDMS: polydimethylsiloxane

PMT: photomultiplier

PTA: phosphotungstic acid

RBC: red blood cell

RDT: rapid diagnostic test

SHG: second harmonic generation

SP: short pass

SRS: stimulated Raman scattering

TEM: transmission electron microscopy

THG: third harmonic generation

THGISC: third harmonic generation image scanning cytometry

TPAF: two photon autofluorescence

TPF: two-photon fluorescence

VF: vocal fold

Voxel: volume element

VVG: Verhoeff-Van-Gieson

WHO: World Health Organization

1 Introduction

1.1 Motivation

Histology, the study of tissue using microscopy, is a fundamental pillar of modern medicine. From its use in basic biomedical sciences to histopathology performed by anatomical pathologists for the diagnosis of disease, histology has been widely used since its introduction in the 1800s. Despite technological advances in lasers and microscopy, manual histological analysis using colored dyes and an optical microscope remains a gold standard for tissue analysis. Better alternatives must be developed for histology to evolve into a modern environment, improving not only throughput and accuracy but also expanding it to the realm of three-dimensional structural information.

1.2 Conventional Histology

1.2.1 Definitions

The anatomical study of tissue is critical both for the understanding of normal physiology as well as disease conditions. To set the stage for an in-depth discussion of histology, it is important to define common terminology used in the field, which is regularly used interchangeably in the literature. Histology itself is typically defined as the microscopic study of tissue[1]. Along with it comes the concept of histopathology, the histological study of diseased tissues, which is often performed to establish a medical diagnosis. While histopathology is performed by a medical professional, the pathologist[2], the tissue sample is extensively processed for this purpose by histologists, who are also referred to as histotechnologists[3]. In the interest of maintaining clarity within this thesis, the word histology will from now on be used to refer to the technical aspects of the microscopic study of tissue, from tissue collection to observation.

1.2.2 Introduction to Histological Methods

The establishment of the field of histology is traditionally attributed to Marie Francois Xavier Bichat[4] in the 1700s, who enumerated 21 different tissue types in the human body through gross observation of cadavers without a microscope[5]. However, it was Johannes Müller[6], a German physiologist, who first promoted the use of the microscope for the structural study of cancer in tissue in 1836[7].

While technological progress has sped up histological processing, the basic principles on which the method was founded remain mostly unchanged[3]. The final goal of histology is to obtain and stain a representative thin section of the tissue that can be visualized under an optical microscope.

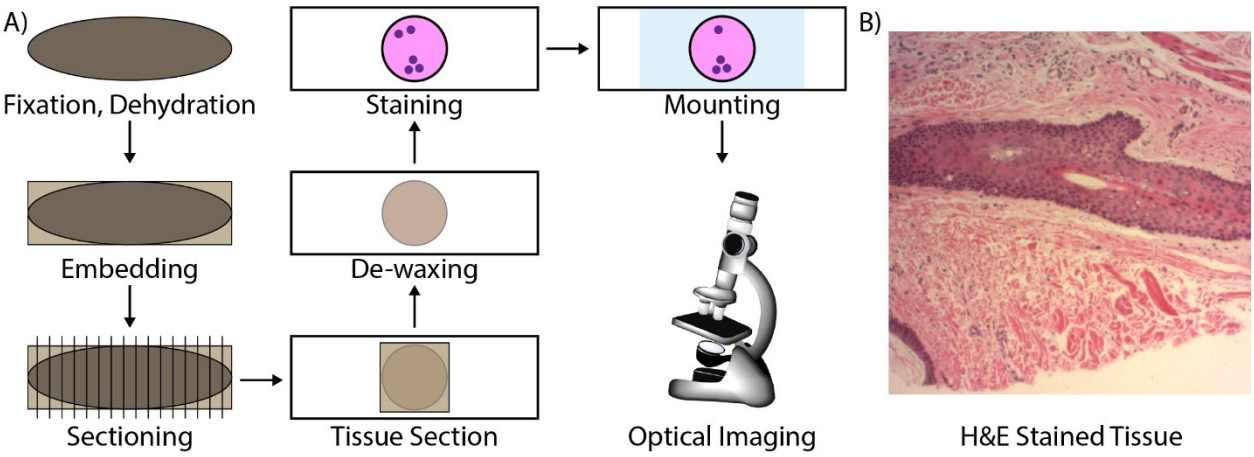

Figure 1-1: A) Summary of conventional histological preparation steps. B) Example image of hematoxylin & eosin stained human skin tissue.

The process of histology can be separated into the fixation, dehydration, embedding, sectioning, mounting, staining and optical imaging steps, which are summarized on Figure 1-1A[8]. First, the tissue sample is chemically fixed to prevent degradation after collection. This can be done either by a crosslinking fixative[9] (typically an aldehyde such as formaldehyde or glutaraldehyde), which creates covalent bonds between different proteins in the tissue, or by a precipitation fixative[10]

(typically an alcohol such as methanol or ethanol), which denatures proteins in the sample and causes them to precipitate and aggregate. The selection of fixative primarily depends on the tissue features that are of interest, since neither method perfectly preserves all tissue elements equally.

After fixation, the tissue must be embedded in a medium before sectioning[11]. Embedding facilitates the slicing process by providing the tissue with a mechanical support while also helping preserve the tissue morphology. As embedding is conventionally done using paraffin wax, an additional dehydration step is necessary to remove the water content of the tissue and replace it with xylene, which is miscible with melted paraffin. The dehydration step is commonly accomplished by sequential passages in water and ethanol solutions leading up to 100% ethanol, followed by passage into xylene. Embedding is then achieved by passing the sample into melted paraffin until it is fully infiltrated.

Sectioning of the paraffin embedded tissue is accomplished by a tool called a microtome[12], which allows microscopic slicing in equal increments, typically 5 or 10 μm. After sectioning, the tissue slice is immediately placed on a glass slide. Since tissue elements provide poor native contrast for light microscopy, the sample must be stained with a colorful dye to highlight components of interest. Since most stains developed for this purpose are water based, a de-paraffining step and rehydration step are then performed using once again xylene and ethanol/water passages. The tissue sample is then stained by dipping into the required solutions before being placed into xylene once again for dehydration, allowing the tissue to retain the acquired water-soluble dyes. The sample is finally mounted using a permanent, solvent based mounting medium and a cover slip. The thin section of tissue is then ready for observation with light microscopy.

An alternative approach that is used to prepare histological slides for more advanced visualization techniques involves the use of cryogenic sectioning instead of paraffin[13]. After fixation, the tissue is embedded in a cryostable medium (also known as optimal cutting temperature compound[14] or OCT), quickly frozen using liquid nitrogen and sectioned in a cryostat while frozen. While this approach allows for faster processing and preserves certain antigens better than paraffin embedding, there is a significant risk of freezing artifacts.

1.2.3 Common Histological Stains

A variety of histological stains have been developed to visualize different aspects of tissue. Most of these stains exploit chemical interactions between the dyes utilized and specific tissue components. By far, the most commonly used stain is the Hematoxylin (H) and Eosin (E) (H&E) stain, which is used as a gold standard in medical diagnosis by histopathology[15]. This stain allows pathologists to differentiate between nucleated cells and other tissue components, which is critical for diagnosing diseases such as cancer.

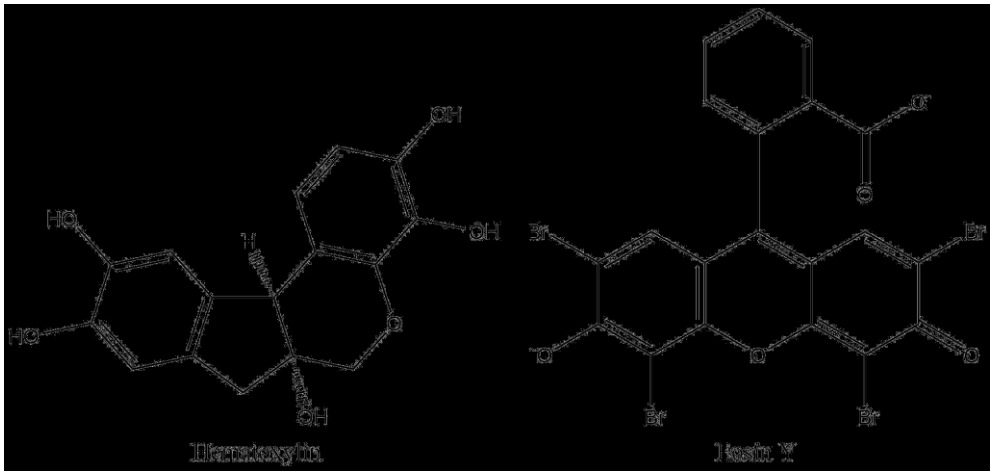

Figure 1-2: Chemical structures of hematoxylin and eosin Y.

Hematoxylin (Figure 1-2) is a natural product extracted from the logwood tree[16]. Through referred to as hematoxylin in the stain name, the active dye material is hematein, the oxidized form of hematoxylin. However, as hematein is not stable in long term and continues to oxidize, the stain solutions typically incorporate hematoxylin with an oxidizing agent to perform the conversion to hematein in situ[17]. By itself, hematein serves little purpose in histology. To bind to tissue, it requires a mordant, a metal ion that serves as a binding intermediary between the tissue and the dye. In the H&E stain, an aluminum salt based mordant is used to create a dye lake with hematein, resulting in a complex called hemalum[18]. It is this complex that binds strongly to the chromatin in the cell nucleus. While it has been theorized that the binding partner is deoxyribonucleic acid (DNA) in the nucleus, evidence has shown that hemalum continues to bind to the chromatin even after DNA extraction, suggesting the presence of other negatively charged binding partners[19]. The result of hemalum staining is a purple/violet coloring of all cell nuclei in the tissue.

To provide contrast to the (H) component, the tissue is counterstained with eosin[20], an acidic, negatively charged dye which stains positively charged components, namely intracellular and extracellular proteins. This results in the cytoplasm and extracellular materials of the tissue being stained in pink. There are two similar molecules that are commonly referred to as eosin: eosin y (Figure 1-2) and eosin b, with eosin y being the most commonly used variant in histology. An example of an H&E stained human skin section can be found on Figure 1-1B.

Other mordants have been used in combination with hematein to produce stains that target other tissue components than simply cell nuclei. The Verhoeff stain[21] uses an iron mordant in the form of ferric chloride in combination with iodine to create an iron-hematein-iodine complex, which binds strongly to elastin, a protein found as part of elastic fibers in the extracellular matrix. As a

result, elastic fibers are stained black while cell nuclei are colorized in brown due to weaker, less specific binding. While the Verhoeff stain predominantly binds to elastin, it has also been shown to bind to myelin sheaths[22]. Its counterstain, the Van Gieson stain[23], utilizes a mixture of picric acid and acid fuchsin to color collagen fibers and cell cytoplasm in red and yellow, respectively. The resulting compound stain, Verhoeff-Van Gieson, is the most common stain used in the histopathology of elastic tissue disorders, as it provides the ability to distinguish between elastic and collagen fibers[24]. While this stain uses acid fuchsin for highlighting collagen, a popular alternative for the same purpose is picrosirius red[25]. Developed as a more stable alternative to acid fuchsin, it provides an effective method for histopathology of collagen disorders thanks to its vivid red staining of collagen in the tissue[26].

Another regularly used hematein complex is Weigert's hematoxylin, which is popularly utilized as part of Masson's Trichrome stain[27]. Weigert's hematoxylin is also an iron-hematein complex but unlike the Verhoeff stain, no iodine is utilized and the concentration of the iron-hematein lake is significantly lower. As such, this solution does not appear to stain elastic fibers but instead produces acid-resistant nuclear staining. In the Masson's Trichrome stain, it is used to pre-stain the cell nuclei in black. before other counterstain solutions containing acid fuchsin, xylidine ponceau, phosphomolybdic acid and light green SF stain are used to colorize muscle fibers in red, collagen in green, cytoplasm in pink. Although the exact mechanisms behind each component are not fully understood, the resulting Trichrome stain is used to distinguish different forms of connective tissue from the cells in the tissue.

As blood is a critical component of the organism, histological stains have been developed to differentiate the various cells present in it, such as the Romanowsky stain along with its variants (Wright, Giemsa and Leishman stains)[28]. These hematological stains allow hematopathologists to distinguish between red blood cells, white blood cells, platelets as well as parasites such as the malaria *Plasmodium* parasite. Instead of paraffin embedding, blood is processed in the form of smears, which are fixed in methanol before staining.

Although the stains presented in this chapter form the most common ones used in pathology laboratories, there are many more other histological stains available to histology professionals, each with its staining specificity for a given application[29].

1.2.4 Optical Microscopy

The development of the optical microscopy long predated that of histopathology. The first compound microscope is credited to Hans Jansen and his son Zacharias in 1595[30]. In 1665, Robert Hooke published a book entitled "Micrographia", in which he detailed his observations of insects, plants and manmade objects using a microscope, which was the first manuscript of its kind. Through his work, Hooke invented the word "cell" to describe the microscopic pores he saw in cork tissue, which reminded him of the cells of a Christian monastery. Progress in microscopy continued with Anthony van Leeuwenhoek, who created single-lens, single use microscopes with higher quality lenses in 1670[6]. However, it was only during the 19th century that microscope development reached a new level of achievement thanks to the collective work of Carl Zeiss, Otto Schott and Ernst Abbé, who achieved the invention of apochromatic lenses and objectives with which they made high quality compound microscopes. These accomplishments provided

microscopes with significant improvements in image resolution and fostered the use of microscopy in biology, bringing microscopy and histology together.

Sample observation in modern histology is still typically conducted using a compound light microscope (Figure 1-3). In the standard configuration commonly referred to as upright, the light source (lamp) is placed below the stage and is directed by a condenser lens onto the slide containing the sample[31]. A uniform illumination field is generated using a Kohler illumination configuration, in which the image of the microscope light source is perfectly defocused at the sample[32]. The light transmitted through the sample is collected by the objective lens and directed to the eyepiece or to a camera through a tube lens, though manual observation is typically the norm in histopathology. This method is also commonly known as brightfield microscopy. The use of transmitted light as a contrast method requires very thin samples as the entire sample is illuminated axially at the same time. Imaging of thicker samples results in significant out-of-focus blur which renders observation impractical.

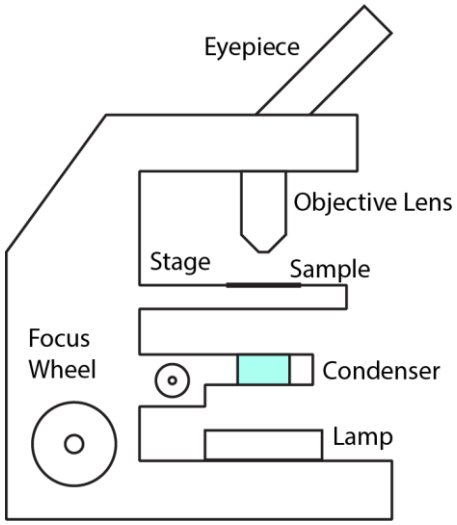

Figure 1-3: Schematic of an upright compound optical microscope.

The choice of objective lens enables the observer to determine both the observable field size (magnification of the objective) and the maximum resolution available (numerical aperture (NA)) required for their needs. The highest resolution obtainable with a light microscope is limited by the diffraction of light within the lens system[32]. For standard objective lenses with circular apertures, this diffraction results in the spread of light originating from a single point in the sample plane into a disk shape surrounded by concentric rings in the focal plane which was first described by Airy[33]. The diameter of the Airy disk created from a point source of light is measured from the disk center to the first minimum of the Airy pattern and can be obtained using equation 1-1:

$$d = 1.22\frac{\lambda}{2NA} \tag{1-1}$$

Where d is the diameter of the Airy disk, λ is the wavelength of the light and NA is the numerical aperture of the lens system.

The numerical aperture is the capacity of the lens system to collect light, and can be calculated using equation 1-2:

$$NA = n \cdot sin(\theta)(2) \tag{1-2}$$

Where n is the refractive index of the medium surrounding the lens and θ is the half-angle that subtends the cone of light that can be collected or emitted by the lens. As such, the greatest achievable resolution in light microscopy requires objectives with a high numerical aperture and a high refractive-index immersion medium, and short wavelength for illumination light.

1.2.5 Drawbacks of Conventional Histology

While classical histological has enjoyed a long and productive history as a gold standard for histopathological analysis, it presents several drawbacks. First, each step of tissue processing required to obtain tissue sections is a long and labor-intensive process, with fixation steps sometimes requiring overnight time periods. In addition, tissue sectioning inherently only presents a two-dimensional (2D) slice of information regarding the tissue structure. As organs and tissues inherently exist in a three-dimensional (3D) layout, histologists are required to subjectively determine which projections to take during sectioning to ensure representative sampling. Finally, while colored stains provide a wealth of information about the tissue, they are not an ideal solution for distinguishing tissue components and require significant professional training to be properly interpreted by pathologists. In summary, there is a scientific need for new histological methods to be developed that address one or more of these drawbacks by providing automated approaches that enable full 3D histology without requirement for sectioning and with better specificity than the chemistry of dye-mordant-tissue binding.

1.3 Alternative Histological Methods

1.3.1 Electron Microscopy

The histological observation of subcellular organelles requires a resolution beyond that offered by optical microscopy. Electron microscopy (EM) remedies this issue by using electrons instead of photons as an illumination source[34]. Through the particle-wave duality, electrons can act as waves with very short de Broglie wavelengths when accelerated by electromagnetic fields. According to equation 1-1, a shorter wavelength significantly reduces the diameter of the diffraction pattern produced by the imaging process. The much finer spatial resolution offered by EM has not only

allowed the imaging of the ultrastructure of cells but also that of viruses and other biological materials that cannot be visualized under standard light microscopy[35].

The basic form of the technique is transmission electron microscopy (TEM)[36], in which an electron beam is accelerated and directed through an ultrathin section of material. Certain areas of the sample will scatter the incoming electrons, while others remain transparent to the illumination. The electrons that are transmitted through the sample are then magnified by an objective lens system and directed to a fluorescent phosphor screen. The fluorescence can then be captured by a digital camera to record the final image. Conceptually, the setup of the TEM is actually very similar to that of an inverted light microscope, but with the use of electromagnetic lenses instead of optical materials to guide the electron beam. The entire setup must be placed under vacuum as otherwise the electrons would interact with molecules in the air.

Electron microscopy requires different tissue sample preparation methods due to the different properties of electrons[37-39]. First, the tissue must be sectioned even thinner (≤ 1um) than for optical microscopy due to electrons being scattered more easily than photons. This procedure requires special microtomes along with a different embedding material than paraffin wax. Tissue embedding for EM is typically accomplished using epoxy resins[40]. Metal grids are used to support the sample during the imaging process, instead of microscope slides, as the electron beam cannot penetrate thick glass. Proper fixation of subcellular components is critical for electron microscopy, so fixation using glutaraldehyde is preferred over the conventional formaldehyde as it achieves better preservation of intercellular proteins. For visualization, different kinds of histological stains, typically consisting of heavy metals, must be utilized to absorb or scatter electrons and create image contrast[41].

Clinical applications of electron microscopy include the histology of the kidney for the investigation of glomerular and tubular diseases, tumor histology to differentiate tumor cell origin and identification of viruses, along with other applications in the histology of liver, muscle and nerve cell tissue[42]. The latest development for biological EM is the cryogenic scanning electron microscope (Cryo-SEM), in which samples can be imaged without dehydration through prior vitrification of the aqueous content with liquid nitrogen. Cryo-SEM allows for significantly less damage to the biological sample during the imaging process, while presenting fewer sample preparation steps than convention EM[43].

1.3.2 X-ray Nanotomography

A modern approach to histology involves the use of x-ray nanotomography, also known as nano computer tomography or Nano-CT[44]. In this technique, a sample is illuminated with x-rays and rotated to obtain cross sections in every direction that are then mathematically mapped on a computer to obtain a tomograph[45]. The resulting tomograph allows three-dimensional volume rendering of the sample, while maintaining an isometric submicron^3 volume element (voxel) size. While the method utilizes the same concept as traditional medical computer tomography, technological advances have allowed nanotomography to obtain much finer submicron resolution through a combination of geometric magnification and optical magnification after scintillation[46].

Nanotomography generates contrast based on tissue density, which can be a problem for soft tissue observation where native contrast is insufficient. This contrast can then be enhanced through staining with agents such as phosphotungstic acid, which provides a larger density contrast[47]. An alternative option is the use of phase-retrieval tomography which does not require additional staining steps[48]. Differentiation of tissue types can be conducted either through the use

of antibody-conjugated metal staining agents[49] or through advanced image segmentation based on machine learning methods[50].

The great advantage of nanotomography is the ability to obtain three-dimensional structural information of large tissue samples while maintaining high resolution in the axial and lateral dimensions. By utilizing volume analysis software, pathologists could conduct "virtual histology" by selecting their own cross sections of the virtual model without the need for mechanical sectioning[51]. Modern nano-CT instruments are capable of imaging objects in the cm size range, which allows them to accommodate typical biopsy sizes easily, though imaging of such samples with the highest resolution possible would require significant time. With continuous development, nanotomography could potentially supplant conventional histology, provided that the issue of tissue differentiation is properly addressed.

1.3.3 Immunohistochemistry

Immunohistochemistry (IHC), also known as immunolabelling, was developed to address the lack of selectivity in conventional histological staining[52]. Immunolabelling uses the intrinsic specificities of the immune response to foreign bodies. As part of the immune response, antibodies are generated by immune cells. These antibodies target pathogens by binding to specifically recognized epitopes on the surface of the pathogen. To generate antibodies for IHC, immune cells are exposed to a specific antigen (the target protein) and subsequently isolated for culture. These immune cells are fused with a myeloma tumor cell line to produce hybridoma cells[53]. The hybridoma cells can be cultured indefinitely to produce antibodies that bind specifically to a single epitope.

By using protein specific antibodies that are coupled to a reporter, IHC allows direct visualization of the spatial distribution of the targeted proteins in tissue that the antibodies bind. Direct immunolabelling uses primary antibodies conjugated to a reporter, while indirect immunolabelling uses a primary antibody to bind to the epitope of interest and a secondary antibody conjugated to a reporter which in turn binds specifically to the primary antibodies. Indirect IHC provides a more flexible approach since the secondary antibody is typically specific to a species (i.e. anti-rat, anti-goat, etc.), such that one secondary antibody can be used with multiple primary antibodies. In addition, multiple secondaries can bind to a single primary, which increases the sensitivity of detection due to signal amplification.

In traditional IHC, the reporter is usually an enzyme such as horseradish peroxidase (HRP) or alkaline phosphatase (AP). These reporters are chromogenic as the enzyme label can react with a substrate to generate an intensely colored product. As such traditional IHC is visualized using a light microscope.

An alternative approach is immunohistofluorescence[54], more commonly known as immunofluorescence, where the antibody is conjugated to a fluorescent reporter dye. Immunofluorescence is known to be more sensitive than traditional IHC as it uses fluorescence microscopy to detect proteins of interest with high sensitivity.

1.4 Fluorescence Microscopy

1.4.1 Principles of Fluorescence

Fluorescence is a physical luminescent phenomenon resulting from light-matter interactions. In the first step of the fluorescence cycle, a photon of excitation light is rapidly (10^{-15} s) absorbed by a fluorescent molecule, promoting an electron to an excited singlet state (S_1)[55].

The electron then undergoes nonradiative relaxation (10^{-12} s) to the lowest vibrational level of the excited electronic state, where it remains until it relaxes back to the singlet ground state (S_0) through the emission of a fluorescence photon (10^{-9} s) (this assumes a fluorescence relaxation pathway and not other possible relaxation paths). This entire process is illustrated in a Jablonski energy level diagram in Figure 1-4. The nonradiative energy loss in the excited state leads to a wavelength red shift in the emission spectrum in comparison to the absorption spectrum, which is called the Stokes shift. A similar slower phenomenon, phosphorescence, can occur when the electron undergoes a spin-forbidden intersystem crossing from the excited singlet state (S_1) to the triplet state (T_1). Emission of a phosphorescence photon happens when the electron relaxes from the T_1 to the S_0 state (10^{-4} -10^{-1} s). A molecule capable of fluorescence is commonly called a fluorophore.

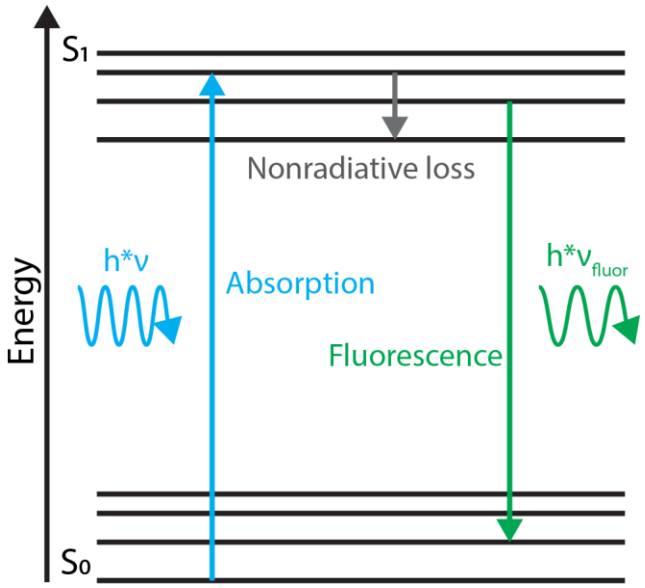

Figure 1-4: Jablonski energy diagram of the fluorescence process.

The emission efficiency of a fluorescent molecule, also known as its quantum yield, is defined as the ratio of the number of photons emitted to the number of photons absorbed. In fluorescence imaging applications, higher quantum yield reporters are advantageous as samples can be imaged at lower excitation power. At higher illumination power, fluorophores can undergo photochemical destruction or permanent inactivation in a process known as photobleaching. This limits the use of certain reporters in fluorescence microscopy such that only photostable fluorophores with higher quantum yields can be used for long term imaging applications[56].

Fluorescence microscopy has become a vital tool in biological imaging since it provides a method of visualizing only select components in a sample against a dark background through control of excitation and emission spectra and detection direction relative to excitation light path[57].

1.4.2 Fluorescence Labelling

While some compounds have innate fluorescent properties owing to their conjugated ring systems, i.e. tryptophan and quinine[58], the detection of non-fluorescent biomolecules is highly desirable. As such, methods have been developed to label non-fluorescent species with fluorescent reporters[59]. One commonly used method is immunofluorescence which was discussed in the previous section. Briefly, the technique labels the biological molecule of interest with fluorescently tagged antibodies. Immunofluorescence reporters commonly consist of organic dyes[60] and quantum dot nanoparticles[61]. An alternative labelling modality is the use of genetically encoded fluorescent proteins such as enhanced green fluorescent protein (EGFP) expressed in cells or transgenic animals[62, 63].

1.4.3 Widefield Fluorescence Microscopy

Histological analysis by immunofluorescence is performed using a fluorescence microscope. The purpose of this instrument is to illuminate a uniform field of the sample with excitation light of a specific wavelength, thereby exciting fluorophores within the sample. Fluorescence emission is subsequently collected, usually back through the same objective lens, filtered and detected.

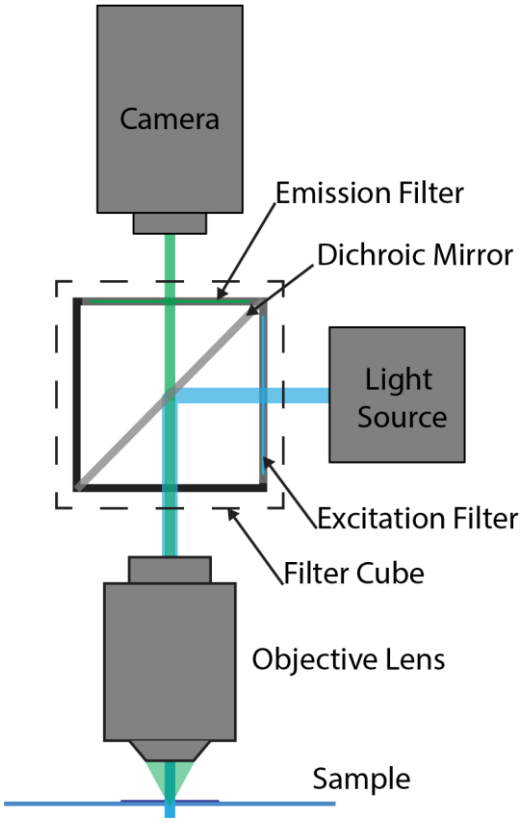

Figure 1-5: Schematic layout of a widefield fluorescence microscope.

The basic setup of a fluorescence microscope (Figure 1-5), commonly known as widefield, begins with a high intensity light source that is directed towards an excitation filter. This filter is used to select an excitation wavelength to excite a specific fluorophore within the sample. The filtered excitation light is reflected into the objective by a dichroic mirror. The objective projects uniform illumination onto the sample, which excites the fluorescent moieties present within the tissue sample resulting in the emission of fluorescence into 4π. The emission is collected in an epi (from

Greek "the same") configuration by the same objective and directed towards an emission filter that blocks any scattered excitation light. The filtered Stokes shifted fluorescence emission light passes through the dichroic mirror towards an eyepiece for direct visualization or through a tube lens into a camera for image detection. To simplify the wavelength selection process, the dichroic mirror and emission and excitation filters are typically combined in a filter cube, which can be easily swapped out to visualize different fluorescent labels.

While widefield fluorescence microscopy presents a significant evolution over brightfield light microscopy used in conventional histology, it presents some limitations. In widefield microscopy, the entire field of view is illuminated axially simultaneously, which presents a significant out-of-focus background for thicker samples. For histological samples, this still requires the tissue to be sectioned into thin slices to avoid this effect. In addition, due to the diffraction limit previously discussed, the resolution of the fluorescence image is determined by the emission wavelength. As this wavelength is redshifted due to energy losses, this results in a lower resolution as determined by equation 1-1. Fortunately, some of these drawbacks were reduced thanks to the development of confocal fluorescence microscopy.

1.4.4 Confocal Microscopy

Confocal laser scanning microscopy (CLSM) is one of the most widely used analytical techniques in the life sciences[64]. In a confocal microscope, a laser light source is focused by the objective to a single diffraction limited spot that is laterally raster scanned over the entire sample to sequentially excite and pointwise image fluorescent molecules in different regions of the sample[65]. The introduction of a pinhole in the detection light path enables the selective imaging of a thin axial plane, spatially filtering out-of-focus fluorescence from adjacent planes (Figure 1-6). This permits

optical sectioning of the sample without the need for mechanical sectioning. At each location along the raster scan path, an image "pixel" is recorded whose intensity is based on the detected fluorescence intensity at that location. These pixels are then assembled to create an image of the sample, as demonstrated in Figure 1-7.

Confocal microscopy addresses several of the drawbacks of widefield fluorescence microscopy. First, the use of a pinhole significantly improves the axial resolution of the image, enabling visualization of larger histological tissue samples, although the overall imaging depth is still limited by the scattering of excitation light typically experienced in thick tissue samples. In addition, the lateral resolution in confocal microscopy is based on the size of the diffraction limited excitation beam. As the excitation wavelength is blue-shifted in comparison to the emission wavelength, CLSM results in improved lateral resolution compared to widefield fluorescence. The raster scanning process further enables the user to determine the spatial sampling frequency, allowing for a rapid overview to identify areas of interest that can then be imaged in detail at the highest possible resolution.

While confocal microscopy has revolutionized biomedical research by providing a powerful tool for the study of biological molecules and their interactions in cells, its usefulness in histology is still limited to mechanically sliced tissue with a thickness of 10-100 μm[66]. Beyond this thickness, the excitation light is destructively scattered, resulting in aberrations and significant loss of fluorescence signal. To conduct histology directly on larger sections of tissue, an evolution of this technique was necessary. Fortunately, this need was addressed by the development of multiphoton microscopy, also known as nonlinear microscopy[67].

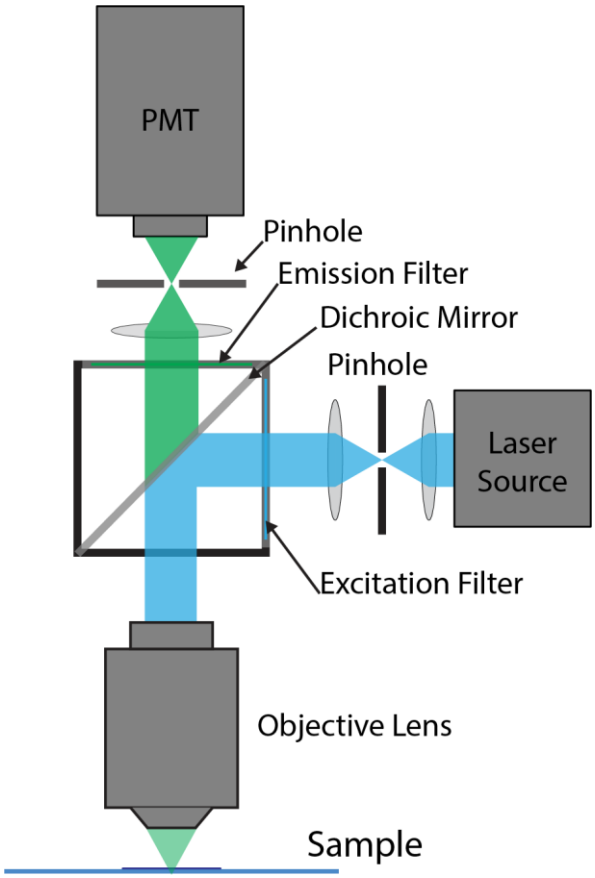

Figure 1-6: Layout of a confocal laser scanning microscope.

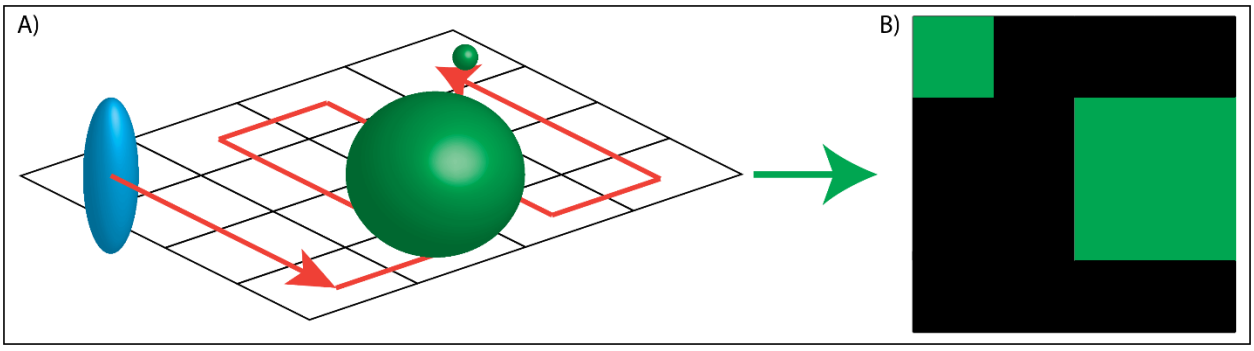

Figure 1-7: Principle of laser scanning microscopy. A) Raster scanning of laser beam across sample. Spheres represent two different sized fluorescent features. B) Schematic pixelated image built from raster scan.

1.5 Nonlinear Microscopy

Nonlinear microscopy is an extension of laser scanning microscopy where the contrast is derived through nonlinear optical interactions that occur as an ultrafast pulsed near-infrared laser beam is raster scanned over the sample. While similar to CLSM in concept, nonlinear microscopy presents inherent advantages that render it decidedly useful for histological applications. First, nonlinear microscopy offers several contrast mechanisms such as second harmonic generation (SHG), third harmonic generation (THG) and multiphoton fluorescence (MPF), which can be used simultaneously to obtain complementary structural information about the sample. While MPF can be used to visualize fluorescently labelled targets just as in confocal microscopy, it can also be applied in a label-free manner due to the wide variety of natively fluorescent proteins in biological tissues that can be excited by multiphoton absorption[68]. Combined with SHG and THG imaging, which do not require any form of labelling, multiphoton microscopy enables label-free tissue histology.

Another significant advantage of nonlinear microscopy is the reduced scattering of the longer wavelength near-infrared illumination, which can penetrate deeper into tissue samples. As tissue scatters and absorbs infrared light significantly less than visible wavelengths, the excitation light can be used focused into thicker samples of up to 1 mm[69]. When combined with adaptive optics, greater imaging depths have been achieved, including imaging of live mouse brain through the skull[70].

An inherent effect of nonlinear excitation is the intrinsic optical sectioning that occurs due to the characteristic low probability of nonlinear optical effects outside of the focal volume (Figure 1-8). As such, excitation and emission from nonlinear processes only occur at the focal plane of the laser beam where the photon density is the highest. This allows easy three-dimensional scanning of samples without the use of a confocal pinhole. The inherent absence of out of plane excitation also makes nonlinear microscopy an excellent tool for deep live tissue imaging as it reduces the impact of the laser light on tissue above and below the focal plane.

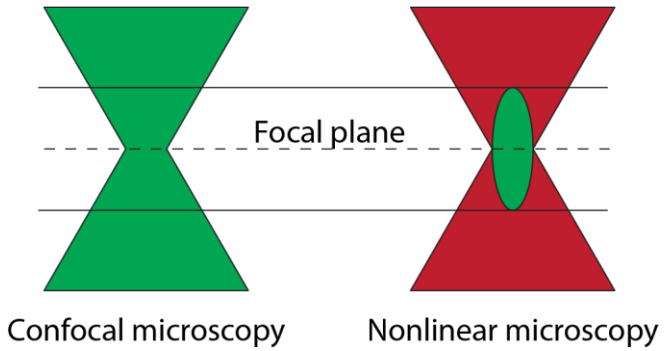

Figure 1-8: Comparison of optical sectioning between confocal and nonlinear microscopy. Green represents the excited volume of fluorophores within a sample. In confocal microscopy, fluorophores along the entire beam path within the sample are excited. The confocal pinhole restricts detection to a narrow volume surrounding the focal plane. In nonlinear microscopy, only fluorophores at the focal plane are excited. Red represents the infrared laser profile where photon density is too low for multiphoton excitation.

Overall, these features make nonlinear microscopy an excellent tool for histological examinations, as it combines high resolution, three-dimensional imaging with a variety of contrast mechanisms that highlight different tissue components. The following sections will introduce both nonlinear optics and the specific nonlinear optical effects used as contrast mechanisms in nonlinear microscopy. In addition, applications of nonlinear microscopy to biomedical problems will be discussed.

1.5.1 Nonlinear Optics

The interaction of light and matter has classically been characterized through the polarization density induced by the electric field of light on the electron density of molecules inside the material. These induced electric dipoles begin to oscillate alongside the applied field, resulting in an overall polarization of the material. When the applied electric field has a small magnitude, the polarization density is linearly related to incident electric field strength:

$$P(t) = \chi \varepsilon_0 E(t) \tag{1-3}$$

Where P is the number of induced dipoles per unit volume, ε_0 is the electric (permittivity) constant and χ is the linear electric susceptibility characteristic of the material. This linear response can be used to describe the basic interactions of light and matter (e.g. absorption, scattering, reflection and refraction) that we witness every day under normal illumination sources such as sunlight.

However, the linear polarization response becomes saturated when a significant electric field is applied, resulting in the occurrence of nonlinear optical effects. The existence of such phenomena was first predicted by Maria Goeppert-Mayer[71] in 1931, who theorized the possibility of two-photon absorption. However, practical experimentation with nonlinear optics was only made possible by the invention of the ruby laser by Maiman[72] in 1960, which granted scientists access to much higher optical field intensities. The ruby laser allowed Franken[73] to discover second harmonic generation in a slab of quartz in 1961[73], opening the door to the field of modern nonlinear optics. Since then, nonlinear optics have been used in a variety of applications, ranging from materials science[74] to biomedical imaging[75].

Nonlinear polarization can be generalized by using a power series approach to equation 1-3 to separate possible field interactions.

$$P_t(t) = \varepsilon_0[\chi^{(1)}E(t) + \chi^{(2)}E(t)E(t) + \chi^{(3)}E(t)E(t)E(t) + \cdots] \quad (1\text{-}4)$$

Where $\chi^{(1)}$ represents the linear susceptibility, $\chi^{(2)}$ and $\chi^{(3)}$are the second and third order nonlinear susceptibilities respectively, and $E(t)$ represents the incident electric fields, which may either come from a monochromatic source or a mixture of different frequency sources. In this form, the polarization $P_t(t)$ and the electric fields $E(t)$ are assumed to be scalars as this provides a simpler presentation of nonlinear polarization. The vector nature of both polarization and vector fields can be addressed by a more rigorous tensor-based analysis[76]. However, for clarity, such a treatment will not be presented here.

Nonlinear optical effects can be separated into two categories: parametric and nonparametric. In a parametric process, the initial and final quantum states of atoms and molecules in the optical material are the same. As such these processes do not result in the exchange of energy with the material and they occur via extremely short lived virtual state transitions. Examples of parametric processes include second harmonic generation[73], third harmonic generation[77], sum-frequency generation[78] and difference-frequency generation[79]. In contrast, a non-parametric process induces a change between the initial and final quantum states of atoms/molecules in the optical material, resulting in excitation from a real energy state to another real state using energy from the incident electric field. An example of a non-parametric process is multiphoton fluorescence. In general, a medium that is capable of nonlinear optical effects is termed a nonlinear optical material.

1.5.2 Second Harmonic Generation

During second harmonic generation (SHG), two incident photons are annihilated and combined into one through interaction with the nonlinear optical material. Photons are emitted from the material that are exactly twice the optical frequency (or half the wavelength) of the photons in the incident beam, resulting in conservation of energy. Figure 1-9 shows the Jablonski energy diagram describing this process, where the dashed energy states are virtual states that do not correspond to any real energy state within the material.

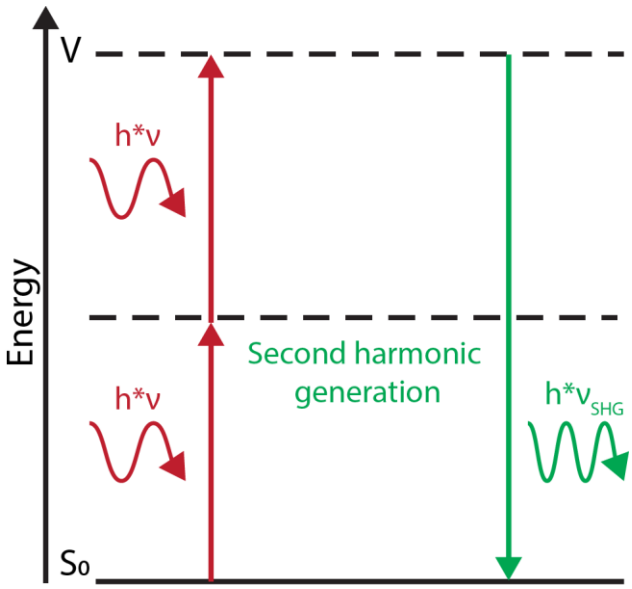

Figure 1-9: Jablonski energy diagram of the second harmonic generation process. Dashed lines represent virtual states

The process of second harmonic generation is described in equation 1-5 whereas the time-varying electric field of the incident laser beam described through Euler's method is presented in equation 1-6.

$$P_2(t) = \varepsilon_0 \chi^{(2)} E^2(t) \tag{1-5}$$

$$E(t) = Ee^{-i\omega t} + E^* e^{i\omega t} \tag{1-6}$$

By substituting equation 1-6 into equation 1-5, we obtain:

$$P_2(t) = \varepsilon_0 \chi^{(2)} E E^* + \varepsilon_0 \chi^{(2)} \left(E^2 e^{-i2\omega t} + (E^*)^2 e^{i2\omega t} \right) \quad (1\text{-}7)$$

From equation 1-7, we can observe two terms that vary as $2\omega t$ that describe the process of second harmonic generation. The first term of the equation does not result in any light generation since it does not present any time varying components. Subsequently, upon differentiation with respect to time, the first term becomes zero.

The selection rules for second harmonic generation requires that a medium does not possess inversion symmetry for emission. If inversion symmetry is present, as E(t) changes sign during oscillation, P_2 must follow and change sign as well for this process to occur. However, due to the quadratic nature of the E^2dependency displayed in equation 1-5, the sign change cannot occur unless $\chi^{(2)} = 0$, where the medium does not have second order nonlinear susceptibility.

Fortunately, this selection rule enables the imaging of highly selective non-centrosymmetric tissue components such as collagen fibers and muscle fibers, with a high signal to noise ratio against a quasi-nonexistent background. As collagen is the most abundant protein in tissue,[80] SHG offers an incredibly convenient way for the visualization and study of collagen in disease[81]. In addition, lipophilic probes have been designed that take advantage of SHG properties to selectively highlight cell membranes[82, 83]. As SHG is a parametric effect, it does not result in any energy transfer into the sample, which allows minimally perturbative long-term imaging without photobleaching if no non-parametric processes occur.

1.5.3 Third Harmonic Generation

Third harmonic generation is a third order nonlinear optical effect that combines three incident photons of identical energy to form a single output photon at three times the frequency (or one third of the wavelength). The Jablonski energy diagram of this process is shown in Figure 1-10. The process of THG can be described by the following equation:

$$P_3(t) = \varepsilon_0 \chi^{(3)} E^3(t) \tag{1-8}$$

The substitution of equation 1-6 into equation 1-8 results in equation 1-9.

$$P_3(t) = \varepsilon_0 3\chi^{(3)}\left(E^2 E^* e^{-i\omega t} + E(E^*)^2 e^{i\omega t}\right) + \varepsilon_0 \chi^{(3)}\left(E^3 e^{-3i\omega t} + (E^*)^3 e^{3i\omega t}\right) \tag{1-9}$$

The first term of this equation presents nonlinear polarization components that have the same frequency (ω) as the original incident electric field. These components represent another important third order nonlinear optical effect: self-lensing through intensity dependent refractive index changes[76]. The second term that varies with $3\omega t$ describes the process of third harmonic generation.

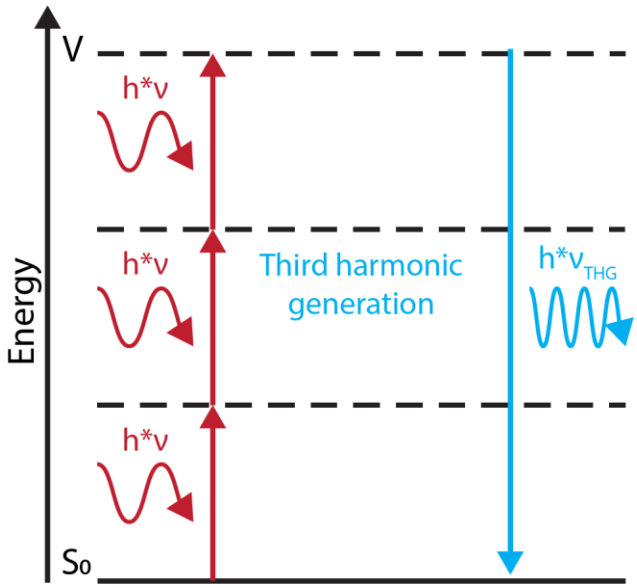

Figure 1-10: Jablonski energy diagram of the third harmonic generation process. Dashed lines represent virtual states.

Unlike SHG, which requires non-centrosymmetric media, THG can theoretically occur in all media, thanks to the E^3 term enabling it to follow sign changes in symmetric media. However, in nonlinear microscopy where a gaussian laser beam is used to excite the sample, THG emission from isotropic media is not possible due to the Gouy phase shift that occurs when focusing a gaussian beam through an objective[84].

Contrary to plane waves, gaussian beams present a progressive phase slippage along the optical axis of π radians on passing through the focal point[85]. This phase shift invalidates the phase-matching conditions between the fundamental and the third order harmonic, resulting in absence of emission from isotropic samples.

However, the Gouy phase shift can be disturbed on passing through certain interfaces, which permits THG emission to occur[84]. These interfaces can be either between tissue components having different refractive indices or different $\chi^{(3)}$ values[86]. In tissue, the difference in refractive index occurs mainly in the form of water/lipid interfaces, making THG a useful tool for visualizing lipid-heavy components. As such, lipid bodies in liver tissue[87], myelin[88], and cell membranes during embryo development[89] have been studied in a label-free manner. In addition, bone and other mineralized tissue interfaces provide good THG contrast[90]. As THG is also a parametric effect, imaging can be conducted long-term with minimal photodamage.

THG emission can also be significantly enhanced if one of the virtual transition states closely coincides with a real electronic energy state in the material, increasing the third order nonlinear susceptibility of the material. This is particularly useful if the resonance occurs at the two-photon level (the second virtual state). If the resonance occurs at the one-photon transition, the incident electric field experiences significant linear absorption that can result in photodamage. Similarly, if

the resonance occurs at the three-photon transition, the material-generated electric field experiences linear absorption and reduced efficiency[76].

We have previously used this resonance mechanism to observe high THG emission in hemozoin, a digestive byproduct of the malaria parasite within red blood cells[91, 92]. The same mechanism has also been observed for hemoglobin in red blood cells[93], as well as hematoxylin, a histological dye[94].

1.5.4 Multiphoton Fluorescence

Two photon excitation fluorescence is a non-parametric nonlinear optical effect where two photons are nearly simultaneously absorbed by the material, which excites an electron in the fluorophore from the ground singlet state (S_o) to an excited singlet state (usually S_1). This is followed by nonradiative loss to the lowest excited state and Stokes' shifted emission as previously described in the single photon fluorescence section.

As the relaxation pathway after absorption is identical to the case of single photon fluorescence, the two-photon fluorescence emission spectrum of a fluorescent moiety is also identical. However, the excitation spectrum of two photon absorption can be significantly different due to differences in accessible transitions between one and two photon absorption for symmetrical molecules[95]. The Jablonski diagram explaining two photon fluorescence is shown in Figure 1-11.

As two-photon fluorescence is a non-parametric process, it is subject to the photobleaching limitations of single photon fluorescence microscopy. However, it still provides intrinsic optical sectioning as the nonlinear absorption only occurs within the focus where photon densities are sufficiently high, and due to infrared excitation wavelengths, it has deeper tissue penetration which is critical for the imaging of large tissue samples.

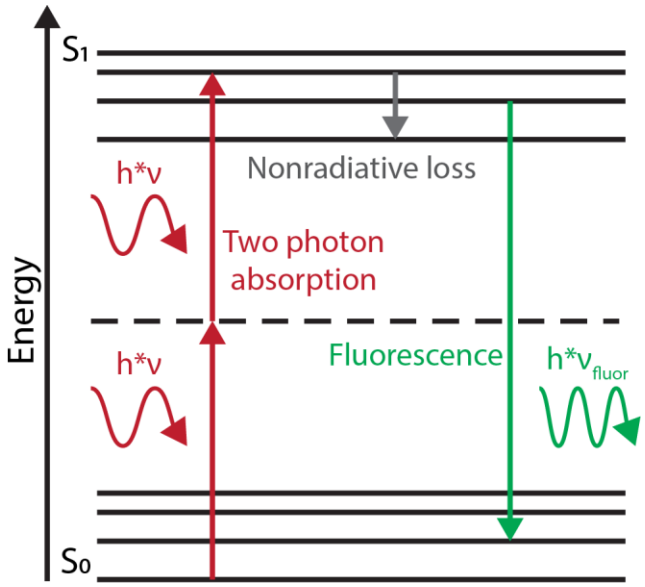

Figure 1-11: Jablonski diagram of the two-photon fluorescence process. Dashed line represents a virtual electronic state.

Another advantage of two-photon fluorescence is that the two-photon cross section of many fluorophores is much broader, resulting in the simultaneous excitation of several dyes/fluorescent proteins with the same excitation laser, minimizing imaging time and simplifying the microscope[95]. This capability is also very useful for the label-free imaging of intrinsic fluorescent molecules, such as elastin, NADH, retinol, flavins and tryptophan, in tissues[68, 96-98].

While this section has described two photon fluorescence, the same nonlinear excitation concept can also be extended to three photon fluorescence, allowing even deeper imaging into tissue thanks to the higher excitation wavelengths required for this process. Three photon fluorescence has been used for in vivo imaging of drosophila brain[99], zebrafish brain[100] as well as mouse intestine[101] and mouse brain[70, 102, 103].

1.5.5 Ultrafast Laser Sources

As discussed previously in this chapter, nonlinear microscopy requires electric fields strengths far beyond those offered by conventional light sources. Lasers used for confocal microscopy provide continuous wave (CW) low intensity emission that is more than sufficient for single photon excitation. However, pulsed lasers are required to efficiently induce nonlinear optical effects as they provide low energy pulses that have a high instantaneous peak power[104]. This allows nonlinear imaging to be conducted without the significant risk of photodamage by high power CW lasers. To achieve the highest peak power available, a laser pulse must have the shortest duration possible for the same pulse energy as dictated by the time-energy uncertainty principle. Practically, this is accomplished with short duration femtosecond (fs) pulses using a process called mode-locking[105]. The lasers that can generate such pulses are classified as ultrafast lasers. In modern systems, mode locking is achieved through Kerr-lens mode-lock[106], a $\chi^{(3)}$ nonlinear optical effect previously described in the THG section of this chapter as self-lensing.

The traditional and most popular ultrafast source for nonlinear microscopes is the titanium:sapphire (Ti:Sapphire) laser[107]. This laser has a wide excitation bandwidth, providing many longitudinal oscillation modes that can be mode-locked together to obtain femtosecond pulses[105]. However, the emission bandwidth tunability of commercial Ti:Sapphire lasers is limited between 700 and 1000 nm, which limits its usefulness for THG imaging. At an excitation wavelength of 1000 nm, the THG emission would occur in the ultraviolet region around 333 nm and light of this wavelength is often absorbed by standard glass optical materials such as lenses and objectives[108]. As such, laser sources that are further into the infra-red are more useful for THG imaging. In addition, such sources enable deeper multiphoton imaging through longer wavelength two photon and three photon excitation due to a reduction in scattering in tissues.

Optical parametric oscillators[109] (OPO) are devices used to extend the wavelength of existing ultrafast laser sources, such as Ti:Sapphire lasers[110]. OPOs use another nonlinear optical effect, difference-frequency generation[85] (DFG), which utilizes a nonlinear crystal to parametrically split incoming photons (pump beam) into two lower energy photons with longer wavelengths, as demonstrated in Figure 1-12A. The higher energy beam is then amplified through resonant oscillation in the device (Figure 1-12B) and is termed "the signal". The other lower energy beam, called "the idler", is typically not retained by the cavity mirrors. While initial pumping of the OPO provides spontaneous DFG to produce the signal and idler wavelengths, the conversion efficiency is extremely weak, and the emitted power is usually insufficient for practical applications.

To significantly amplify the signal wavelength, the OPO provides a return path for the signal beam towards the crystal to permit oscillation. The return path is designed such that the signal pulse arrives back to the crystal at the same time as the next pump pulse, a condition called synchronous pumping[111]. At this point, the simultaneous presence of both pump and signal pulses causes parametric amplification of the signal pulse at the expense of the pump. The parametric oscillation process requires a minimum pump power to occur, which can be decreased by using different cavity designs that also retain the idler component[112]. Wavelength tuning of the signal and idler beams is typically accomplished by adjusting the cavity length, altering the synchronous pumping conditions[111].

Until recently, most nonlinear imaging research has been conducted with a combination of Ti:Sapphire lasers and OPOs[113]. However, new technologies have reduced the cost and increased the efficiency of ultrafast nonlinear microscopy sources. In modern instrumentation, the Ti:Sapphire laser has been replaced by a more robust ytterbium based pump directly integrated

with the OPO as a single box design, allowing for imaging laser sources with computer controlled tunable emission from 660-1320 nm[114]. Ultrafast fiber lasers have also been developed as cost-efficient single wavelength sources for microscopy[115]. An alternate novel approach is the use of a nonlinear crystal fiber to generate supercontinuum pulses, which are wide band ultrafast pulses capable of exciting multiple nonlinear effects simultaneously[116].

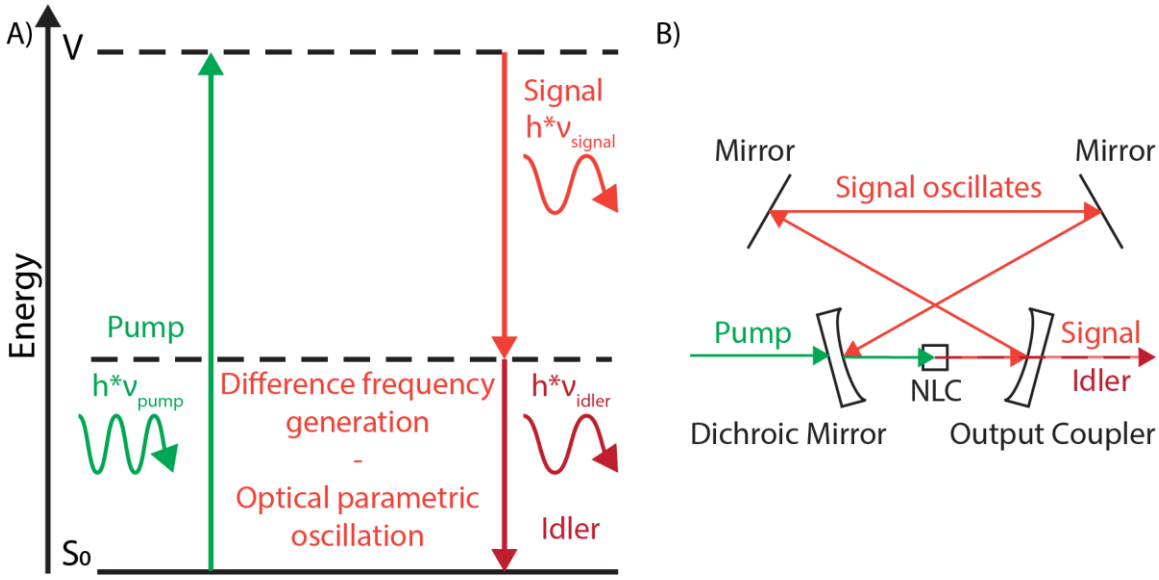

Figure 1-12: A) Jablonski energy diagram of difference frequency generation process. Dashed lines represent virtual states. B) Schematic of an optical parametric oscillator. NLC: nonlinear crystal.

1.5.6 The Nonlinear Microscope

The first nonlinear microscope for two photon imaging was built by Denk et al. in 1990[117]. The imaging setup for a nonlinear microscope is essentially the same as for a confocal microscope, with three key differences. Firstly, the laser source is near-infrared, typically an ultrafast laser capable of delivering femtosecond pulses. Secondly, no pinhole is required for detection due to the inherent intensity dependent restriction of nonlinear optical effects to the beam focus. Finally, the detection of parametric phenomena (i.e. SHG/THG) requires forward collection, as these effects are coherent and are primarily emitted along the direction of the excitation beam. As such,

while the objective focuses the laser beam on the sample, the emitted SHG and/or THG light is collected by a condenser in a trans-detection setup. The light is then separated into spectral channels and point detected by photomultipliers. A schematic of our nonlinear microscope set-up is shown in Figure 1-13. Due to the use of IR lasers in combination with forward detection, it is important to incorporate an IR blocking filter after the collection condenser, so that no IR laser light reaches the detectors.

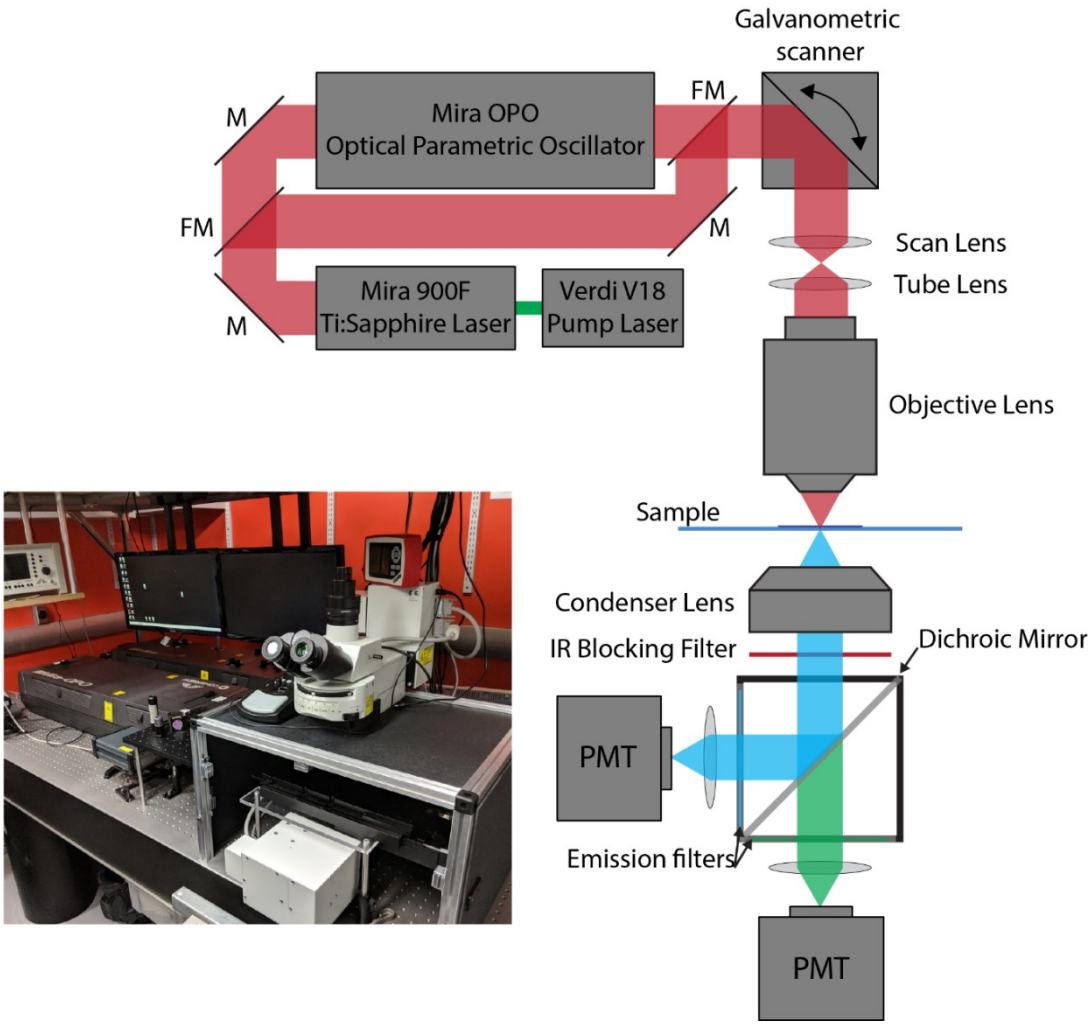

Figure 1-13: Layout of our nonlinear microscope equipped for forward detection of SHG and THG photons. A 532 nm laser (Verdi V18) pumps a Ti:Sapphire laser (Mira 900F), which in turn pumps an optical parametric oscillator (Mira OPO). Switching between the Ti:Sapphire laser and the OPO as excitation sources is accomplished through motorized flip mirrors (FM). Inset shows photograph of the setup. M: mirror

1.6 Nonlinear Microscopy Applied to Histology

Nonlinear microscopy has been previously applied to histological samples using two photon fluorescence (TPF), second harmonic generation (SHG) and third harmonic generation (THG). Other nonlinear optical effects applied to histological imaging include sum frequency generation[118], coherent anti-Stokes Raman spectroscopy (CARS)[119] and stimulated Raman scattering (SRS)[120].

Two photon fluorescence has been used to investigate intratissue elastic fibers[121], targeted imaging of cancer cells using gold nanorods[122], the effects of sickle cell disease on hemoglobin[123] and the placental membrane microarchitecture[124] amongst a vast array of biomedical applications. While the histological applications of two photon fluorescence often involve both auto fluorescence imaging alongside targeted fluorescence labelling, we have chosen to use examples that highlight the label-free possibilities of the technique.

In contrast, most of the published second harmonic generation imaging applications focus on the structure of collagen in various tissues along with some muscle and microtubule visualizations. Collagen modulation in tumors[125] has been characterized by SHG along with microtubule assemblies in native brain tissue[126], living cardiac myocytes[127], and the collagen microstructure in interstitial pneumonia[128], scarring processes[129] and mechanical strain of rat tail tendon[130].

Third harmonic generation has enabled the label-free imaging of intra-tissue elastic fibers[131], myelin in the central nervous system[88], human brain tumors[132] in addition to investigating stored blood[133]. It has often been combined with the previously described two photon contrast mechanisms to form a multimodal approach to image complex biological structures such as the human cornea[75], atherosclerotic lesions[134] and Alzheimer's disease brain samples[135].

Most recently, sum frequency generation and SRS have been used to study mouse[118] and human Meibomian glands[136], respectively. CARS has been utilized as a histopathological tool to study vibrationally detected cancer markers[137]. In addition, new instruments incorporating all the previously described modalities for nonlinear histopathological imaging have been demonstrated[116, 138, 139]. These applications highlight the flexibility granted by label-free multimodal nonlinear microscopy systems for various histological examinations.

1.7 Thesis Objective

The primary objective of this thesis is the development and application of new nonlinear microscopy techniques to study histology in various systems. The work presented in this thesis focuses on two photon fluorescence along with second and third harmonic generation imaging. These modalities are applied separately and in combination to the histological analysis of tissue and cells.

1.8 Thesis Outline

In this thesis, we implement nonlinear microscopy approaches to study tissue histology, initially as a label free modality and lastly as an alternative visualization modality for conventional histological dyes.

In Chapter 2, we utilize third harmonic generation microscopy to develop a new malaria detection technique, third harmonic generation image scanning cytometry (THGISC). The method uses a combination of third harmonic generation (THG) microscopy, high speed motorizing scanning and automated image processing to simultaneously count patient red blood cells and highlight malaria parasites inside infected cells by the significantly enhanced THG emission from hemozoin,

a metabolic byproduct of the parasite. This method provides an easy label-free determination of parasitemia in whole blood while using only a single detection channel.

Chapter 3 presents a new multimodal approach for the virtual histology of rabbit vocal folds using a combination of label-free nonlinear microscopy (TPF/SHG) and nano computed tomography. As an alternative to conventional histology, which requires mechanical sectioning and staining with histological dyes, our approach enables the creation of detailed virtual models of the vocal folds, which can be computationally cross sectioned using software for convenient and flexible visualization. The two methods provide complementary structural information, which is a promising avenue to investigate wound healing.

Chapter 4 explores the use of common histological dyes as third harmonic generation tissue markers. We characterize the nonlinear response of three histological stains using human skin and liver tissue sections and report the novel utilization of Sirius Red as a third order harmonophore. We also visualize the TPF and SHG of these tissue stains to study the overlap between the different modalities.

Finally, Chapter 5 summarizes the conclusions of the work presented and the future directions for this research.

1.9 References

1. Musumeci, G., Past, present and future: overview on histology and histopathology. *Journal of Histology and Histopathology* **2014,** *1* (1).
2. Lester, S. C., *Manual of Surgical Pathology E-Book*. Elsevier Health Sciences: 2010.
3. Titford, M., A Short History of Histopathology Technique. *Journal of Histotechnology* **2013,** *29* (2), 99-110.
4. Shoja, M. M.; Tubbs, R. S.; Loukas, M.; Shokouhi, G.; Ardalan, M. R., Marie-Francois Xavier Bichat (1771-1802) and his contributions to the foundations of pathological anatomy and modern medicine. *Ann Anat* **2008,** *190* (5), 413-20.
5. Bichat, X.; Coffyn, C.; Calvert, G., *General Anatomy: Applied to Physiology and the Practice of Medicine*. 1824.
6. Hussein, I. H.; Raad, M., Once Upon a Microscopic Slide: The Story of Histology. *Journal of Cytology & Histology* **2015,** *06* (06).
7. Muller, J., On the Nature and Structural Characteristics of Cancer: General Observations on the Minute Structure of Morbid Growths. *CA: A Cancer Journal for Clinicians* **1973,** *23* (5), 307-312.
8. Gartner, L. P., *Textbook of Histology E-Book*. Elsevier Health Sciences: 2015.
9. Hopwood, D., Fixatives and fixation: a review. *Histochem J* **1969,** *1* (4), 323-60.
10. Noguchi, M.; Furuya, S.; Takeuchi, T.; Hirohashi, S., Modified formalin and methanol fixation methods for molecular biological and morphological analyses. *Pathol Int* **1997,** *47* (10), 685-91.
11. Dey, P., Basic and Advanced Laboratory Techniques in Histopathology and Cytology. Springer.

12. Atkins, A. G.; Vincent, J. F. V., An Instrumented Microtome for Improved Histological Sections and the Measurement of Fracture-Toughness. *J Mater Sci Lett* **1984,** *3* (4), 310-312.

13. Slot, J. W.; Geuze, H. J., Cryosectioning and immunolabeling. *Nat Protoc* **2007,** *2* (10), 2480-91.

14. Fischer, A. H.; Jacobson, K. A.; Rose, J.; Zeller, R., Cryosectioning tissues. *CSH Protoc* **2008,** *2008* (8), pdb prot4991.

15. Fischer, A. H.; Jacobson, K. A.; Rose, J.; Zeller, R., Hematoxylin and eosin staining of tissue and cell sections. *CSH Protoc* **2008,** *2008*, pdb prot4986.

16. Titford, M., The long history of hematoxylin. *Biotech Histochem* **2005,** *80* (2), 73-8.

17. Horobin, R. W.; Kiernan, J. A., *Conn's biological stains: a handbook of dyes, stains and fluorochromes for use in biology and medicine*. BIOS Scientific Publishers: 2002.

18. Llewellyn, B. D., Nuclear staining with alum hematoxylin. *Biotech Histochem* **2009,** *84* (4), 159-77.

19. BAKER, J. R., Experiments on the Action of Mordants 2. Aluminium-Haematein. *Journal of Cell Science* **1962,** *s3-103* (64), 493-517.

20. Bruce-Gregorios, J. H., *Histopathologic techniques*. JMC Press Inc: Quezon City, Philippines: , 1974.

21. Verhoeff, F. H., Some New Staining Methods of Wide Applicability. *Journal of the American Medical Association* **1908,** *L* (11), 876-877.

22. Puchtler, H.; Waldrop, F. S., On the mechanism of Verhoeff's elastica stain: a convenient stain for myelin sheaths. *Histochemistry* **1979,** *62* (3), 233-47.

23. Van Gieson, J., Laboratory notes of technical methods for the nervous system. *New York Med J* **1889,** *50*, 57-60.

24. Kazlouskaya, V.; Malhotra, S.; Lambe, J.; Idriss, M. H.; Elston, D.; Andres, C., The utility of elastic Verhoeff-Van Gieson staining in dermatopathology. *J Cutan Pathol* **2013,** *40* (2), 211-25.

25. Junqueira, L. C.; Bignolas, G.; Brentani, R. R., Picrosirius staining plus polarization microscopy, a specific method for collagen detection in tissue sections. *Histochem J* **1979,** *11* (4), 447-55.

26. Nielsen, L. F.; Moe, D.; Kirkeby, S.; Garbarsch, C., Sirius red and acid fuchsin staining mechanisms. *Biotech Histochem* **1998,** *73* (2), 71-7.

27. Suvarna, K. S.; Layton, C.; Bancroft, J. D., *Bancroft's Theory and Practice of Histological Techniques E-Book*. Elsevier Health Sciences: 2018.

28. Culling, C. F. A.; Allison, R.; Barr, W., *Cellular pathology technique*. Elsevier: 2014.

29. Kiernan, J. A., Classification and naming of dyes, stains and fluorochromes. *Biotech Histochem* **2001,** *76* (5-6), 261-78.

30. Croft, W. J., *Under the microscope: a brief history of microscopy*. World Scientific: 2006; Vol. 5.

31. Murphy, D. B., *Fundamentals of light microscopy and electronic imaging*. John Wiley & Sons: 2002.

32. Wayne, R. O., *Light and video microscopy*. Academic Press: 2013.

33. Airy, G. B., On the diffraction of an object-glass with circular aperture. *Transactions of the Cambridge Philosophical Society* **1835,** *5*, 283.

34. Sjostrand, F. S., *Electron microscopy of cells and tissues*. Academic Press: New York, 1967.

35. Bernhard, W., Electron microscopy of tumor cells and tumor viruses; a review. *Cancer Res* **1958,** *18* (5), 491-509.

36. Williams, D. B.; Carter, C. B., The transmission electron microscope. In *Transmission electron microscopy*, Springer: 1996; pp 3-17.

37. Weakley, B. S., *Beginner's handbook in biological electron microscopy*. 1972.

38. Pease, D. C., *Histological techniques for electron microscopy*. Elsevier: 2013.

39. Mercer, E. H.; Birbeck, M. S., *Electron microscopy: a handbook for biologists*. 1972.

40. Luft, J. H., Improvements in epoxy resin embedding methods. *J Biophys Biochem Cytol* **1961,** *9* (2), 409-14.

41. Watson, M. L., Staining of tissue sections for electron microscopy with heavy metals. *The Journal of Cell Biology* **1958,** *4* (4), 475-478.

42. Gordon, R. E., Electron Microscopy: A Brief History and Review of Current Clinical Application. In *Histopathology: Methods and Protocols*, Day, C. E., Ed. Springer New York: New York, NY, 2014; pp 119-135.

43. Knapek, E.; Dubochet, J., Beam Damage to Organic Material Is Considerably Reduced in Cryo-Electron Microscopy. *Journal of Molecular Biology* **1980,** *141* (2), 147-161.

44. Cnudde, V.; Masschaele, B.; De Cock, H. E.; Olstad, K.; Vlaminck, L.; Vlassenbroeck, J.; Dierick, M.; Witte, Y. D.; Van Hoorebeke, L.; Jacobs, P., Virtual histology by means of high-resolution X-ray CT. *J Microsc* **2008,** *232* (3), 476-85.

45. Midgley, P. A.; Ward, E. P.; Hungria, A. B.; Thomas, J. M., Nanotomography in the chemical, biological and materials sciences. *Chem Soc Rev* **2007,** *36* (9), 1477-94.

46. Withers, P. J., X-ray nanotomography. *Materials Today* **2007,** *10* (12), 26-34.

47. Metscher, B. D., MicroCT for developmental biology: a versatile tool for high-contrast 3D imaging at histological resolutions. *Dev Dyn* **2009,** *238* (3), 632-40.

48. Diaz, A.; Trtik, P.; Guizar-Sicairos, M.; Menzel, A.; Thibault, P.; Bunk, O., Quantitative x-ray phase nanotomography. *Physical Review B* **2012,** *85* (2), 020104.

49. Metscher, B. D.; Muller, G. B., MicroCT for molecular imaging: quantitative visualization of complete three-dimensional distributions of gene products in embryonic limbs. *Dev Dyn* **2011,** *240* (10), 2301-8.

50. Dyer, E. L.; Roncal, W. G.; Prasad, J. A.; Fernandes, H. L.; Gursoy, D.; De Andrade, V.; Fezzaa, K.; Xiao, X. H.; Vogelstein, J. T.; Jacobsen, C.; Kording, K. P.; Kasthuri, N., Quantifying Mesoscale \Neuroanatomy Using X-Ray Microtomography. *Eneuro* **2017,** *4* (5), ENEURO.0195-17.2017.

51. Albers, J.; Pacilé, S.; Markus, M. A.; Wiart, M.; Velde, G. V.; Tromba, G.; Dullin, C., X-ray-Based 3D Virtual Histology—Adding the Next Dimension to Histological Analysis. *Molecular Imaging Biology* **2018**, 1-10.

52. Taylor, C. R., Immunohistochemistry in surgical pathology: principles and practice. In *Histopathology*, Springer: 2014; pp 81-109.

53. Kohler, G.; Milstein, C., Continuous cultures of fused cells secreting antibody of predefined specificity. *Nature* **1975,** *256* (5517), 495-7.

54. Henle, G.; Henle, W., Immunofluorescence in cells derived from Burkitt's lymphoma. *J Bacteriol* **1966,** *91* (3), 1248-56.

55. Lakowicz, J. R., *Principles of Fluorescence Spectroscopy*. Kluwer Academic/Plenum Publishers, New York: 2004.

56. Widengren, J.; Chmyrov, A.; Eggeling, C.; Lofdahl, P. A.; Seidel, C. A., Strategies to improve photostabilities in ultrasensitive fluorescence spectroscopy. *J Phys Chem A* **2007,** *111* (3), 429-40.

57. Lichtman, J. W.; Conchello, J. A., Fluorescence microscopy. *Nat Methods* **2005,** *2* (12), 910-9.

58. Herschel, J. F. W., No. I. On a case of superficial colour presented by a homogeneous liquid internally colourless. *Philosophical Transactions of the Royal Society of London* **1845**, 143-145.

59. Sabnis, R. W., *Handbook of fluorescent dyes and probes*. John Wiley & Sons: 2015.

60. Giepmans, B. N.; Adams, S. R.; Ellisman, M. H.; Tsien, R. Y., The fluorescent toolbox for assessing protein location and function. *Science* **2006,** *312* (5771), 217-24.

61. Michalet, X.; Pinaud, F. F.; Bentolila, L. A.; Tsay, J. M.; Doose, S.; Li, J. J.; Sundaresan, G.; Wu, A. M.; Gambhir, S. S.; Weiss, S., Quantum dots for live cells, in vivo imaging, and diagnostics. *Science* **2005,** *307* (5709), 538-44.

62. Zimmer, M., Green fluorescent protein (GFP): applications, structure, and related photophysical behavior. *Chem Rev* **2002,** *102* (3), 759-81.

63. Abe, T.; Fujimori, T., Reporter mouse lines for fluorescence imaging. *Dev Growth Differ* **2013,** *55* (4), 390-405.

64. Diaspro, A., *Confocal and Two-Photon Microscopy: Foundations, Applications and Advances*. Wiley: 2001.

65. Pawley, J., *Handbook of biological confocal microscopy*. Springer Science & Business Media: 2010.

66. Schmitt, J. M.; Knuttel, A.; Yadlowsky, M., Confocal microscopy in turbid media. *J Opt Soc Am A Opt Image Sci Vis* **1994,** *11* (8), 2226-35.

67. Theer, P.; Denk, W., On the fundamental imaging-depth limit in two-photon microscopy. *J Opt Soc Am A Opt Image Sci Vis* **2006,** *23* (12), 3139-49.

68. Zipfel, W. R.; Williams, R. M.; Christie, R.; Nikitin, A. Y.; Hyman, B. T.; Webb, W. W., Live tissue intrinsic emission microscopy using multiphoton-excited native fluorescence and second harmonic generation. *Proceedings of the National Academy of Sciences of the United States of America* **2003,** *100* (12), 7075-80.

69. Helmchen, F.; Denk, W., Deep tissue two-photon microscopy. *Nat Methods* **2005,** *2* (12), 932-40.

70. Wang, T.; Ouzounov, D. G.; Wu, C.; Horton, N. G.; Zhang, B.; Wu, C. H.; Zhang, Y.; Schnitzer, M. J.; Xu, C., Three-photon imaging of mouse brain structure and function through the intact skull. *Nat Methods* **2018,** *15* (10), 789-792.

71. Göppert-Mayer, M., Über elementarakte mit zwei quantensprüngen. *J Annalen der Physik* **1931,** *401* (3), 273-294.

72. Maiman, T. H., Stimulated Optical Radiation in Ruby. *Nature* **1960,** *187* (4736), 493-494.

73. Franken, P. A.; Weinreich, G.; Peters, C. W.; Hill, A. E., Generation of Optical Harmonics. *Phys Rev Lett* **1961,** *7* (4), 118-&.

74. Ding, L.; Blackwell, R.; Kunzler, J. F.; Knox, W. H., Large refractive index change in silicone-based and non-silicone-based hydrogel polymers induced by femtosecond laser micro-machining. *Opt Express* **2006,** *14* (24), 11901-9.

75. Aptel, F.; Olivier, N.; Deniset-Besseau, A.; Legeais, J. M.; Plamann, K.; Schanne-Klein, M. C.; Beaurepaire, E., Multimodal nonlinear imaging of the human cornea. *Investigative ophthalmology & visual science* **2010,** *51* (5), 2459-65.

76. Boyd, R. W., *Nonlinear optics*. Elsevier: 2003.

77. Squier, J.; Muller, M.; Brakenhoff, G.; Wilson, K. R., Third harmonic generation microscopy. *Opt Express* **1998,** *3* (9), 315-24.

78. Bass, M.; Hill, A. E.; Franken, P. A.; Peters, C. W.; Weinreich, G., Optical Mixing. *Phys Rev Lett* **1962,** *8* (1), 18-&.

79. Wang, C. C.; Racette, G. W., Measurement of Parametric Gain Accompanying Optical Difference Frequency Generation. *Appl Phys Lett* **1965,** *6* (8), 169-&.

80. Di Lullo, G. A.; Sweeney, S. M.; Körkkö, J.; Ala-Kokko, L.; San Antonio, J. D., Mapping the ligand-binding sites and disease-associated mutations on the most abundant protein in the human, type I collagen. *Journal of Biological Chemistry* **2002,** *277* (6), 4223-4231.

81. Campagnola, P., Second harmonic generation imaging microscopy: applications to diseases diagnostics. *Anal Chem* **2011,** *83* (9), 3224-31.

82. Moreaux, L.; Sandre, O.; Mertz, J., Membrane imaging by second-harmonic generation microscopy. *Journal of the Optical Society of America B* **2000,** *17* (10), 1685.

83. Moreaux, L.; Sandre, O.; Blanchard-Desce, M.; Mertz, J., Membrane imaging by simultaneous second-harmonic generation and two-photon microscopy. *Optics Letters* **2000,** *25* (5), 320.

84. Beaurepaire, E.; Débarre, D.; Olivier, N., THG Microscopy of Cells and Tissues: Contrast Mechanisms and Applications. In *Second Harmonic Generation Imaging*, CRC Press: 2016; pp 70-99.

85. New, G., *Introduction to nonlinear optics*. Cambridge University Press: 2011.

86. Weigelin, B.; Bakker, G. J.; Friedl, P., Third harmonic generation microscopy of cells and tissue organization. *J Cell Sci* **2016,** *129* (2), 245-55.

87. Debarre, D.; Supatto, W.; Pena, A. M.; Fabre, A.; Tordjmann, T.; Combettes, L.; Schanne-Klein, M. C.; Beaurepaire, E., Imaging lipid bodies in cells and tissues using third-harmonic generation microscopy. *Nat Methods* **2006,** *3* (1), 47-53.

88. Farrar, M. J.; Wise, F. W.; Fetcho, J. R.; Schaffer, C. B., In vivo imaging of myelin in the vertebrate central nervous system using third harmonic generation microscopy. *Biophysical journal* **2011,** *100* (5), 1362-71.

89. Olivier, N.; Luengo-Oroz, M. A.; Duloquin, L.; Faure, E.; Savy, T.; Veilleux, I.; Solinas, X.; Debarre, D.; Bourgine, P.; Santos, A.; Peyrieras, N.; Beaurepaire, E., Cell lineage reconstruction of early zebrafish embryos using label-free nonlinear microscopy. *Science* **2010,** *329* (5994), 967-71.

90. Oron, D.; Yelin, D.; Tal, E.; Raz, S.; Fachima, R.; Silberberg, Y., Depth-resolved structural imaging by third-harmonic generation microscopy. *J Struct Biol* **2004,** *147* (1), 3-11.

91. Tripathy, U.; Giguere-Bisson, M.; Sangji, M. H.; Bellemare, M. J.; Bohle, D. S.; Georges, E.; Wiseman, P. W., Optimization of malaria detection based on third harmonic generation imaging of hemozoin. *Analytical and bioanalytical chemistry* **2013,** *405* (16), 5431-40.

92. Belisle, J. M.; Costantino, S.; Leimanis, M. L.; Bellemare, M. J.; Bohle, D. S.; Georges, E.; Wiseman, P. W., Sensitive detection of malaria infection by third harmonic generation imaging. *Biophysical journal* **2008,** *94* (4), L26-8.

93. Clay, G. O.; Millard, A. C.; Schaffer, C. B.; Aus-Der-Au, J.; Tsai, P. S.; Squier, J. A.; Kleinfeld, D., Spectroscopy of third-harmonic generation: evidence for resonances in model compounds and ligated hemoglobin. *J Opt Soc Am B* **2006,** *23* (5), 932-950.

94. Tuer, A.; Tokarz, D.; Prent, N.; Cisek, R.; Alami, J.; Dumont, D. J.; Bakueva, L.; Rowlands, J.; Barzda, V., Nonlinear multicontrast microscopy of hematoxylin-and-eosin-stained histological sections. *J Biomed Opt* **2010,** *15* (2), 026018.

95. Williams, R. M.; Zipfel, W. R.; Webb, W. W., Multiphoton microscopy in biological research. *Current opinion in chemical biology* **2001,** *5* (5), 603-8.

96. Deyl, Z.; Macek, K.; Adam, M.; Vancikova, O., Studies on the chemical nature of elastin fluorescence. *Biochim Biophys Acta* **1980,** *625* (2), 248-54.

97. Campagnola, P. J.; Millard, A. C.; Terasaki, M.; Hoppe, P. E.; Malone, C. J.; Mohler, W. A., Three-dimensional high-resolution second-harmonic generation imaging of endogenous structural proteins in biological tissues. *Biophysical journal* **2002,** *82* (1 Pt 1), 493-508.

98. Huang, S.; Heikal, A. A.; Webb, W. W., Two-photon fluorescence spectroscopy and microscopy of NAD(P)H and flavoprotein. *Biophysical journal* **2002,** *82* (5), 2811-25.

99. Chen, B.; Huang, X.; Gou, D.; Zeng, J.; Chen, G.; Pang, M.; Hu, Y.; Zhao, Z.; Zhang, Y.; Zhou, Z.; Wu, H.; Cheng, H.; Zhang, Z.; Xu, C.; Li, Y.; Chen, L.; Wang, A., Rapid

volumetric imaging with Bessel-Beam three-photon microscopy. *Biomed Opt Express* **2018,** *9* (4), 1992-2000.

100. Guesmi, K.; Abdeladim, L.; Tozer, S.; Mahou, P.; Kumamoto, T.; Jurkus, K.; Rigaud, P.; Loulier, K.; Dray, N.; Georges, P.; Hanna, M.; Livet, J.; Supatto, W.; Beaurepaire, E.; Druon, F., Dual-color deep-tissue three-photon microscopy with a multiband infrared laser. *Light-Science & Applications* **2018,** *7* (1), 12.

101. Lee, S.; Lee, J. H.; Wang, T.; Jang, W. H.; Yoon, Y.; Kim, B.; Jun, Y. W.; Kim, M. J.; Kim, K. H., Three-photon tissue imaging using moxifloxacin. *Sci Rep* **2018,** *8* (1), 9415.

102. Ouzounov, D. G.; Wang, T.; Wang, M.; Feng, D. D.; Horton, N. G.; Cruz-Hernandez, J. C.; Cheng, Y. T.; Reimer, J.; Tolias, A. S.; Nishimura, N.; Xu, C., In vivo three-photon imaging of activity of GCaMP6-labeled neurons deep in intact mouse brain. *Nat Methods* **2017,** *14* (4), 388-390.

103. Horton, N. G.; Wang, K.; Kobat, D.; Clark, C. G.; Wise, F. W.; Schaffer, C. B.; Xu, C., In vivo three-photon microscopy of subcortical structures within an intact mouse brain. *Nat Photonics* **2013,** *7* (3), 205-209.

104. Squier, J.; Muller, M., High resolution nonlinear microscopy: A review of sources and methods for achieving optimal imaging. *Rev Sci Instrum* **2001,** *72* (7), 2855-2867.

105. Haus, H. A., Mode-locking of lasers. *IEEE Journal of Selected Topics in Quantum Electronics* **2000,** *6* (6), 1173-1185.

106. Spence, D. E.; Kean, P. N.; Sibbett, W., 60-fsec pulse generation from a self-mode-locked Ti:sapphire laser. *Opt Lett* **1991,** *16* (1), 42-4.

107. Hecht, J. In *Short history of laser development*, SPIE: 2010; p 23.

108. Yelin, D.; Oron, D.; Korkotian, E.; Segal, M.; Silberberg, Y., Third-harmonic microscopy with a titanium–sapphire laser. *Applied Physics B* **2014,** *74* (S1), s97-s101.

109. Giordmaine, J.; Miller, R. C., Tunable coherent parametric oscillation in LiNbO3 at optical frequencies. *Phys Rev Lett* **1965,** *14* (24), 973.

110. Herz, J.; Siffrin, V.; Hauser, A. E.; Brandt, A. U.; Leuenberger, T.; Radbruch, H.; Zipp, F.; Niesner, R. A., Expanding two-photon intravital microscopy to the infrared by means of optical parametric oscillator. *Biophysical journal* **2010,** *98* (4), 715-23.

111. Edelstein, D. C.; Wachman, E. S.; Tang, C. L., Broadly Tunable High Repetition Rate Femtosecond Optical Parametric Oscillator. *Appl Phys Lett* **1989,** *54* (18), 1728-1730.

112. Dunn, M. H.; Ebrahimzadeh, M., Parametric Generation of Tunable Light from Continuous-Wave to Femtosecond Pulses. *Science* **1999,** *286* (5444), 1513-1518.

113. Lefort, C., A review of biomedical multiphoton microscopy and its laser sources. *J Phys D Appl Phys* **2017,** *50* (42), 423001.

114. Arrigoni, M., Lasers for Optogenetics and Multimodal Microscopy. *Optik & Photonik* **2016,** *11* (2), 27-30.

115. Taylor, J. R., Tutorial on fiber-based sources for biophotonic applications. *J Biomed Opt* **2016,** *21* (6), 61010.

116. Tu, H.; Liu, Y.; Turchinovich, D.; Marjanovic, M.; Lyngso, J.; Laegsgaard, J.; Chaney, E. J.; Zhao, Y.; You, S.; Wilson, W. L.; Xu, B.; Dantus, M.; Boppart, S. A., Stain-free histopathology by programmable supercontinuum pulses. *Nat Photonics* **2016,** *10* (8), 534-540.

117. Denk, W.; Strickler, J. H.; Webb, W. W., Two-photon laser scanning fluorescence microscopy. *Science* **1990,** *248* (4951), 73-6.

118. Hanninen, A. M.; Prince, R. C.; Ramos, R.; Plikus, M. V.; Potma, E. O., High-resolution infrared imaging of biological samples with third-order sum-frequency generation microscopy. *Biomed Opt Express* **2018,** *9* (10), 4807-4817.

119. Zumbusch, A.; Holtom, G. R.; Xie, X. S., Three-dimensional vibrational imaging by coherent anti-Stokes Raman scattering. *Phys Rev Lett* **1999,** *82* (20), 4142-4145.

120. Freudiger, C. W.; Min, W.; Saar, B. G.; Lu, S.; Holtom, G. R.; He, C.; Tsai, J. C.; Kang, J. X.; Xie, X. S., Label-free biomedical imaging with high sensitivity by stimulated Raman scattering microscopy. *Science* **2008,** *322* (5909), 1857-61.

121. Konig, K.; Schenke-Layland, K.; Riemann, I.; Stock, U. A., Multiphoton autofluorescence imaging of intratissue elastic fibers. *Biomaterials* **2005,** *26* (5), 495-500.

122. Durr, N. J.; Larson, T.; Smith, D. K.; Korgel, B. A.; Sokolov, K.; Ben-Yakar, A., Two-photon luminescence imaging of cancer cells using molecularly targeted gold nanorods. *Nano Lett* **2007,** *7* (4), 941-5.

123. Vigil, G. D.; Howard, S. S., Photophysical characterization of sickle cell disease hemoglobin by multi-photon microscopy. *Biomed Opt Express* **2015,** *6* (10), 4098-104.

124. Richardson, L.; Vargas, G.; Brown, T.; Ochoa, L.; Trivedi, J.; Kacerovsky, M.; Lappas, M.; Menon, R., Redefining 3Dimensional placental membrane microarchitecture using multiphoton microscopy and optical clearing. *Placenta* **2017,** *53*, 66-75.

125. Brown, E.; McKee, T.; diTomaso, E.; Pluen, A.; Seed, B.; Boucher, Y.; Jain, R. K., Dynamic imaging of collagen and its modulation in tumors in vivo using second-harmonic generation. *Nat Med* **2003,** *9* (6), 796-800.

126. Dombeck, D. A.; Kasischke, K. A.; Vishwasrao, H. D.; Ingelsson, M.; Hyman, B. T.; Webb, W. W., Uniform polarity microtubule assemblies imaged in native brain tissue by second-harmonic generation microscopy. *Proceedings of the National Academy of Sciences of the United States of America* **2003,** *100* (12), 7081-6.

127. Boulesteix, T.; Beaurepaire, E.; Sauviat, M. P.; Schanne-Klein, M. C., Second-harmonic microscopy of unstained living cardiac myocytes: measurements of sarcomere length with 20-nm accuracy. *Opt Lett* **2004,** *29* (17), 2031-3.

128. Kottmann, R. M.; Sharp, J.; Owens, K.; Salzman, P.; Xiao, G. Q.; Phipps, R. P.; Sime, P. J.; Brown, E. B.; Perry, S. W., Second harmonic generation microscopy reveals altered collagen microstructure in usual interstitial pneumonia versus healthy lung. *Respir Res* **2015,** *16*, 61.

129. Yildirim, M.; Quinn, K. P.; Kobler, J. B.; Zeitels, S. M.; Georgakoudi, I.; Ben-Yakar, A., Quantitative differentiation of normal and scarred tissues using second-harmonic generation microscopy. *Scanning* **2016,** *38* (6), 684-693.

130. Goulam Houssen, Y.; Gusachenko, I.; Schanne-Klein, M. C.; Allain, J. M., Monitoring micrometer-scale collagen organization in rat-tail tendon upon mechanical strain using second harmonic microscopy. *J Biomech* **2011,** *44* (11), 2047-52.

131. Yu, C. H.; Tai, S. P.; Kung, C. T.; Wang, I. J.; Yu, H. C.; Huang, H. J.; Lee, W. J.; Chan, Y. F.; Sun, C. K., In vivo and ex vivo imaging of intra-tissue elastic fibers using third-harmonic-generation microscopy. *Opt. Express* **2007,** *15* (18), 11167-11177.

132. Kuzmin, N. V.; Wesseling, P.; Hamer, P. C.; Noske, D. P.; Galgano, G. D.; Mansvelder, H. D.; Baayen, J. C.; Groot, M. L., Third harmonic generation imaging for fast, label-free pathology of human brain tumors. *Biomed Opt Express* **2016,** *7* (5), 1889-904.

133. Saytashev, I.; Glenn, R.; Murashova, G. A.; Osseiran, S.; Spence, D.; Evans, C. L.; Dantus, M., Multiphoton excited hemoglobin fluorescence and third harmonic generation for non-invasive microscopy of stored blood. *Biomed Opt Express* **2016,** *7* (9), 3449-3460.

134. Le, T. T.; Langohr, I. M.; Locker, M. J.; Sturek, M.; Cheng, J. X., Label-free molecular imaging of atherosclerotic lesions using multimodal nonlinear optical microscopy. *J Biomed Opt* **2007,** *12* (5), 054007.

135. Lee, J. H.; Kim, D. H.; Song, W. K.; Oh, M. K.; Ko, D. K., Label-free imaging and quantitative chemical analysis of Alzheimer's disease brain samples with multimodal multiphoton nonlinear optical microspectroscopy. *J Biomed Opt* **2015,** *20* (5), 56013.

136. Paugh, J. R.; Alfonso-Garcia, A.; Nguyen, A. L.; Suhalim, J. L.; Farid, M.; Garg, S.; Tao, J.; Brown, D. J.; Potma, E. O.; Jester, J. V., Characterization of expressed human meibum using hyperspectral stimulated Raman scattering microscopy. *Ocul Surf* **2019,** *17* (1), 151-159.

137. Cicerone, M. T.; Camp, C. H., Histological coherent Raman imaging: a prognostic review. *Analyst* **2017,** *143* (1), 33-59.

138. You, S.; Sun, Y.; Chaney, E. J.; Zhao, Y.; Chen, J.; Boppart, S. A.; Tu, H., Slide-free virtual histochemistry (Part I): development via nonlinear optics. *Biomed Opt Express* **2018,** *9* (11), 5240-5252.

139. You, S.; Sun, Y.; Chaney, E. J.; Zhao, Y.; Chen, J.; Boppart, S. A.; Tu, H., Slide-free virtual histochemistry (Part II): detection of field cancerization. *Biomed Opt Express* **2018,** *9* (11), 5253-5268.

Preface to Chapter 2

In this chapter, we present a novel malaria detection technique, third harmonic generation image scanning cytometry (THGISC). THGISC combines nonlinear microscopy (namely third harmonic generation imaging) with automated software-based image processing and rapid motorized scanning to provide a high throughput, single channel, quantitative diagnosis method that counts the number of red blood cells in thin blood smears and determines parasitemia. The method was validated using cultured malaria parasites at different lifecycle stages (ring, trophozoite and schizont) with two photon fluorescence of nuclear staining. THGISC was applied to whole blood patient samples obtained in collaboration with Dr. Wellington Oyibo, University of Lagos, Nigeria.

This chapter was published as an article in *Analytical Chemistry* (Kazarine et al. 2019). Supplementary information for this article can be found in Appendix A.

2 Malaria Detection by Third-Harmonic Generation Image Scanning Cytometry

Alexei Kazarine,† Fadi Baakdah,‡ Angelica A. Gopal,† Wellington Oyibo,§ Elias Georges,‡ and Paul W. Wiseman*,†,‖

†Department of Chemistry, McGill University, 801 Sherbrooke Street West, Montreal, Quebec H3A 0B8, Canada

‡Institute of Parasitology, McGill University, Sainte Anne de Bellevue, Quebec H9X 3 V9, Canada

§ANDI Centre of Excellence for Malaria Diagnosis, College of Medicine, University of Lagos, Idi-Araba, Lagos 100254, Nigeria

‖Department of Physics, McGill University, 3600 University Street, Montreal, Quebec H3A 2T8, Canada

2.1 Abstract

Despite global efforts aimed at its elimination, malaria is still a significant health concern in many countries across the world. The disease is caused by blood-borne parasites, *Plasmodium* species, and is transmitted by female *Anopheles* mosquitoes and presents with generic febrile symptoms that are challenging to diagnose clinically. To adequately tackle this issue, an effective detection method is required for screening potential malaria patients for infection. To this day, the gold standard for malaria detection remains basic light microscopy of Giemsa-stained patient blood smears to first enable detection and manual counting to determine the parasite density by a microscopist. While effective at detecting parasites, this method requires both significant time and skilled personnel. As an alternate approach, we propose a new malaria detection method that we call third-harmonic generation image scanning cytometry (THGISC) based on the combination of third-harmonic generation imaging, high-speed motorized scanning, and automated software processing. Third-harmonic generation (THG) is a nonlinear optical process in which the frequency of incident photons is tripled within the sample material. We have previously demonstrated that hemozoin, a metabolic by product of the malaria parasite, presents a significant

THG signal. We now present a practical approach that uses the selectivity of this contrast mechanism to perform label-free image scanning cytometry of patient blood smears for automated malaria detection. In this work, we applied this technique to lab-cultured parasites and parasites in whole blood obtained from malaria patients. We also compared its effectiveness to parasite counts obtained by classical methods. The ability to easily and rapidly determine parasitemia by THG offers potential not only for the easy confirmation of malaria diagnoses following symptoms, but also the tracking of treatment progress in existing patients, potentially allowing physicians to adjust medication and dosage for each individual.

2.2 Introduction

To this day, malaria remains a significant global public health issue. This infectious disease is caused by *Plasmodium* species, blood-borne apicomplexan parasites transmitted by mosquitoes, with most cases and deaths caused by *Plasmodium falciparum*.[1] In 2017, the World Health Organization (WHO) reported over 216 million cases of infection, with over 90% occurring in Africa.[2] It is estimated that malaria causes over a hundred thousand deaths each year. The infection begins from sporozoites injected into the bloodstream during the mosquito's blood meal.[3] This infective motile stage of the parasite travels to the liver where it begins reproducing asexually, releasing merozoites into the blood-stream. These merozoites proceed to infect erythrocytes to replicate, consuming the hemoglobin contained within, and enter the ring stage. The rings then mature to become trophozoites. After rapid growth within the red blood cell (RBC), they undergo multiple asexual fission (schizogony) developing into a schizont that eventually results in hemolysis and release of merozoites to continue the parasitic lifecycle. During hemolysis, the patient presents with general febrile symptoms, making clinical diagnosis difficult.[4,5] While the disease is curable, early and accurate confirmation of malaria parasites in suspected patients is

critical for effective case management of malaria to prevent the onset of severe malaria that may be fatal.

The current gold standard for malaria detection is lightmicroscopy[6] that requires the preparation of Giemsa-stained blood smears that are then examined by a trained technician who would have to skillfully view the fields of the smear to detect or negate the presence of the parasite. Thick blood smears allow for more sensitive parasite detection, while thin blood smears permit more precise determination of the *Plasmodium* species. However, this method presents several drawbacks, including the need for trained and experienced personnel, low detection sensitivity for cases of low parasitemia, and the subjective nature of manual observation. A variety of alternative malaria diagnostic techniques have now been developed including fluorescence microscopy,[7] point-of-care rapid diagnostic tests[8] (RDT) based on antigen detection, nucleic acid based analyses,[9] microfluidic devices,[10] and othersensors.[11] While these methods show significant promise, the WHO still recommends the use of light microscopy as the diagnostic tool for potential malaria cases[2] in addition to malaria RDTs.

Other detection methods have been elaborated based on the detection of hemozoin,[12] a biocrystalline byproduct of the *Plasmodium* parasite's digestion of hemoglobin, instead of direct parasite detection. This metabolic by product is characteristic of malaria infection and is presently being researched as a biomarker for malaria detection[13] as well as a potential target for antimalarial drugs. Hemozoin's nature as a biological crystal endows it interesting optical properties that can be exploited for its detection. Several potential malaria diagnostic methods have now been demonstrated, including the use of cell-phone-based polarized light microscopy to exploit its birefringence[14] and an acoustic method based on the production of nanobubbles generated by its

interaction with ultrafast laser pulses.[15,16] Another technique based on simple in vivo UV−vis absorption spectroscopy of hemozoin has also been reported.[17]

Another remarkable optical property of hemozoin is its significant third-order nonlinear optical susceptibility resulting in efficient third-harmonic generation (THG). THG is a nonlinear coherent optical process in which three photons of incident light combine to form one photon at one-third of the excitation wavelength. This process mainly occurs at interfaces between materials presenting different refractive indexes or third-order nonlinear susceptibilities.[18] THG imaging provides a simple yet powerful contrast method that does not require any form of external labeling. We have previously demonstrated that hemozoin presents a highly specific THG signal when illuminated with near-infrared ultrafast pulses.[19] The method was demonstrated on both cultured *Plasmodium* parasites and synthetic hematin anhydride crystals, but its practical effectiveness has not yet been established.[20]

In the development of an effective and practical implementation of THG-based malaria detection, a high-throughput approach is desired to maximize detection chances and minimize time-to-answer. One such approach could be its implementation into flow cytometry. However, as THG is an interface effect that requires scanning with a diffraction-limited laser beam, it is not directly compatible with flow cytometry instrumentation which typically utilizes a widefield configuration. A more practical approach to THG-based malaria detection is its implementation in the form of image scanning cytometry. Unlike flow cytometry, image scanning cytometry relies on automated rapid scanning of microscopy slide areas to perform single-cell optical measurements on a high-throughputlevel.[21,22] One additional advantage of imaged-based cytometry over standard flow cytometry is the ability to obtain detailed data for each imaged cell, including morphological data

such as cell size.[23] Overall, while image scanning cytometry does present a lower throughput than flow cytometry, it is presently the favored option when it comes to THG cytometry due to the unique interface-based nature of this contrast mechanism.

In this work, we combined THG imaging with motorized scanning and easy-to-use processing software to establish a new method for malaria detection that we call third-harmonic generation image scanning cytometry (THGISC) (Figure 2-1).

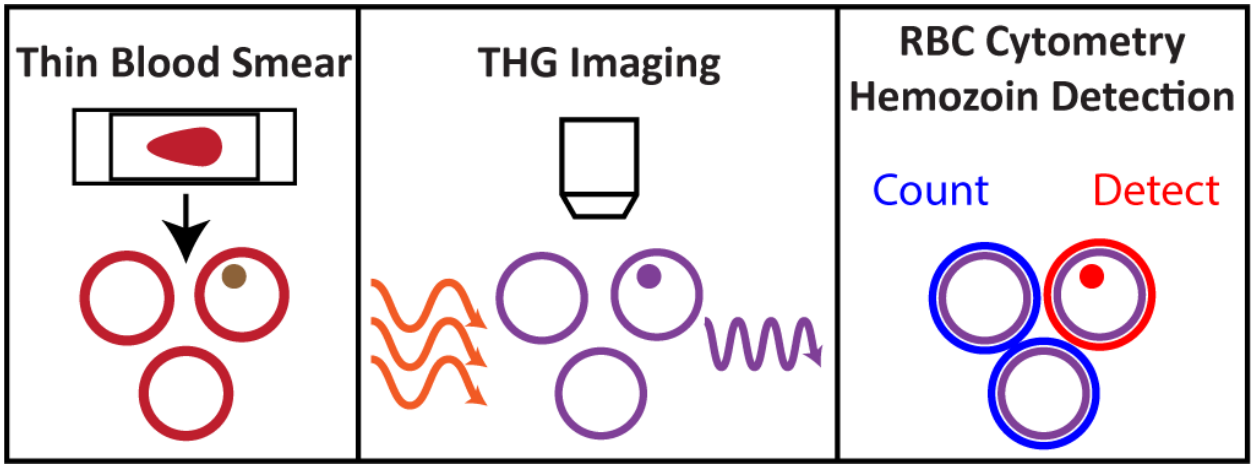

Figure 2-1: Methodology schematic of malaria detection by THG image scanning cytometry.

Using a single detection channel, we can locate both red blood cells and *Plasmodium* parasites via their hemoglobin and hemozoin crystals, respectively. This method enables screening at the single red blood cell level to rapidly and effectively determine parasitemia in whole patient blood, label-free. Thanks to the specificity of the THG signal and the use of automated image analysis, malaria detection using THGISC does not require prior user experience or skill. We have tested the method on both cultured *P. falciparum parasites* at several erythrocytic lifecycle stages and whole-blood samples obtained from confirmed malaria patients. Method performance was compared using two-photon fluorescence (TPF) microscopy of fluorescent nuclear stains using the same

imaging system for the cultured parasites. Classical light microscopy was used to independently verify parasitemia for the patient study.

2.3 Methods

2.3.1 *P. falciparum* Asexual Blood Stages Cultivation.

P. falciparum 3D7-H strain was maintained in a continuous synchronous culture as described previously by Trager and Jensen[24] with a few modifications. Culture reagents were obtained from ThermoFisher Scientific, Massachusetts, unless stated otherwise. Briefly, parasites were cultivated in RPMI 1640 media supplemented with L-glutamine and HEPES in 10% human plasma and A+ human erythrocytes (The Interstate Blood Bank Inc., Tennessee) in a maintained packed cell volume of 2%. They were synchronized with 5% sorbitol (MilliporeSigma, Ontario, Canada), and each stage was collected at 8% from rings, trophozoites, and schizonts. Once the parasites reached 8% they were washed with PBS and fixed in 4% paraformaldehyde (electron microscopy grade, Electron Microscopy Sciences, Pennsylvania) in PBS.

2.3.2 Patient Blood Collection from Clinical Cases and Parasitemia Determination.

Blood samples were collected from patients that presented with malaria-related symptoms who consented to participating in an ongoing malaria research in Ikorodu, Lagos, Nigeria. The study protocol was approved by the Ethics Committee of the College of Medicine, University of Lagos, Lagos, Nigeria. In summary, 3 mL of venous blood was collected from patients and stored in a 5 mL EDTA blood bottle that was gently rotated to ensure the collected blood mixed with the anticoagulant. Two thin and thick malaria blood films (MBFs) were prepared on the same slide and stained with Giemsa using standard protocol.

The stained MBFs were read independently by two WHO grade I certified microscopists who confirmed the presence or absence of *Plasmodium* species (detection), speciated into different species of *Plasmodium* species, reported the stage of the parasites, and enumerated the parasites in thick film using standard procedures. Where there was discordance in parasite detection and counts, a third microscopist that served as an arbiter reread the MBF to resolve the discordant result. The *Plasmodium* parasites seen were counted against a minimum of 500 leucocytes, while 200 oil immersion fields were scanned to declare an MBF negative. Parasite density was computed using an estimated 8000 white blood cells and reported as parasites per microliter of blood from parasites in thick film preparation.

2.3.3 Sample Preparation from Cultured Plasmodium Parasites.

Thin blood smears were prepared from parasites cultured and synchronized at three different lifecycle stages: ring, trophozoite, and schizont. Samples were separately stained with two fluorescent nuclear stains: acridine orange (MilliporeSigma, Ontario, Canada) or DAPI (4',6-diamidino-2-phenylindole, ThermoFisher Scientific, Massachusetts, U.S.A.) for verification. Blood smears were also prepared from whole-blood samples obtained from malaria patients after dilution in phosphate-buffered saline (DPBS, ThermoFisher Scientific, Massachusetts, U.S.A.) by 50% to ensure thin films. Samples were rehydrated and mounted on coverslips immediately prior to imaging.

2.3.4 Experimental Setup.

THGISC was conducted using a customized multiphoton imaging system (Figure 2-2). The system consists of two tunable ultrafast laser sources coupled to an upright microscope base and scanning unit (FV1200 MPE, Olympus Canada Inc., Ontario, Canada): a Ti:sapphire laser (Mira

900F, Coherent, California, U.S.A.) and an optical parametric oscillator (Mira OPO, Coherent, California, U.S.A.). Switching between sources is automated through two motorized flip mounts (MFF101, Thorlabs, New Jersey, U.S.A.), while laser power is controlled using a custom motorized variable attenuator system operated by a custom Labview Program (National Instruments, Texas, U.S.A.). Laser power is measured directly before beam entrance to the microscope using a thermal power sensor (S175C/PM100D, Thorlabs, New Jersey, U.S.A.). The excitation light was directed at blood smear samples mounted on a high-speed motorized stage (H117, Prior Scientific, Massachusetts, U.S.A.) using a 25× 1.05 NA water immersion multiphoton objective (XLPL25XWMP, Olympus Canada Inc., Ontario, Canada). A 0.9 NA dry top lens condenser directed the output light to two forward detection photomultipliers (PMTs), enabling simultaneous trans detection of THG light along with two-photon dye fluorescence. Blood smears were first imaged with OPO excitation (1150 nm, 150 mW) to collect THG emission (380−420 nm filter, ET400/40X, Chroma Technology, Vermont, U.S.A.). Two-photon fluorescence was then excited with the Ti:sapphire laser (780 nm, 80 mW) to enable detection of DAPI (460−500 nm filter, BA460-500, Olympus Canada Inc., Ontario, Canada) and acridine orange (515−555 nm filter, BA515-555, Olympus Canada Inc., Ontario, Canada). THG was separated from fluorescence using a dichroic mirror (T425LPXR, Chroma Technology, Vermont, U.S.A.). An edge-pass infrared blocking filter (FF01-770/SP32, Semrock, New York, U.S.A.) was placed immediately after the condenser to ensure complete blocking of excitation light at the detection PMTs. Samples were imaged using a 248 nm X−Y pixel size, 2 µs pixel dwell time, resulting in a 1 s frame time for a 1024 × 1024 pixels image.

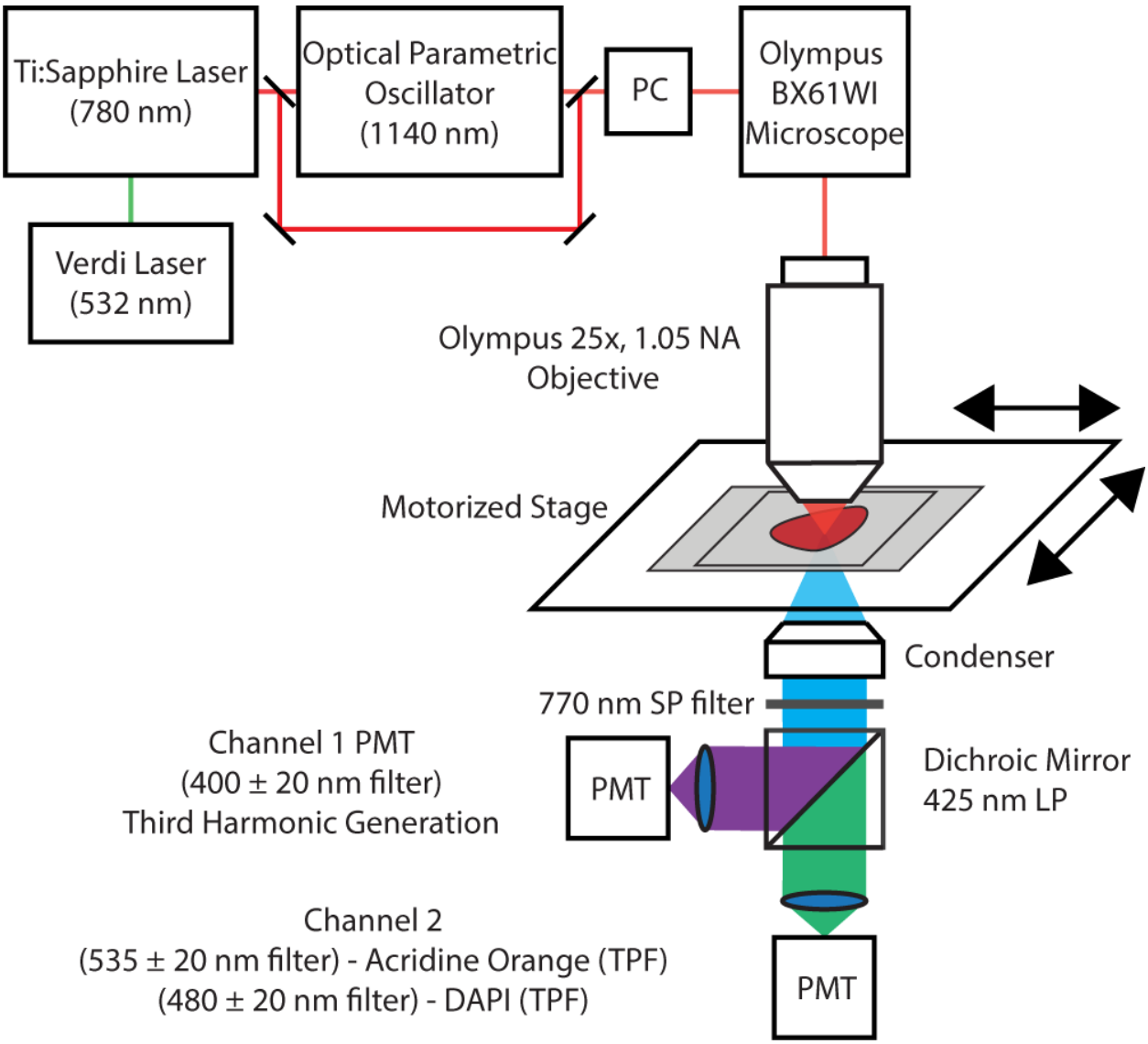

Figure 2-2: Experimental THGISC imaging setup. Abbreviations: PC, power control; PMT, photomultiplier tube; TPF, two-photon fluorescence; SP, short-pass filter; LP, long-pass filter.

2.3.5 Image Analysis

THG and dye fluorescence images were first registered using the pairwise FIJI stitching plug-in[25] to ensure overlap of features. For the cultured parasite experiments, a graphical user interface (GUI) MATLAB application was used to establish overlap of detected parasites between the THG and dye channels. First, an intensity threshold was used for each channel to create a binary image representing the hemozoin and parasite nuclei locations. Morphological dilation with a disk

structural element was then used in each channel to ensure that overlapping signals from the same parasite were counted as one using the MATLAB functions "strel" and "imdilate". The parasites in each channel were then counted with the "bwconncomp" function and compared. The GUI application is available upon request.

Malaria detection in patient blood was conducted using a custom GUI MATLAB application (Figure A-1). First, a smoothing Gaussian filter ("imgaussfilt" function) was applied to the THG image to prepare for segmentation. A circular Hough transform ("imfindcircles" function) was then used to detect each individual red blood cell and establish a total cell count per image. Within the same channel, a threshold intensity was selected to locate potential parasites from their nearly saturated hemozoin signal. The centroids of these locations were found using the "regionprops" function, which were then referenced to the detected RBCs to verify that the hemozoin was located within an RBC. These cells were then declared as infected, and a total parasitemia % was calculated for each image and averaged for each patient sample. The GUI application is available upon request.

2.4 Results and Discussion

Third-harmonic generation imaging enables a powerful malaria detection approach by providing a sensitive contrast mechanism that highlights both parasite-produced hemozoin and erythrocytes within the same detection channel. Hemoglobin, the oxygen transport protein that is ubiquitous within red blood cells, presents a resonance-enhanced THG signal when the THG wavelength is tuned close to its Soret spectroscopic absorption band.[26,27] This property has previously been exploited to examine and evaluate morphology of stored RBCs within blood bags.[28] Hemozoin, also known as β-hematin, is a biocrystal formed during the Plasmodium parasite's digestion of

hemoglobin.[29] The digestion process releases free hematin, which is toxic to the parasite, resulting in the production of hemozoin as a detoxification mechanism. Owing to a similar resonance mechanism as hemoglobin, hemozoin has been found to be a very strong source of THG, generating signals over an order of magnitude higher than those of hemoglobin. By using THG exclusively as a contrast mechanism, it is possible to simultaneously detect RBCs via hemoglobin and malaria parasites via hemozoin with the segmentation between the two easily implemented due to the large signal difference.

As THG is a nonlinear optical effect that requires a tight diffraction-limited beam focus to achieve the necessary excitation power, its usage is incompatible with standard flow cytometry instrumentation which uses a wide focus to illuminate whole cells at lower power. However, by combining THG laser scanning microscopy with rapid motorized scanning, a high-throughput measurement can still be achieved without relying on flow processes. This approach brings the benefit of image-based cytometry which provides single-cell characterization, enabling us to monitor hemozoin on a subcellular level in addition to visualizing morphological cellular features. Once images of the sampled erythrocytes are obtained, simple image processing can be used to identify and count red blood cells and highlight potential infected ones via the significant hemozoin signal.

2.4.1 Validation Using Cultured Parasites.

To establish our method as a practical means for malaria detection, it was imperative to characterize its performance using known controls. We first applied our technique to P. falciparum parasites cultured in packed red blood cells at three different lifecycle stages: ring (early trophozoite), trophozoite, and schizont stages. To validate our measurements, two-photon

fluorescence (TPF) imaging was performed alongside THG imaging using two nuclear staining fluorescent dyes commonly used for malaria parasite detection, acridine orange (AO)[30] and DAPI (4',6-diamidino-2-phenylindole).[31] By performing two-photon fluorescence microscopy with the same imaging system as for THG, it was possible to obtain a direct comparison for parasite numbers obtained for the same fields of view with both methods. Since healthy RBCs do not possess DNA, any fluorescence signal present within an RBC after staining could be attributed to the presence of parasite DNA. Both AO and DAPI are intercalating DNA dyes and yield increased fluorescence upon binding to DNA. To obtain efficient two-photon excitation of the fluorescent dyes, a Ti:sapphire laser source was used instead of the OPO, owing to its ability to generate excitation light at a lower wavelength (780 nm), closer to the peak of their two-photon absorbance. Example images obtained from this study can be found in Figure 2-3 for the three different parasite stages examined, showing nearly exact overlap (white) between the parasite nuclei (green for AO and cyan for DAPI) and hemozoin (magenta) locations. It is important to note that the hemozoin is located within the malaria parasite's digestive vacuole, whereas the AO/DAPI signals originate from the parasite's nucleus. As such, these two signals are not completely colocalized depending on the parasites' spatial orientation. The PMT sensitivity for the THG channel was adjusted to clearly visualize the RBCs in addition to the hemozoin, resulting in a saturated signal associated with the presence of hemozoin due to its high intrinsic third-order nonlinear susceptibility. Using simple image processing, we determined the number of parasites per image obtained by THG and TPF for parasites stained with AO (Figure 2-4A) and DAPI (Figure 2-4B).

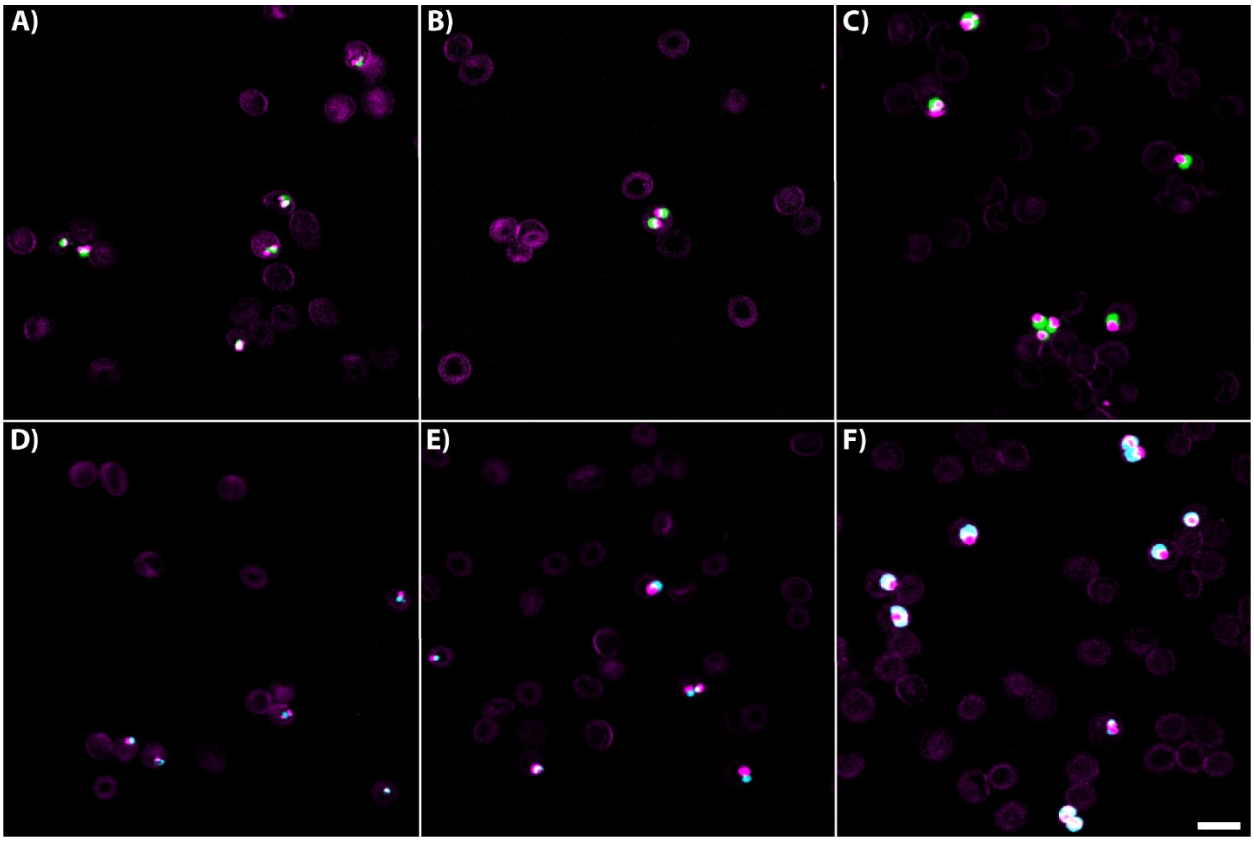

Figure 2-3: Validation of method performance using nuclear staining dyes on cultured P. falciparum parasites at the (A and D) ring, (B and E) trophozoite, and (C and F) schizont stages. Panels A−C were stained using acridine orange; panels D−F were stained using DAPI. Magenta, THG signal; green, TPF acridine orange; cyan, TPF DAPI. Scale bar: 10 μm. Separate channel images for panels A−C can be found in Figure A-2, while separate channel images for panels D−F can be found in Figure A-3.

Using the slopes of the THG versus AO graphs, it could be seen that THGISC slightly underestimated ring (0.8186) and trophozoite (0.8170) numbers while matching the numbers obtained for schizonts (1.0085). The numbers obtained for DAPI-stained parasites showed an improvement across all stages, with the trophozoite and schizont slopes being significantly higher than for rings. The differences in parasite counts obtained by THGISC in comparison to those obtained from the fluorescent DNA probes could potentially be explained by a difference in focal planes between the two different laser sources used for excitation (780 nm Ti:sapphire vs 1150

nm OPO), which were manually switched for every experiment. As THG is an interface effect, it is significantly more sensitive to small changes in focal plane compared to bulk fluorescence. For earlier parasite stages (ring and trophozoite), it is possible that the THG excitation beam failed to encompass their smaller hemozoin crystals at the same focal plane in which fluorescence could still be seen from their nuclei.

To verify this hypothesis, an additional experiment (Figure 2-4C) was conducted using DAPI-strained trophozoites where the dye was excited using the same Ti:sapphire excitation source as before along with the OPO that is normally used for THG, this time manually switched to 1000 nm for each field, which was the shortest wavelength possible for this source. From Figure 2-4C, the precision of THGISC significantly improves (R^2 of 0.96 vs 0.88) when the same laser source is used for the comparison, demonstrating the importance of proper focal plane selection. This issue could potentially be resolved by automated autofocusing or the incorporation of three-dimensional image stacks for validation from which a maximum projection could be extracted instead of single images. However, in practical applications of our method, proper focusing using the THG image channel directly should minimize false negatives due to this effect. We implemented this approach for our patient study.

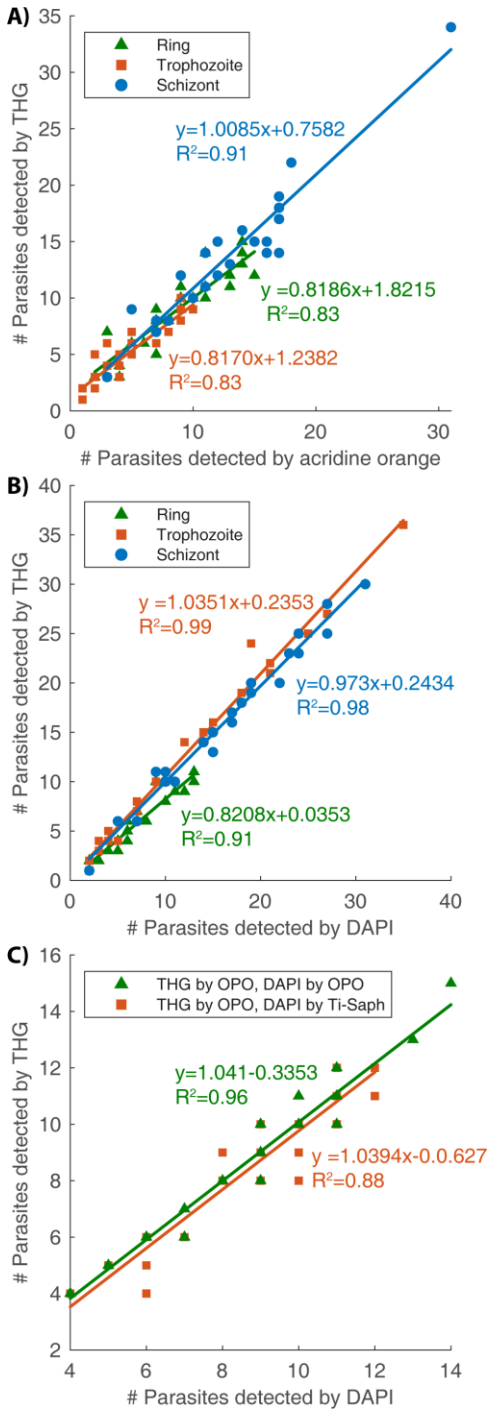

Figure 2-4: Results of method validation using fluorescent nuclear staining dyes on three different parasite lifecycle stages: ring, trophozoite, and schizont. Number of parasites obtained by our THG method vs no. of parasites detected by TPF using (A) acridine orange, (B) DAPI, and (C) DAPI with same/different excitation sources for comparison for trophozoites only. A linear regression best fit line was calculated for each data set (solid lines). N = 20−25 fields for each parasite stage.

2.4.2 Proof of Concept Using Whole-Blood Samples from Malaria Patients.

To characterize our method for potential clinical applications, we conducted THGISC screening of whole blood obtained from malaria patients. For each patient, parasite count was first established at the point of origin by microscopy of thick blood films. Parasite count was conducted in thick MBF, and the estimated white blood cell count of the patient (8000) was used in determining the parasitemia in parasite per microliter count[32] (eq 2-1):

$$\frac{n_{parasites}}{\mu L} = \frac{n_{parasites}}{n_{white\ blood\ cells}} \times \frac{8000\ white\ blood\ cells}{\mu L} \tag{2-1}$$

Using THGISC, parasite counts were established using unlabeled methanol-fixed thin blood smears to determine a percentage of parasitemia for each patient. Parasitemia was determined using eq 2-2:

$$\%\ Parasitemia = 100 * \frac{n_{Infected\ RBCs}}{n_{Total\ RBCs}} \tag{2-2}$$

An example of images obtained from two different patients can be found on Figure 2-5. We established a direct comparison for the % parasitemia obtained from our technique against the parasites per microliter that were previously clinically determined, which can be found on Figure 2-6. The relationship between the two methods can be seen to be very linear (R^2 of 0.96), demonstrating that malaria detection by THGISC provides comparable performance to the classical method of malaria detection.

The larger variation between figures obtained for patients having smaller parasite counts could potentially be explained by parasite reproduction during transit from Nigeria to Canada along with variation in sampling during preparation of the blood films. To obtain accurate results for smaller

parasite counts, it is critical for the erythrocytes to be set in a proper single layer with the blood homogeneously mixed to increase the chances of finding single isolated parasites.

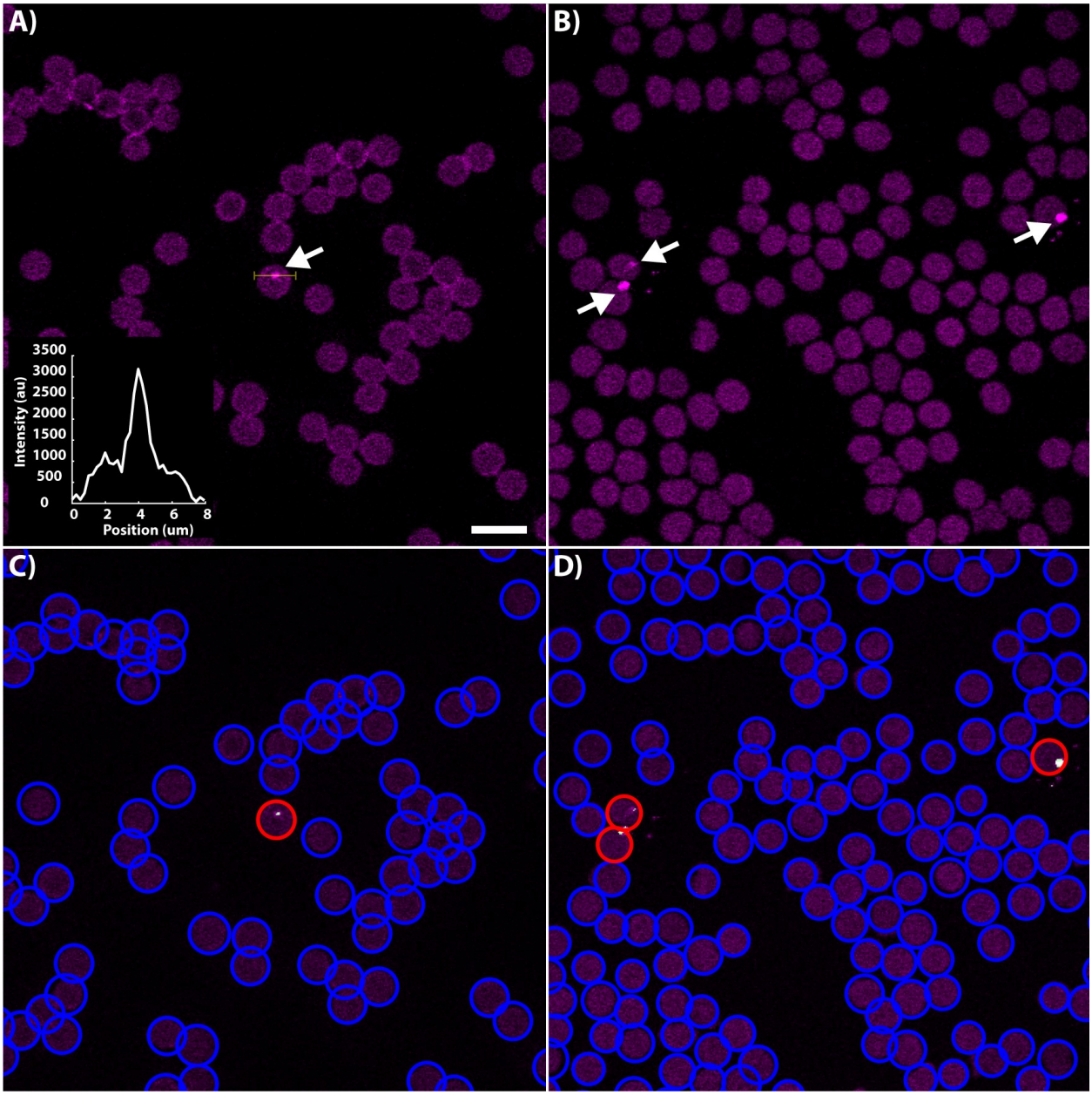

Figure 2-5: Raw and processed THGISC images for malaria detection in patient blood. (A and B) Malaria parasites (arrows) detected in whole-blood smears of two malaria patients. Inset: intensity cross section through red blood cell and hemozoin THG signals. (C and D) Red blood cell segmentation and hemozoin detection for images in panels A and B. Scale bar: 10 μm.

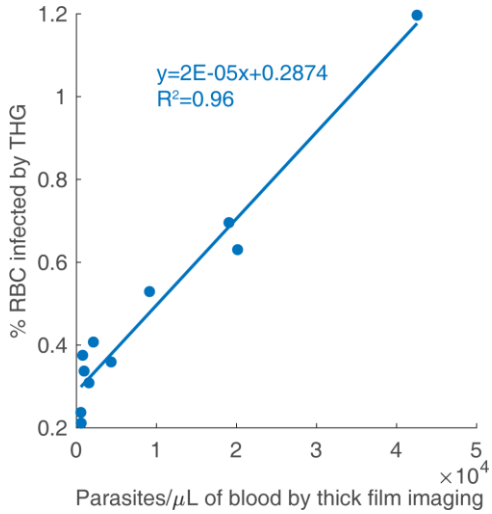

Figure 2-6: Results of method characterization using patient samples. N = 11 patients. The percentage of infected RBCs is comparable to parasitemia obtained via imaging of thick films. A linear regression best fit line was calculated (solid line).

Thanks to the use of automated scanning, the number of fields examined by THGISC could also be increased to cover most of the blood smear to increase detection probability in patients with low parasitemia. Assuming that the parasitemia rate is constant throughout a blood sample, the probability of finding a small parasite count within the millions of uninfected blood cells should follow a Poisson distribution. The higher throughput enabled by our method could allow examiners to sample significantly more fields than is normally possible due to labor constraints, which could increase the overall probability of finding at least one parasite in an entire blood smear. Such an approach could also be beneficial for parasite screening in populations to find potential asymptomatic carriers, an important checkpoint on the road to complete malaria eradication.[33] In addition, automated scanning removes the subjectivity of manual malaria blood smear reading by microscopists, while increasing the screening throughput.

The main drawback of the technique is the requirement for an ultrafast mode-locked excitation laser source for THG imaging which carries a significant initial expense. However, while a research grade tunable OPO was used in our demonstration, a much less expensive setup using a single

wavelength fiber laser based setup could provide a more economical option.[34] With the rapid progress in laser oscillator development and optimization, it is conceivable to expect such laser sources to become more widely available and accessible. Other than cost, the power requirement of the excitation laser must also be considered, rendering this method more viable for use in larger hospitals and clinics where such power can be reliably present. In such locations, a quantitative and easy-to use higher throughput method would be highly advantageous for routinely tracking patient parasitemia throughout treatment, allowing earlier health care interventions.

Another limitation of the technique is the throughput obtained via laser scanning cytometry in comparison to flow cytometry. While much faster than manual counting, a higher throughput would be desirable. Due to the nature of THG as an interface effect arising from the Gouy phase shift, the emitted signal is maximized when the sample being imaged is on the same physical scale as the laser beam.[35] For hemozoin crystals, this requires diffraction-limited beam sizes to maximize sensitivity.[20] To incorporate this approach into a flow cytometry instrument, a high-speed line scanner could potentially be adapted to continuously scan incoming RBCs. However, this would require a very tight focus of the cell flow in the axial dimension to avoid focal plane issues. Another potential solution would be the utilization of scanned Bessel beams to increase the available depth of field to ensure that parasites are detected along all axial positions in each RBC. However, a theoretical evaluation of the application of Bessel beams to THG imaging showed that it would potentially require significantly more excitation power than the standard Gaussian beams typically used in THG microscopy, which would bring additional challenges to the practical implementation.[36] Biologically, the absence of hemozoin in the very early ring stages of Plasmodium parasites (less than 6 h)[37] may be missed by THG and could explain the slightly reduced detection compared with TPF.

Malaria detection by THGISC shows promising results as compared to the current gold standard, light microscopy; however, several improvements could be made to enhance the measurements. While blood smears were prepared in methanol for each patient sample to ensure sample preservation for the entire batch after receiving of the shipment, direct measurements without fixation could provide a benefit in sensitivity. In live samples, red blood cells present a more standardized shape, resulting in better image segmentation. In addition, live samples present a lower background signal due to a reduced number of THG-emitting particles that can often be introduced during sample processing.

Treatment options for malaria patients typically consist of artemisinin-based combination therapies (ACT) where an artemisinin derivative is combined with a quinine derivative. The specific combinations, treatment duration, and dosage depend on patient factors such as endemicity, age, weight, pregnancy, and immunocompromised status, in addition to clinical diagnosis. According to the WHO,[38] symptomatic malaria patients with no signs of severity or organ dysfunction are categorized as "uncomplicated malaria", whereas "severe malaria" is defined with signs of severity and/or signs of vital organ dysfunction. It has been reported that some patients may be symptomatic at parasitemia levels as low as 0.002%, whereas patients that have developed a partial protective immunity owing to repeated exposure only show symptoms above parasitemia of 0.2%.[39] The WHO defines hyperparasitemia as >4%, a level which increases the risk of deterioration from uncomplicated to severe malaria. At a parasitemia >10%, the WHO considers the case to be severe malaria even if there is no evidence of vital organ dysfunction. We have demonstrated malaria detection at physiological levels ranging from 0.2% to 1.2%, consistent with detection using Giemsa-stained blood smear imaging. However, our method demonstrates an automated higher throughput approach in comparison to manual counting by microscopists.

Current developments in adaptive optics and three-photon fluorescence instrumentation have resulted in significant improvements in deep tissue imaging, with some commercial objectives allowing imaging at depths of up to 8 mm. Given such progress, it could be possible to apply THG-based malaria detection in vivo with imaging conducted directly in blood vessels through patient skin with epi-based detection. Such an approach was previously used for conducting human leukocyte cytometry by using THG transdermally.[40]

2.5 Conclusion

We developed a new optical detection method and demonstrated that it is a viable tool for malaria detection. By combining the sensitivity of THG imaging with high-speed motorized scanning and image processing software, malaria detection at the single red blood cell level can be achieved. The technique relies on intrinsic contrast obtained from the third order susceptibilities of hemoglobin and hemozoin to obtain both cytometry of red blood cells and detection of malaria parasites in a single channel. Unlike traditional methods, our approach does not require any labels or any preparation beyond a simple blood smear. In addition, thanks to the automated image processing, parasitemia counts can be rapidly determined in an objective manner without requiring skilled labor. While the method was shown to be sensitive to proper focusing, this could be remedied with the use of an autofocus module.

In control measurements, THGISC showed good linearity and comparable results to parasite counts obtained by two-photon fluorescence of parasite DNA stains, with a slight underestimation of smaller parasites from earlier stages (ring and trophozoite). In direct application to blood smears obtained from confirmed malaria patients, the technique showed great linearity and comparable performance to standard thick blood smear measurements. The ability

to easily and rapidly determine parasitemia offers potential not only for the easy confirmation of malaria diagnoses following symptoms, but also the tracking of treatment progress in existing patients, potentially allowing physicians to adjust medication and dosage for each individual. The technique could also be used to assist in the development of new antimalarial drugs, some of which have been theorized to be actively blocking hemozoin formation, resulting in a fatal outcome for the parasite.[41]

Acknowledgements

The authors gratefully acknowledge Discovery Grant support from the Natural Sciences and Engineering Research Council of Canada for P.W.W. (RGPIN-2018-05005) and E.G. (RGPIN-2017-05009). A.K. would like to acknowledge the Fond de Recherche du Quebec - Nature et Technologies for scholarship support. The authors thank the Bio Ventures for Global Health Organization for helping establish this collaboration. We thank the Lagos State Ministry of Health for approving the use of Health Facilities in Ikorodu, Lagos State, Nigeria where samples for this study were obtained as well as the management and staff of Ijede General Hospital and Imota Primary Health Centre, Ikorodu, Lagos, Nigeria.

2.6 References

1. Phillips, M. A.; Burrows, J. N.; Manyando, C.; van Huijsduijnen, R. H.; Van Voorhis, W. C.; Wells, T. N. C. *Nat. Rev. Dis Primers* **2017**, *3*, 17050.
2. *World Malaria Report 2017*; World Health Organization: Geneva, Switzerland, 2017.
3. Miller, L. H.; Ackerman, H. C.; Su, X. Z.; Wellems, T. E. *Nat. Med.* **2013**, *19* (2), 156−67.
4. White, N. J.; Pukrittayakamee, S.; Hien, T. T.; Faiz, M. A.; Mokuolu, O. A.; Dondorp, A. M. *Lancet* **2014**, *383* (9918), 723−735.
5. Cowman, A. F.; Healer, J.; Marapana, D.; Marsh, K. *Cell* **2016**, *167* (3), 610−624.
6. Mathison, B. A.; Pritt, B. S. *J. Clin. Microbiol.* **2017**, *55* (7), 2009−2017.
7. Hathiwala, R.; Mehta, P. R.; Nataraj, G.; Hathiwala, S. *J. Infect Public Health* **2017**, *10* (6), 824−828.
8. Wilson, M. L. *Arch. Pathol. Lab. Med.* **2013**, *137* (6), 805−11.
9. Britton, S.; Cheng, Q.; McCarthy, J. S. *Malar. J.* **2016**, *15*, 88.
10. Kolluri, N.; Klapperich, C. M.; Cabodi, M. *Lab Chip* **2018**, *18* (1), 75−94.
11. Ragavan, K. V.; Kumar, S.; Swaraj, S.; Neethirajan, S. *Biosens. Bioelectron.* **2018**, *105*, 188−210.
12. Coronado, L. M.; Nadovich, C. T.; Spadafora, C. *Biochim. Biophys. Acta, Gen. Subj.* **2014**, *1840* (6), 2032−41.
13. Delahunt, C.; Horning, M. P.; Wilson, B. K.; Proctor, J. L.; Hegg, M. C. *Malar. J.* **2014**, *13*, 147.
14. Pirnstill, C. W.; Cote, G. L. *Sci. Rep.* **2015**, *5*, 13368.
15. Lukianova-Hleb, E. Y.; Campbell, K. M.; Constantinou, P. E.; Braam, J.; Olson, J. S.; Ware, R. E.; Sullivan, D. J., Jr.; Lapotko, D. O. *Proc. Natl. Acad. Sci. U. S. A.* **2014**, *111* (3), 900−5.
16. Lukianova-Hleb, E.; Bezek, S.; Szigeti, R.; Khodarev, A.; Kelley, T.; Hurrell, A.; Berba, M.; Kumar, N.; D'Alessandro, U.; Lapotko, D. *Emerging Infect. Dis.* **2016**, *22* (2), 344−344.
17. Burnett, J. L.; Carns, J. L.; Richards-Kortum, R. *Biomed. Opt. Express* **2015**, *6* (9), 3462−74.

18. Weigelin, B.; Bakker, G. J.; Friedl, P. *J. Cell Sci.* **2016**, *129* (2), 245−55.

19. Belisle, J. M.; Costantino, S.; Leimanis, M. L.; Bellemare, M. J.; Bohle, D. S.; Georges, E.; Wiseman, P. W. *Biophys. J.* **2008**, *94* (4), L26−8.

20. Tripathy, U.; Giguere-Bisson, M.; Sangji, M. H.; Bellemare, M. J.; Bohle, D. S.; Georges, E.; Wiseman, P. W. *Anal. Bioanal. Chem.* **2013**, *405* (16), 5431−40.

21. Pozarowski, P.; Holden, E.; Darzynkiewicz, Z. *Methods Mol. Biol.* **2006**, *319*, 165−92.

22. Pozarowski, P.; Holden, E.; Darzynkiewicz, Z. *Methods Mol. Biol.* **2012**, *931*, 187−212.

23. Han, Y.; Gu, Y.; Zhang, A. C.; Lo, Y. H. *Lab Chip* **2016**, *16* (24), 4639−4647.

24. Trager, W.; Jensen, J. *Science* **1976**, *193* (4254), 673−675.

25. Preibisch, S.; Saalfeld, S.; Tomancak, P. *Bioinformatics* **2009**, *25* (11), 1463−5.

26. Chang, C. F.; Yu, C. H.; Sun, C. K. *Journal of biophotonics* **2010**, *3* (10−11), 678−85.

27. Clay, G. O.; Millard, A. C.; Schaffer, C. B.; Aus-Der-Au, J.; Tsai, P. S.; Squier, J. A.; Kleinfeld, D. *J. Opt. Soc. Am. B* **2006**, *23* (5), 932−950.

28. Saytashev, I.; Glenn, R.; Murashova, G. A.; Osseiran, S.; Spence, D.; Evans, C. L.; Dantus, M. *Biomed. Opt. Express* **2016**, *7* (9), 3449−3460.

29. Egan, T. J. J. *Inorg. Biochem.* **2002**, *91* (1), 19−26.

30. Shute, G. T.; Sodeman, T. M. *Bull. World Health Organ.* **1973**, *48* (5), 591−596.

31. Hyman, B. C.; Macinnis, A. J. *J. Parasitol.* **1979**, *65* (3), 421−5.

32. *DPDx - Laboratory Identification of Parasites of Public Health Concern. Determination of Parasitemia;* Centers for Disease Control and Prevention: Atlanta, GA, 2014.

33. Krampa, F. D.; Aniweh, Y.; Awandare, G. A.; Kanyong, P. *Diagnostics* **2017**, *7* (3), 54.

34. Millard, A. C.; Wiseman, P. W.; Fittinghoff, D. N.; Wilson, K. R.; Squier, J. A.; Muller, M. *Appl. Opt.* **1999**, *38* (36), 7393−7397.

35. Beaurepaire, E.; Débarre, D.; Olivier, N. THG Microscopy of Cells and Tissues: Contrast Mechanisms and Applications. In *Second Harmonic Generation Imaging*; CRC Press: Boca Raton, FL, 2016; pp 70−99.

36. Olivier, N.; DeBarre, D.; Mahou, P.; Beaurepaire, E. *Opt. Express* **2012**, *20* (22), 24886−902.

37. Delahunt, C.; Horning, M. P.; Wilson, B. K.; Proctor, J. L.; Hegg, M. C. *Malar. J.* **2014**, *13*, 147.

38. *Guidelines for the Treatment of Malaria*; World Health Organization: Geneva, Switzerland, 2015.

39. Hanscheid, T. *Clin. Lab. Haematol.* **1999**, *21* (4), 235−45.

40. Wu, C. H.; Wang, T. D.; Hsieh, C. H.; Huang, S. H.; Lin, J. W.; Hsu, S. C.; Wu, H. T.; Wu, Y. M.; Liu, T. M. *Sci. Rep.* **2016**, *6*, 37210.

41. Kumar, S.; Guha, M.; Choubey, V.; Maity, P.; Bandyopadhyay, U. *Life Sci.* **2007**, *80* (9), 813−28.

Preface to Chapter 3

In the previous chapter, we presented a new malaria detection method implementing nonlinear microscopy to the field of hematology. We implemented third harmonic generation (THG) microscopy to detect red blood cells through their hemoglobin content and malaria infected cells via the metabolic byproduct of the malaria parasite, hemozoin. During the validation of this technique, we utilized the nonlinear modality of two photon fluorescence to visualize the nuclear staining of the parasite.

In this chapter, we demonstrate a novel technique for virtual histology of rabbit vocal folds using a combination of multimodal nonlinear microscopy and nano computed tomography. Specifically, we now utilize two photon fluorescence to probe the native fluorescence of elastic fibers, muscle tissue and blood vessels in addition to second harmonic generation to visualize the underlying collagen structure of the vocal fold lamina propria. Both nonlinear microscopy and nano-computed tomography provided detailed three-dimensional histological information of the vocal fold microarchitecture, which was used to create volume renders of anatomical relevance.

This chapter has been published as an article in *Biomedical Optics Express* (Kazarine et al. 2019).

3 Multimodal Virtual Histology of Rabbit Vocal Folds by Nonlinear Microscopy and Nano Computed Tomography

Alexei Kazarine,[1] Ksenia Kolosova,[2] Angelica A. Gopal,[1,3] Huijie Wang,[4,5] Rui Tahara,[6] Almoaidbellah Rammal,[7,8] Karen Kost,[7] Luc Mongeau,[4] Nicole Y. K. Li-Jessen[5,7,9] and Paul W. Wiseman[1,2,*]

[1]Department of Chemistry, McGill University, 801 Sherbrooke St. West, Montreal, QC H3A 0B8, Canada
[2]Department of Physics, McGill University, 3600 University St., Montreal, QC, H3A 2T8, Canada
[3]Department of Physiology, McGill University, 3655 Promenade Sir William Osler, Montreal, H3G 1Y6, Canada
[4]Department of Mechanical Engineering, McGill University, 817 Sherbrooke St. West, Montreal, QC H3A 0C3, Canada
[5]School of Communication Sciences and Disorders, McGill University, 2001 McGill College Ave., Montreal, QC H3A 1G1, Canada
[6]Redpath Museum, McGill University, 859 Sherbrooke St. West, Montreal, QC H3A 0C4, Canada
[7]Department of Otolaryngology – Head and Neck Surgery, McGill University, 1001 Decarie Blvd., Montreal, QC, H4A 3J1, Canada
[8]Department of Otolaryngology – Head and Neck Surgery, King Abdul-Aziz University, Jeddah, Saudi Arabia.
[9]Department of Biomedical Engineering, McGill University, 3775 University St., Montreal H3A 2B4, Canada

3.1 Abstract

Human vocal folds (VFs) possess a unique anatomical structure and mechanical property for human communication. However, VFs are prone to scarring as a consequence of overuse, injury, disease or surgery. Accumulation of scar tissue on VFs inhibits proper phonation and leads to partial or complete loss of voice, with significant consequences for the patient's quality of life. VF regeneration after scarring provides a significant challenge for tissue engineering therapies given the complexity of tissue microarchitecture. To establish an effective animal model for VF injury and scarring, new histological methods are required to visualize the wound repair process of the tissue in its three-dimensional native environment. In this work, we propose the use of a combination of nonlinear microscopy and nanotomography as contrast methods for virtual histology of rabbit VFs. We apply these methods to rabbit VF tissue to demonstrate their use as

alternatives to conventional VF histology that may enable future clinical studies of this injury model.

3.2 Introduction

Human vocal folds have a distinctive tri-layered mucosal structure with rich extracellular matrix substances such as collagen, elastin and hyaluronan [1]. The delicate structure of the VFs makes them prone to scarring as a consequence of injury, disease or surgery [2]. The thicker scar tissue inhibits proper phonation and leads to voice disorders or even the loss of voice, which significantly hampers the patient's communicative ability and quality of life [3]. Surgical attempts to remove the scar often result in additional, iatrogenic scarring [4]. While studies have been conducted on potential therapies, effective treatment for the prevention or removal of VF scarring has not yet been achieved [5-8]. Proper understanding of the cellular mechanisms of the scarring process is required for the development of better treatment strategies [9].

Histology provides invaluable insight into both normal tissue physiology and disease pathology. The complex and heterogeneous structures of VF however present a unique challenge in histological analyses [10]. Histopathology remains largely unmodified since its introduction more than a century ago and continues to be based on the microscopic observation of micron-thin tissue slices stained with colored dyes. Hematoxylin and Eosin (H&E) staining, for example, has been employed since the 1800s [11]. Visualization of specific components of connective tissue can be performed using traditional immunoperoxidase or histochemical staining, such as reticulin (type III and IV collagen), Masson's trichrome (collagen and muscle), and the Verhoeff–van Gieson stain (elastic fibres and collagen) [12]. While conventional histology (Figure 3-1A) provides important ultrastructural information at the micron level, the procedure is labor-intensive since it

requires fine slicing of the tissue into thousands of individual slices, dyeing of the tissue, and manual microscopic observation of each slice to locate features of interest [13]. Since native tissues are organized in three-dimensional (3D) structures, a two-dimensional slice can only provide limited local information. To provide an improvement over conventional histology, new methodologies must be explored to enable high resolution three-dimensional visualization of tissue ultrastructure in a form of "virtual" histology. Among potential approaches, two imaging techniques, namely nano computed tomography (CT) and nonlinear microscopy (NM), show great promise towards addressing this challenge (Figure 3-1B). While magnetic resonance imaging (MRI) has previously been used to study the scarring process of vocal fold mucosa in rats, the resolution provided by the technique is insufficient for ultrastructure visualization in three dimensions [14].

Nanotomography (also called Nano-CT) employs x-ray illumination to obtain cross sectional images of tissue as the sample is rotated on a moving stage [15]. Nano-CT's contrast is based on tissue density and sometimes enhanced with phosphotungstic acid staining when native tissue contrast is insufficient. Unlike traditional medical computed tomography or microtomography [16], nanotomography employs x-ray optics and small focal volumes to obtain isotropic submicron volume elements (voxels). Using this volumetric data, a virtual three-dimensional model of the sample can be reconstructed and "re-sliced" as desired for histological observation. Most recently, x-ray nanotomography has been used for 3D multiscale imaging of human vocal folds [17].

Nonlinear microscopy is a laser scanning imaging technique that exploits multiphoton absorption of IR photons from ultrafast laser sources to enable deep tissue imaging [18]. This method offers a variety of label-free contrast mechanisms thanks to multiple simultaneous light-matter interactions

that occur in the sample upon illumination with ultrashort laser pulses from IR lasers. Two photon autofluorescence (TPAF) imaging can reveal native intrinsic fluorophores in tissue such as elastin, NADH and hemoglobin amongst others [19]. Second harmonic generation (SHG) is a nonlinear scattering process in which two incident photons are combined into a single emitted photon having twice the incident laser light frequency [20]. This process can only occur in dense, non-centrosymmetric media and was initially discovered using inorganic crystalline materials. In biological tissue, SHG has been demonstrated to be significant in collagen and muscle and is now often used as the gold standard for collagen imaging [21]. We have previously utilized nonlinear microscopy to investigate tissue sections of human [22], rat [23], porcine [24, 25], and rabbit vocal folds [26].

Traditional nonlinear microscopy enables imaging depths in biological tissues down to ~1 mm in the best case scenario, at which point it is significantly limited by scattering of the incident excitation beam [27]. To increase the imaging depth beyond a millimeter, new sample processing methods have been developed to significantly reduce tissue scattering [28]. These optical clearing techniques employ an immersion medium to reduce or eliminate refractive index differences between tissue components, rendering the tissue transparent. Refractive index matching is typically preceded by removal of lipids to reduce the refractive index of the tissue. Various optical clearing techniques have been developed, with key differences being the choice of delipidation method and refractive index matching solution [29]. Aqueous methods, such as CUBIC, are easy to implement and are compatible with a wide range of fluorescent dyes and proteins. Such methods are however limited to small samples, result in sample enlargement, and require significant preparation time [30]. To combat this, hydrogel embedding methods, such as CLARITY, have been developed that provide faster aqueous clearing of larger samples although at an increased cost [31]. Organic solvent-based methods such as uDISCO result in less expensive and faster tissue

clearing [32]. However, the dehydration steps inherent in solvent based methods can often result in significant tissue shrinkage and loss of lipids. The choice of clearing method therefore directly depends on the desired application. For the purposes of virtual histology, uDISCO appears to be an optimal choice due to its low cost, high efficiency and good preservation of intrinsic fluorescent proteins. In combination with tissue clearing, nonlinear microscopy can provide mm^3 sized volumetric imaging with submicron lateral and micron-sized axial resolution, rendering it of great interest in virtual histology.

In this work, we present a new histological approach of combining nano-CT with nonlinear microscopy and uDISCO tissue clearing to obtain three-dimensional virtual models of the vocal folds. This virtual histology is important for determining normal vocal fold physiology prior to the establishment of a wound model for the study of vocal fold scarring and regeneration. In comparison with normal histology, our approach enables a three-dimensional view of the vocal fold ultrastructure, with easy determination of tissue features such as the cartilage, lamina propria layers, muscles and blood capillaries that are important structures to visualize for wound healing studies. The volume renders can easily be separated into cross sectional planes that are familiar to anatomic pathologists, enabling detailed observation of regions of interest.

This study represents the first instance of whole rabbit vocal fold histological imaging, enabled by optical clearing, nonlinear microscopy, and nano-CT. This new, integrated histological approach could bring significant insights in the three-dimensional anatomical organization and physiology of normal and diseased vocal fold tissues, which has traditionally only been examined in two dimensions through irreversible mechanical sectioning of tissue slices.

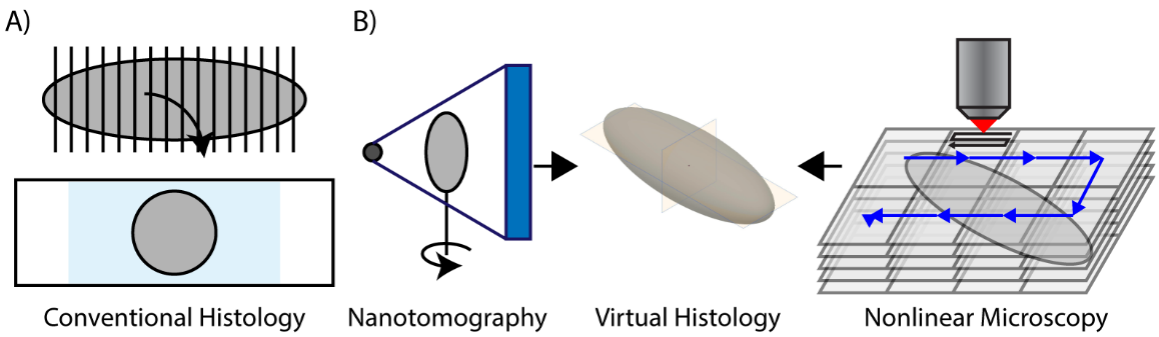

Figure 3-1: Schematic comparison of the concepts of conventional histology (A) with virtual histology by nanotomography and nonlinear microscopy (B).

3.3 Materials and Methods

3.3.1 Animal Study

Ethics approval was obtained from the McGill University Animal Care Committee (Protocol number DOW FACCs 2014-7556). All animal handling and experimental procedures were carried out in accordance with the National Institutes of Health (NIH) guidelines for care and use of laboratory animals. A rabbit model was selected as it is a well-documented model commonly used to study vocal fold injuries [33]. Rabbits possess larger vocal folds than smaller laboratory animals such as rats [34], enabling easier and more reliable vocal fold surgery. For the purposes of this study, one New Zealand white rabbit received a surgical injury on the left vocal fold while the right was kept intact as a control.

The animal was sacrificed 42 days after surgical intervention and its larynx was excised for ex-vivo high resolution nano-CT and nonlinear microscopy imaging. For coarse, full size CT imaging, one intact rabbit larynx was excised from a rabbit carcass obtained from a commercial source.

3.3.2 Tissue Clearing

For nonlinear microscopy, the vocal cords were dissected from the rabbit larynx sample to reduce tissue thickness to 2 mm to match the microscope objective working distance. Optical clearing was conducted using the established uDISCO clearing protocol [32]. Laboratory reagents were obtained from Millipore Sigma (ON, Canada) unless otherwise indicated. Briefly, the sample was first dehydrated through sequential passages in 30%, 50%, 70%, 80%, 90%, 96% v/v tert-butanol solutions in distilled water before incubation in a refractive index matching solution consisting of a mixture of benzyl alcohol (BA), benzyl benzoate (BB) and diphenyl ether (DPE) in a 2:1:4 (BA-BB-DPE) v/v solution. Concurrently, α-tocopherol was added at a final concentration of 0.4% v/v as an oxygen scavenger. Each clearing step was maintained for one day at room temperature. Figure 3-2A shows the rabbit vocal folds after dissection while Figure 3-2B shows the same sample after optical clearing.

Custom imaging chambers were designed and fabricated to allow a complete encapsulation of the sample immersed in the refractive index matching solution while avoiding physical contact with the microscope objective during nonlinear imaging. The chambers consist of polydimethylsiloxane (PDMS) spacers cast from a machined aluminum mold that were attached to microscope slides during the casting process, resulting in a permanent bond. Once the sample is introduced to the chamber, enough refractive index matching solution is added to slightly overfill the chamber and a no. 1.5 coverslip was then used to close the chamber and ensure a seal by surface tension. The isolated sample could then be safely manipulated and imaged by nonlinear microscopy. A render of the sample encapsulated in a chamber is shown in Figure 3-2C.

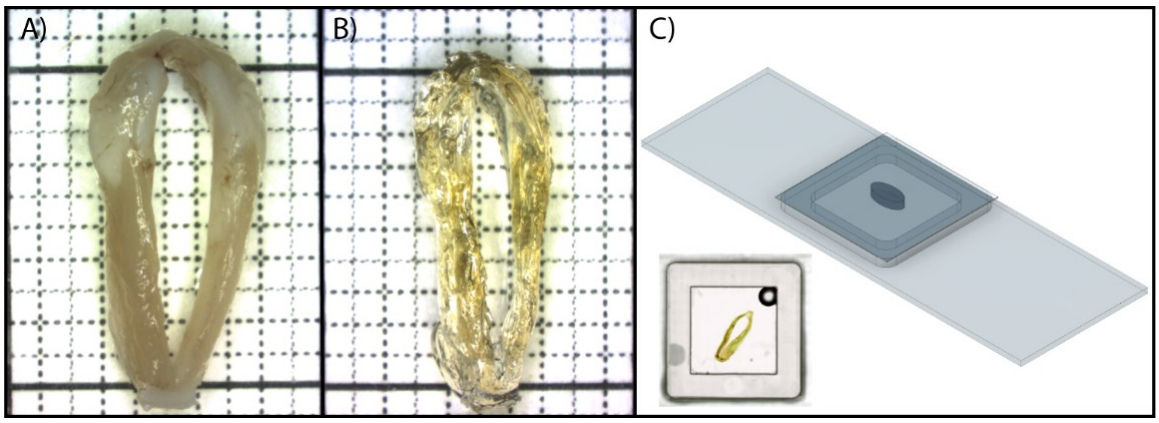

Figure 3-2: Optical clearing of rabbit vocal folds. (A) Uncleared vocal fold tissue after dissection, (B) the same tissue after clearing with the uDISCO protocol, (C) render of imaging chamber used for nonlinear microscopy of the cleared tissue, inset showing brightfield microscopy image of the sample and chamber. Dotted lines in (A) and (B) are spaced 1mm apart.

3.3.3 Nanotomography

For coarse nanotomography, a full rabbit larynx was dissected, dehydrated with passages to 70% ethanol and stained with an alcoholic solution of phosphotungstic acid (PTA) to enhance soft tissue contrast [35]. For high resolution nanotomography, the same rabbit larynx sample that was previously optically cleared and imaged by nonlinear microscopy was immersed in ethanol passages to 70% ethanol before PTA staining.

Nanotomography was conducted using a Zeiss Xradia Versa 520 x-ray microscope (Carl Zeiss Canada Ltd., ON, Canada). For full laryngeal imaging, an optical magnification of 0.4x was used to achieve an isotropic voxel size of 12 μm. For high resolution imaging of the rabbit vocal fold, a 4x optical magnification was employed for a final voxel size of 0.8 μm. Virtual models of the nanotomography image stacks were created and analyzed using Dragonfly (Object Research Systems, QC, Canada). This software enabled easy determination of cross sectional planes by directly selecting corresponding x/y/z axes after volume rendering.

3.3.4 Nonlinear Microscopy

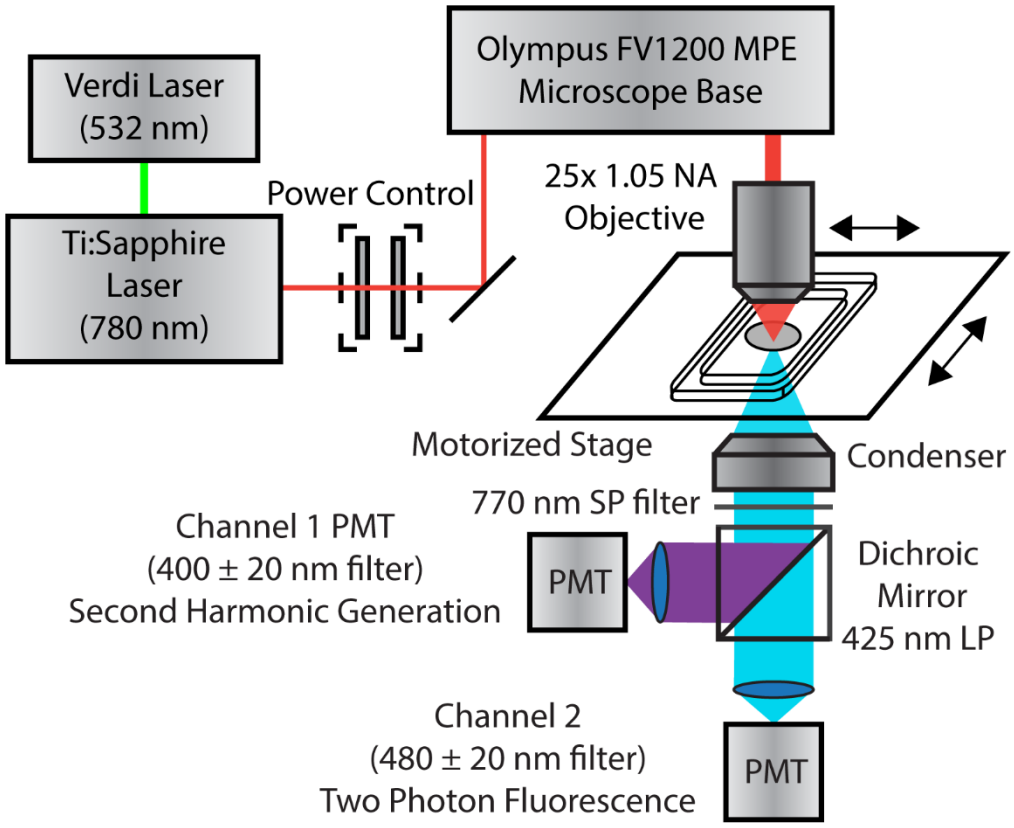

Figure 3-3: A schematic diagram of the nonlinear microscopy imaging system. The Verdi (532 nm) laser pumps the Ti:Sapphire laser (780 nm) that is directed into the microscope base with computer control over the power. A 25X 1.05NA water immersion objective is used to focus the excitation light onto the sample. Forward detection was achieved using a condenser lens, where the emission was separated into two channels: the second harmonic generation channel (Channel 1) and the two-photon fluorescence channel (Channel 2) and subsequently detected by photomultipliers (PMTs).

Nonlinear microscopy was performed using a customized multiphoton microscope (Figure 3-3) based on a FV1200 MPE microscope base (Olympus Canada Inc, ON, Canada). Excitation with 780 nm laser light was achieved by a Ti:Sapphire laser (Mira 900F, Coherent, CA) pumped by a 532 nm laser (Verdi V18, Coherent, CA). The excitation laser provided 200 fs pulses at a 76 MHz repetition rate. Laser power was measured, and computer controlled immediately prior to entry to the microscope by a custom built variable attenuator consisting of a rhomb retarder (FR600HM,

Thorlabs, NJ) mounted on a motorized rotational stage (PRM1Z8, Thorlabs, NJ, USA) and a linear Glan-Laser polarizer (GL10, Thorlabs, NJ). Imaging was conducted using a 25x 1.05 NA water immersion objective (XLPL25XWMP(F), Olympus Canada Inc, ON, Canada) with a working distance of 2 mm. Emission light was collected with a dry top lens condenser, split by a long pass (LP) dichroic mirror (T425lpxr, Chroma Technology, VT) and directed into two detection photomultipliers (PMTs) for simultaneous detection of second harmonic generation (380-420 nm filter, ET400/40x, Chroma Technology, VT) and two-photon fluorescence (460-500 nm filter, BA 460-500, Olympus Canada Inc, ON, Canada). A 770 nm IR blocking short pass (SP) filter (FF01-770/SP32, Semrock, NY) was placed immediately below the condenser to prevent the excitation light from reaching the detectors. The sample was mounted on a motorized stage to conduct three-dimensional mosaic imaging. Adjacent image fields were stitched using Fluoview (Olympus Canada Inc, ON, Canada) to obtain 3D image stacks, that were rendered as virtual models in Imaris (Bitplane Inc., South Windsor, CT) and Dragonfly (Object Research Systems, QC, Canada).

3.4 Results and Discussion

Virtual histology combines the principles of optical sectioning and three-dimensional volume rendering to obtain high resolution histological information from intact tissue. Instead of physical slicing, virtual slicing through the rendering software allows easy manipulation for rapid interpretation of histological data. With recent advances in both central and graphical processing unit technology, computing power has become inexpensive enough for such rendering to be done on standard desktop workstations. To compete with conventional histology of vocal folds, virtual histology methods must present similar resolution and contrast along with deep tissue penetration to enable efficient 3D data collection.

Three-dimensional histology of animal vocal folds is critical in establishing their use as a wound healing model for vocal fold injury and repair. While the rabbit model has been used to evaluate different potential vocal fold regeneration therapies [36], the data obtained in these studies was limited to traditional histology such as H&E, which cannot provide the entire three-dimensional tissue landscape when it comes to a spatial understanding of wound healing. By using virtual histology, the entire wound area could be observed and compared across animals over time. Such capability is important to standardize the location and size of the injury and to evaluate the wound healing outcome in a more consistent manner. Before such studies can be conducted, it is important to determine the ultrastructure of normal rabbit vocal folds and verify that the proposed virtual histology methods provide adequate resolution and contrast. To achieve this, we have evaluated two potential avenues for conducting virtual histology of rabbit vocal fold tissue: nanotomography and nonlinear microscopy, each of which presents its own advantages and limitations.

3.4.1 Virtual Histology of an Entire Rabbit Larynx via Nanotomography

Nanotomography employs a combination of a rotating stage with x-ray imaging and computer processing to obtain a three-dimensional image stack with a final submicron voxel size and contrast based on tissue density. The flexibility of this system lies in its ability to image large samples at varying resolution, allowing us to capture both lower resolution coarse renders of entire organs followed by detailed submicron resolution imaging of volumes of interest.

We first imaged an entire rabbit larynx using a coarser magnification (12 μm^3 voxels) to obtain a render of the entire vocal folds and their surrounding tissues (Figure 3-4A). In the transverse plane (Figure 3-4B), the vocal folds and surrounding cartilage are immediately visible, with easy software-controlled sectioning enabling discrete observation of the tissue types.

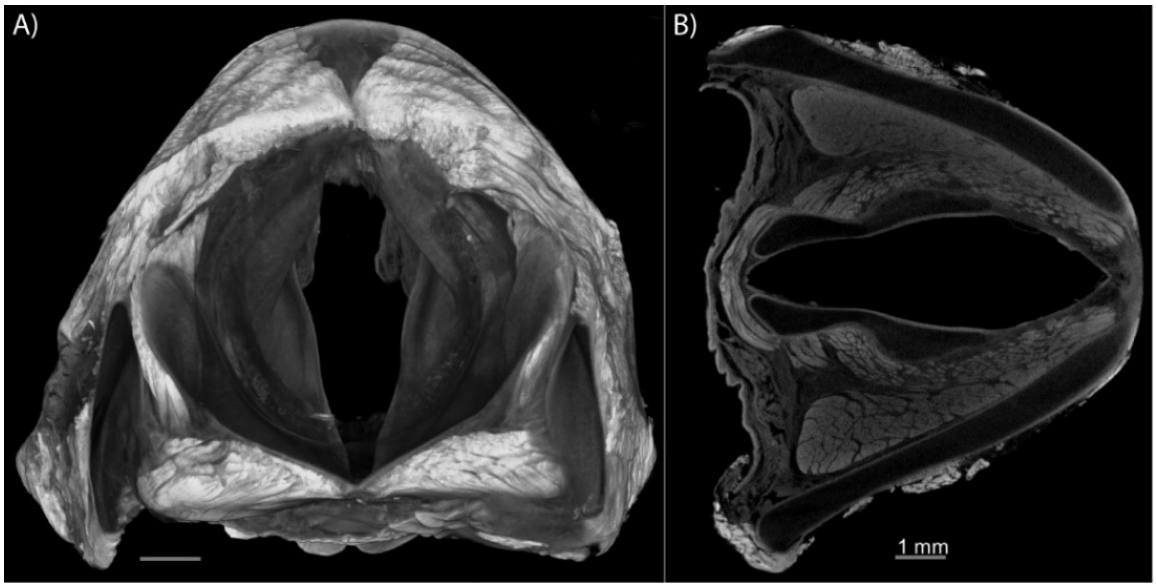

Figure 3-4: Coarse tomography of a rabbit larynx. (A) 3D volume render of the entire rabbit larynx. (B) Cross sectional plane across the rabbit larynx. Scale bars are 1 mm.

Figure 3-5 demonstrates a comparison between virtual histology with coarse nanotomography (Figure 3-5A) and classical histology with H&E staining (Figure 3-5B) for coronal sections of vocal fold tissue. In H&E sections, the contrast is provided by tissue components that are either basophilic or acidophilic, resulting in color differences between dark purple (cell nuclei) and pink (cytoplasm and extracellular matrix components). Using tomography, the tissue components are contrast distinguished by their density, with adequate separation in signal levels between cartilage, muscle and the soft tissue of the vocal fold lamina propria (basement membrane) that can be easily distinguished (Figure 3-5A).

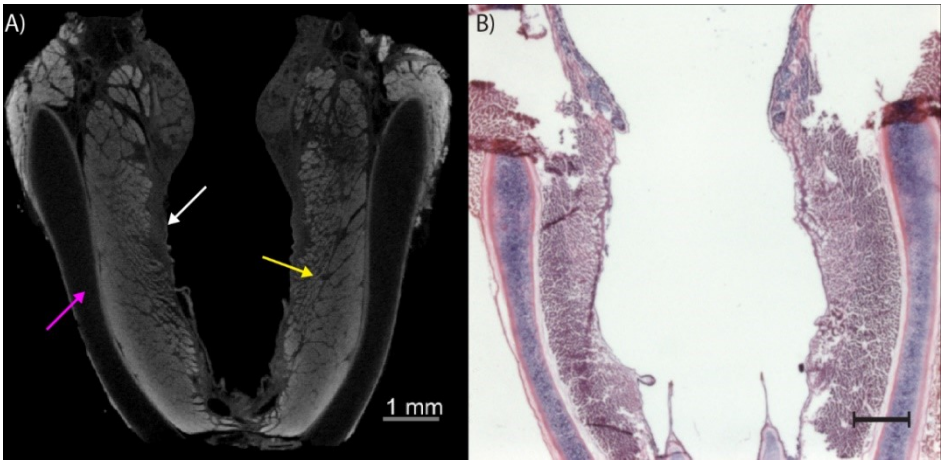

Figure 3-5: Comparison of histology methods applied to rabbit vocal folds. (A) Virtual histology by Nano-CT. (B) Classical histology example by hematoxylin and eosin staining of a thin tissue slice of rabbit larynx. White arrow indicates the vocal fold lamina propria, yellow arrow points to muscle while the magenta arrow denotes an area of cartilage. Scale bars are 1 mm.

3.4.2 Virtual Histology of a Dissected Rabbit Larynx via Nonlinear Microscopy and Nanotomography

Nonlinear microscopy is a deep tissue optical imaging technique commonly used for the observation of thick specimens. By using femtosecond pulsed near-infrared excitation lasers, nonlinear microscopy allows for inherent optical sectioning and an imaging depth of nearly 1 mm before loss of signal due to scattering and attenuation. This imaging depth can be significantly extended using optical clearing techniques, which render the tissue transparent and greatly reduce scattering and excitation power loss. If adequate tissue clearing is performed, the imaging depth is then only limited by the working distance of the microscope objective. In our study, we used the uDISCO clearing protocol to obtain rapid optical clearing of rabbit vocal fold tissue in less than a week. Due to the 2 mm working distance of our objective lens, the rabbit larynx sample was first dissected to fit this size before imaging via nonlinear microscopy.

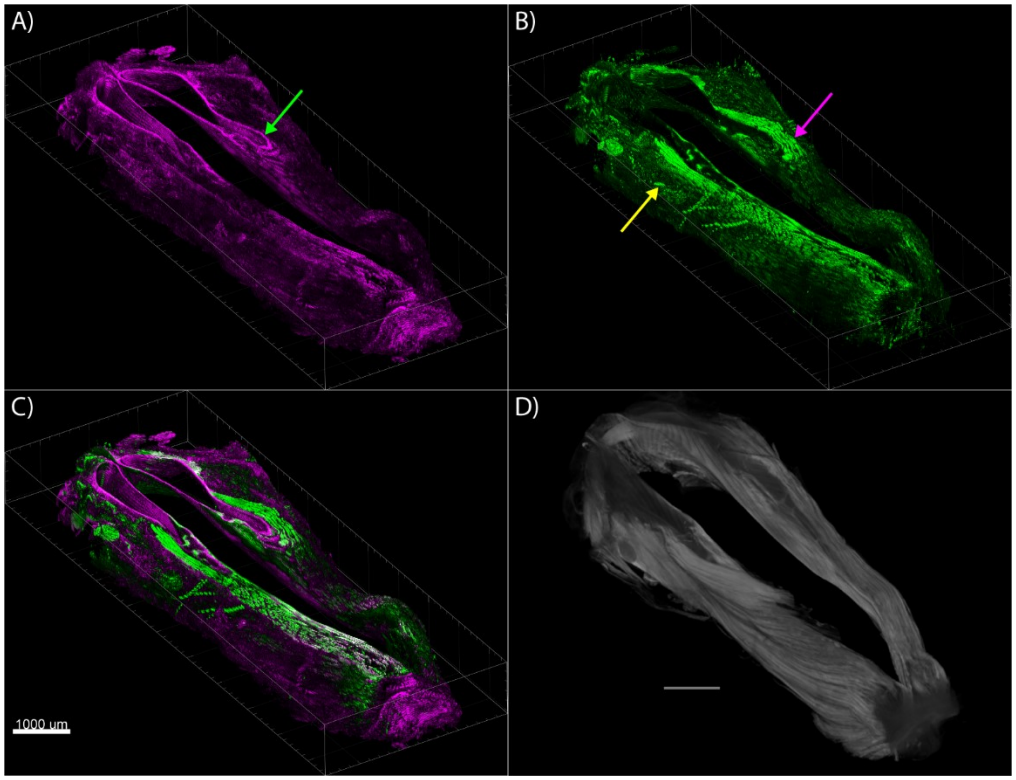

Figure 3-6: 3D volume render of dissected rabbit vocal folds imaged by nonlinear microscopy and nanotomography (coarse). (A) Channel 1: Second Harmonic Generation highlighting collagen type I & III fibers. Green arrow highlights structural laryngeal cartilage. (B) Channel 2: Two Photon Autofluorescence showing primarily muscle cell NADH (magenta arrow) and blood vessel (yellow arrow). (C) Composite of (A) and (B). (D) Coarse nanotomography of the same dissected rabbit larynx performed after nonlinear microscopy. (A-C) are at the same scale. Scale bars are 1 mm.

To compare nonlinear microscopy to nanotomography on the same sample, we first performed nonlinear imaging on an unlabeled rabbit larynx sample using SHG and TPAF imaging, two contrast mechanisms that exploit inherent tissue properties. SHG allows the visualization of collagen type I & III fibers [37] in vocal folds, while TPAF centered around emission wavelength of 480 nm highlights elastic fibers and NADH in muscle cells [18]. After nonlinear imaging, we passaged the sample into ethanol to prepare it for nanotomography.

Full size volume renders of the vocal folds and surrounding tissue imaged by nonlinear microscopy and coarse nanotomography can be found in Figure 3-6. Nonlinear imaging was performed at x-y pixel sizes of 0.5 μm with 50 μm steps between z slices, while the coarse nanotomography utilized a voxel size of 12 μm. The contrast difference between nonlinear microscopy (Figure 3-6A-C) and nanotomography (Figure 3-6D) is directly visible even at the coarse resolution utilized in nanotomography. The SHG volume (Figure 3-6A) highlights the collagen structure of the laryngeal cartilage and within the VF lamina propria. The TPAF render (Figure 3-6B) primarily shows muscle fibers via autofluorescence of NADH along with evidence of blood vessels via red blood cell and elastic lining autofluorescence.

3.4.3 Tissue Ultrastructure Revealed by High Resolution Nanotomography

Nanotomography of the dissected rabbit vocal folds (see Figure 3-6D) was first performed at a coarse resolution with a voxel size of 12 μm to facilitate fast visualization of the vocal fold and surrounding tissues for a broad overview of the sample. Using this overview, the vocal fold volumes were identified and re-imaged at high resolution (0.8 μm voxel size) to push the resolution limits of nanotomography (Figure 3-7A). When virtually cross-sectioned, the resulting volume allows easy observation of both cartilage (Figure 3-7B) and vocal fold histology (Figure 3-7C), including epithelium, lamina propria and muscle fibers. This demonstrates the powerful capabilities of nanotomography to visualize tissue ultrastructure directly at a three-dimensional level without destruction of the delicate VF tissue from its native state.

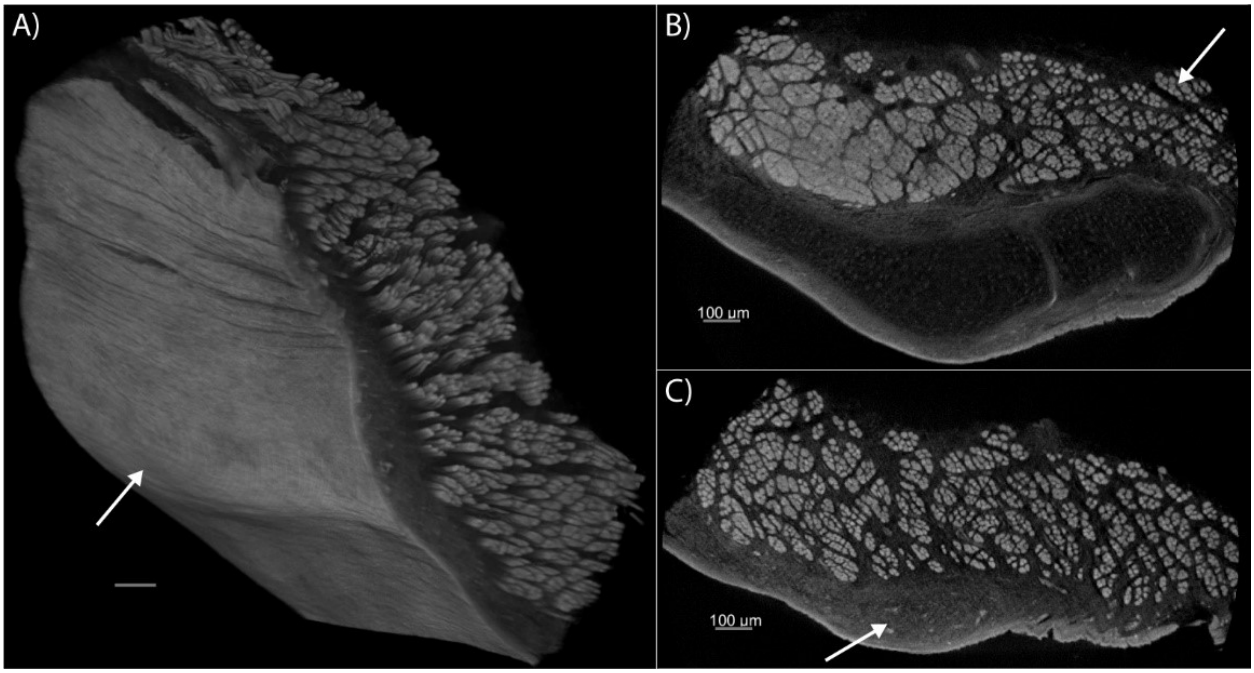

Figure 3-7: High resolution nanotomography of rabbit vocal fold tissue and the surrounding area. (A) 3D volume render of the epithelium (highlighted by white arrow), vocal fold lamina propria, and surrounding muscle. (B) Cross section of cartilage and muscle (highlighted by white arrow) in the surrounding tissue of the vocal fold. (C) Vocal fold lamina propria (white arrow) cross section. Scale bars are 100 μm.

The main limitation of nano-CT lies in its contrast mechanism, which is based on tissue density. Staining can enhance the contrast at the soft tissue level and enable differentiation between major tissue types, similarly to the contrast obtained using H&E staining. However, without immunolabeling, neither of these techniques can provide the specificity to highlight single protein targets.

3.4.4 Cellular Details Revealed by High Resolution Nonlinear Microscopy

We also conducted high resolution nonlinear imaging of the rabbit vocal fold tissue with z-spacing of 1 μm (Figure 3-8). In the full render (Figure 3-8A), the ultrastructure of the rabbit vocal fold is directly visible, as the two contrast mechanisms highlight different layers of the tissue, including the epithelium, lamina propria (basement membrane), collagen fibers and muscle tissue.

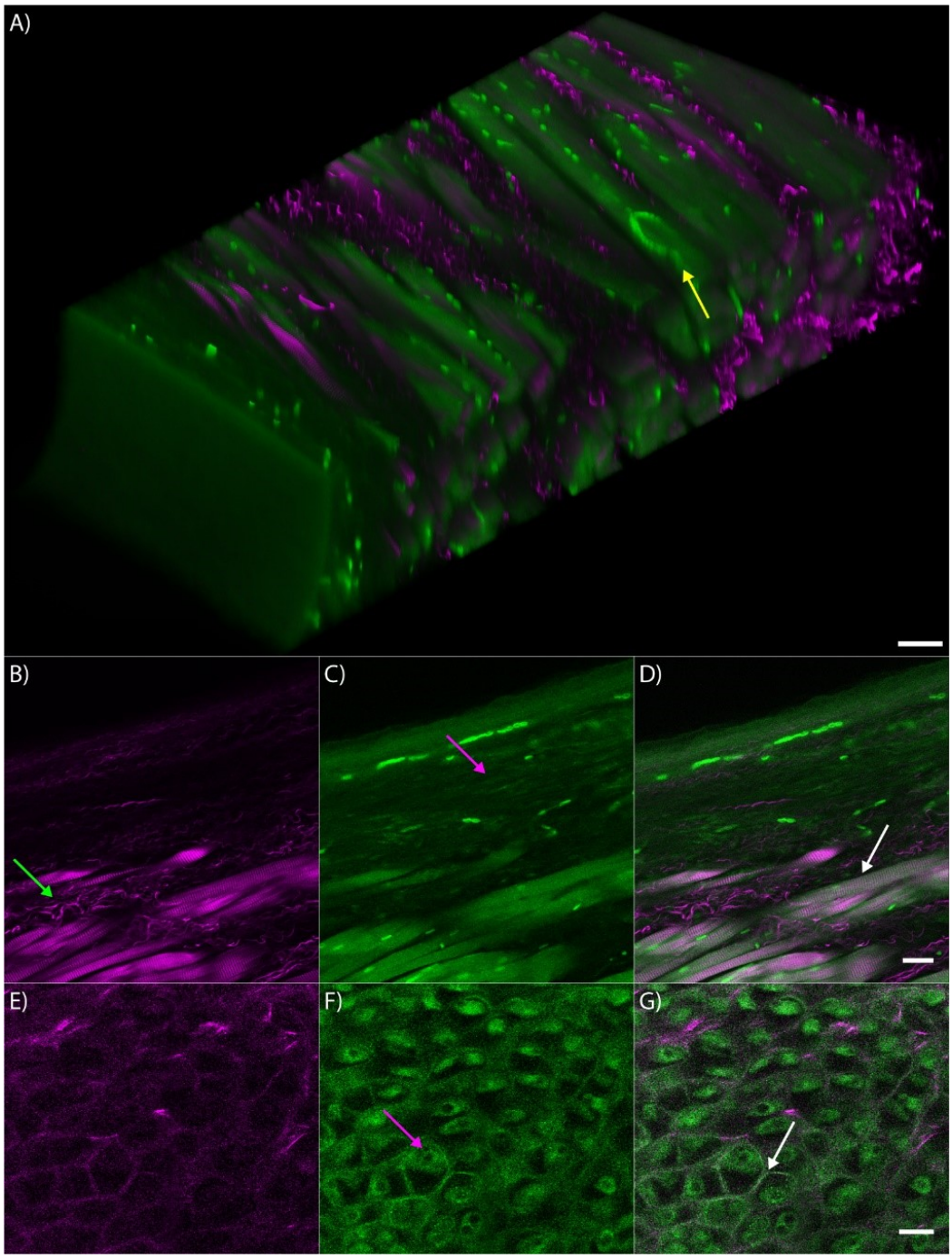

Figure 3-8: High resolution nonlinear microscopy of optically cleared rabbit vocal fold and surrounding tissue. (A) 3D Volume render combining SHG (magenta) and TPAF (green), yellow arrow highlights the presence of red blood cells via autofluorescence from hemoglobin. (B-D) Imaged area including structural collagen (green arrow in SHG channel B), vocal fold lamina propria (magenta arrow in TPAF channel C), and surrounding muscle fibers (white arrow in composite D). (E-G) Imaged area showing surrounding cartilage, where E is the SHG channel, F is the TPAF channel highlighting chondrocytes (magenta arrow), and composite G shows presence of elastic fibers (white arrow). Scale bars are 25 μm.

In the high-resolution images obtained, several tissue features are directly revealed at the cellular level. In the 480 nm detection channel, TPAF demonstrates the presence of red blood cells in a blood vessel and NADH from cells in muscle tissue (Figure 3-8B) along with chondrocytes and elastic fibers in the vocal fold cartilage (Figure 3-8C). In the 400 nm detection channel, SHG from collagen fibers and the muscle tissue itself can be seen (Figure 3-8D) along with collagen fibers and three photon fluorescence from elastic fibers visible in the cartilage. The elastic tissue shows direct correspondence between the two channels, allowing it to be distinguished from collagen fibers, which are only visible in the 400 nm channel.

The visualization of collagen fibers by SHG is dependent on the orientation of the fibers in relation to the polarization of the excitation beam. Consequently, by tightly controlling the linear polarization of the beam, the collagen structure could be further analyzed to reveal fiber orientation and aggregation [38]. This feature is beneficial for developing quantitative measures or biomarkers to characterize and monitor the health state of the tissue, such as scarring index.

Our utilization of solvent based optical clearing shrank the tissue in addition to optically clearing the tissue for deep imaging, resulting in decreased structural resolution. An approach to counteract this effect could be the use of expansion microscopy [39]. This technique utilizes polymers to expand tissues for improved visualization of smaller structures that are hidden by the diffraction limit. The implementation of expansion microscopy on entire vocal folds would however be limited by the working distance of the objective, as expanding the tissue will enlarge the sample beyond the range we could safely mount and image with our current microscope.

Other techniques that can be used to improve the optical resolution of imaging include the use of Bessel beams in two photon microscopy to improve lateral resolution at the expense of axial resolution [40]. To improve the resolution of 3D imaging, a light sheet approach can be utilized using Bessel-beam illumination, in both one [41] and two [42] photon regimes, which can also be combined with localization algorithms for super-resolution measurements [43].

While the rabbit used for the high-resolution CT and NM imaging received a surgical injury on the left vocal fold, we were unable to find any histological differences between the two vocal folds in either nano-CT, nonlinear microscopy images or traditional H&E examination. As such, the CT and NM images presented in this paper were from the uninjured right vocal fold. It is highly likely that the wounded VF had completely healed within the 42 days following the surgery without any significant tissue remodeling, which has been previously reported after 14 days post injury [44]. In this demonstration study, we have focused on exploring the normal rabbit vocal fold physiology in its native 3D form for the first time.

Future studies will be focused on quantitatively evaluating different injury models at earlier time points. We anticipate our novel approach to be of significant value in establishing vocal fold injury models as it would considerably aid in the localization of the wound site given its 3D capability. Previous studies have focused on 2D localization of vocal fold injuries with traditional histology that does not provide a complete picture of the 3D wound site and tissue remodeling. The application presented in this study uses commercially available technology in combination with inexpensive optical clearing, making it easily accessible to the medical research community.

In a comparison of both approaches as contrast methods for virtual histology of rabbit vocal folds, we were able to demonstrate that these techniques can be used in parallel to provide a complete picture of vocal fold histology. Nanotomography offers a convenient way of providing a coarse overview that can then be re-imaged at submicron resolution to obtain finer details of the relevant tissue ultrastructure. However, the density-based contrast mechanism in PTA labelled samples is an important limitation for the analysis of soft tissue as there is reduced contrast between cells in the vocal fold lamina propria and extracellular matrix components such as collagen and elastin. Nonlinear microscopy of cleared tissue can fill in these knowledge gaps as we were able to directly visualize collagen and elastin and resolve single cells at optical resolution in the same sample.

While nonlinear microscopy shows a wealth of detailed histological information, it presents limitations due to the optical point spread function of the laser scanning microscope, which is diffraction limited to around 1 μm axially in size in this study. This limits the resolution in XZ and YZ cross-sectional planes in rendering. However, this limitation could be addressed by the implementation of nonlinear tomography [45] which rotates the sample as it is imaged to exploit the increased lateral resolution in XY for an isometric pixel reconstruction. Despite this limitation, label free nonlinear microscopy allows virtual histological evaluation of tissue features that directly rival those offered by conventional histology. In addition, the uDISCO technique is directly compatible with fluorescent antibody labelling along with the use of fluorescent proteins from transgenic animals, allowing for highly specific labelling of proteins of interest in a three-dimensional environment.

3.5 Conclusion

In this work, we presented a new approach to rabbit vocal fold virtual histology using a complementary combination of nanotomography and nonlinear microscopy. Using these two techniques, detailed 3D volume renders of rabbit vocal folds were constructed for the first time, which highlighted relevant tissue features for the study of vocal fold regeneration. The ultrastructural information obtained was comparable to traditional histology for the study of connective tissue but does not require tissue sectioning. Using this novel combination of methods, a rabbit vocal fold wound model could then be studied in its native 3D state, and quantitative evaluation of experimental wound repair treatments could be conducted.

Funding

National Sciences and Engineering Research Council of Canada (NSERC) (RGPIN-2017-05005, RGPIN-2018-03843), Canada Research Chair (Tier 2 – Canadian Institutes of Health Research), Canada Foundation for Innovation (229251, 33122), National Institutes of Health (NIH) (NIH DC 005788-15)

Acknowledgments

We thank David L. Kolin (M.D., Ph.D.) for his helpful comments and suggestions on this manuscript. We acknowledge the Integrative Quantitative Biology Initiative (IQBI) of McGill University for access to the ZeIiss Xradia Versa 520. 3D rendering via Imaris for this work was performed in the McGill University Life Sciences Complex Advanced Biomaging Facility (ABIF).

Addendum:

The nonlinear microscopy volumes in figure 3-6 were reconstructed from 1024x1024 pixel images with a voxel size of 496 nm in XY and 50 μm in Z and a total acquisition time of approximately 5 hours. The volume in figure 3-8 is from 1024x1024 pixel images with a voxel size of 248 nm in

XY and 1 μm in Z and a total acquisition time of approximately 12 minutes. All stitched images were acquired with a 10% overlap.

3.6 References

1. Hirano, M., Morphological Structure of the Vocal Cord as a Vibrator and its Variations. *Folia Phoniatrica et Logopaedica* **1974,** *26* (2), 89-94.
2. Benninger, M. S.; Alessi, D.; Archer, S.; Bastian, R.; Ford, C.; Koufman, J.; Sataloff, R. T.; Spiegel, J. R.; Woo, P., Vocal fold scarring: current concepts and management. *Otolaryngol Head Neck Surg* **1996,** *115* (5), 474-82.
3. Krischke, S.; Weigelt, S.; Hoppe, U.; Kollner, V.; Klotz, M.; Eysholdt, U.; Rosanowski, F., Quality of life in dysphonic patients. *J Voice* **2005,** *19* (1), 132-7.
4. Friedrich, G.; Dikkers, F. G.; Arens, C.; Remacle, M.; Hess, M.; Giovanni, A.; Duflo, S.; Hantzakos, A.; Bachy, V.; Gugatschka, M.; European Laryngological Society. Phonosurgery, C., Vocal fold scars: current concepts and future directions. Consensus report of the Phonosurgery Committee of the European Laryngological Society. *Eur Arch Otorhinolaryngol* **2013,** *270* (9), 2491-507.
5. Mattei, A.; Magalon, J.; Bertrand, B.; Philandrianos, C.; Veran, J.; Giovanni, A., Cell therapy and vocal fold scarring. *Eur Ann Otorhinolaryngol Head Neck Dis* **2017,** *134* (5), 339-345.
6. Hirano, S., Current treatment of vocal fold scarring. *Curr Opin Otolaryngol Head Neck Surg* **2005,** *13* (3), 143-7.
7. Hansen, J. K.; Thibeault, S. L., Current understanding and review of the literature: vocal fold scarring. *J Voice* **2006,** *20* (1), 110-20.
8. Chen, W.; Woo, P.; Murry, T., Vocal Fold Vibration Following Surgical Intervention in Three Vocal Pathologies: A Preliminary Study. *J Voice* **2017,** *31* (5), 610-614.

9. Tracy, L. E.; Minasian, R. A.; Caterson, E. J., Extracellular Matrix and Dermal Fibroblast Function in the Healing Wound. *Adv Wound Care (New Rochelle)* **2016,** *5* (3), 119-136.

10. Rousseau, B.; Hirano, S.; Chan, R. W.; Welham, N. V.; Thibeault, S. L.; Ford, C. N.; Bless, D. M., Characterization of chronic vocal fold scarring in a rabbit model. *J Voice* **2004,** *18* (1), 116-24.

11. Titford, M., The long history of hematoxylin. *Biotech Histochem* **2005,** *80* (2), 73-8.

12. Lester, S. C., *Manual of Surgical Pathology E-Book*. Elsevier Health Sciences: 2010.

13. Suvarna, K. S.; Layton, C.; Bancroft, J. D., *Bancroft's Theory and Practice of Histological Techniques E-Book*. Elsevier Health Sciences: 2018.

14. Kishimoto, A. O.; Kishimoto, Y.; Young, D. L.; Zhang, J.; Rowland, I. J.; Welham, N. V., High- and ultrahigh-field magnetic resonance imaging of naive, injured and scarred vocal fold mucosae in rats. *Dis Model Mech* **2016,** *9* (11), 1397-1403.

15. Withers, P. J., X-ray nanotomography. *Materials Today* **2007,** *10* (12), 26-34.

16. Senter-Zapata, M.; Patel, K.; Bautista, P. A.; Griffin, M.; Michaelson, J.; Yagi, Y., The role of micro-CT in 3D histology imaging. *Pathobiology* **2016,** *83* (2-3), 140-147.

17. Bailly, L.; Cochereau, T.; Orgeas, L.; Henrich Bernardoni, N.; Rolland du Roscoat, S.; McLeer-Florin, A.; Robert, Y.; Laval, X.; Laurencin, T.; Chaffanjon, P.; Fayard, B.; Boller, E., 3D multiscale imaging of human vocal folds using synchrotron X-ray microtomography in phase retrieval mode. *Sci Rep* **2018,** *8* (1), 14003.

18. Zipfel, W. R.; Williams, R. M.; Webb, W. W., Nonlinear magic: multiphoton microscopy in the biosciences. *Nature Biotechnology* **2003,** *21*, 1369.

19. Zipfel, W. R.; Williams, R. M.; Christie, R.; Nikitin, A. Y.; Hyman, B. T.; Webb, W. W., Live tissue intrinsic emission microscopy using multiphoton-excited native fluorescence and

second harmonic generation. *Proceedings of the National Academy of Sciences* **2003,** *100* (12), 7075-7080.

20. Campagnola, P. J.; Loew, L. M., Second-harmonic imaging microscopy for visualizing biomolecular arrays in cells, tissues and organisms. *Nat Biotechnol* **2003,** *21* (11), 1356-60.

21. Campagnola, P. J.; Chen, X., SHG Microscopy and Its Comparison with THG, CARS, and Multiphoton Excited Fluorescence Imaging. In *Second Harmonic Generation Imaging*, CRC Press: 2016; pp 100-119.

22. Miri, A. K.; Tripathy, U.; Mongeau, L.; Wiseman, P. W., Nonlinear laser scanning microscopy of human vocal folds. *Laryngoscope* **2012,** *122* (2), 356-63.

23. Heris, H. K.; Miri, A. K.; Ghattamaneni, N. R.; Li, N. Y.; Thibeault, S. L.; Wiseman, P. W.; Mongeau, L., Microstructural and mechanical characterization of scarred vocal folds. *J Biomech* **2015,** *48* (4), 708-11.

24. Miri, A. K.; Heris, H. K.; Tripathy, U.; Wiseman, P. W.; Mongeau, L., Microstructural characterization of vocal folds toward a strain-energy model of collagen remodeling. *Acta Biomater* **2013,** *9* (8), 7957-67.

25. Heris, H. K.; Miri, A. K.; Tripathy, U.; Barthelat, F.; Mongeau, L., Indentation of poroviscoelastic vocal fold tissue using an atomic force microscope. *J Mech Behav Biomed Mater* **2013,** *28*, 383-92.

26. Kazarine, A.; Bouhabel, S.; Douillette, A. H.; Kost, K.; Li-Jessen, N. Y. K.; Mongeau, L.; Wiseman, P. W. In *Multimodal imaging of vocal fold scarring in a rabbit model by multiphoton microscopy*, SPIE BiOS, SPIE: 2017; p 9.

27. Theer, P.; Denk, W., On the fundamental imaging-depth limit in two-photon microscopy. *J Opt Soc Am A Opt Image Sci Vis* **2006,** *23* (12), 3139-49.

28. Ariel, P., A beginner's guide to tissue clearing. *Int J Biochem Cell Biol* **2017,** *84*, 35-39.

29. Richardson, D. S.; Lichtman, J. W., Clarifying Tissue Clearing. *Cell* **2015,** *162* (2), 246-257.

30. Tainaka, K.; Kubota, S. I.; Suyama, T. Q.; Susaki, E. A.; Perrin, D.; Ukai-Tadenuma, M.; Ukai, H.; Ueda, H. R., Whole-body imaging with single-cell resolution by tissue decolorization. *Cell* **2014,** *159* (4), 911-24.

31. Tomer, R.; Ye, L.; Hsueh, B.; Deisseroth, K., Advanced CLARITY for rapid and high-resolution imaging of intact tissues. *Nature Protocols* **2014,** *9*, 1682.

32. Pan, C.; Cai, R.; Quacquarelli, F. P.; Ghasemigharagoz, A.; Lourbopoulos, A.; Matryba, P.; Plesnila, N.; Dichgans, M.; Hellal, F.; Ertürk, A., Shrinkage-mediated imaging of entire organs and organisms using uDISCO. *Nature Methods* **2016,** *13*, 859.

33. Campagnolo, A. M.; Tsuji, D. H.; Sennes, L. U.; Imamura, R.; Saldiva, P. H., Histologic study of acute vocal fold wound healing after corticosteroid injection in a rabbit model. *Ann Otol Rhinol Laryngol* **2010,** *119* (2), 133-9.

34. Coppoolse, J. M.; Van Kooten, T. G.; Heris, H. K.; Mongeau, L.; Li, N. Y.; Thibeault, S. L.; Pitaro, J.; Akinpelu, O.; Daniel, S. J., An in vivo study of composite microgels based on hyaluronic acid and gelatin for the reconstruction of surgically injured rat vocal folds. *J Speech Lang Hear Res* **2014,** *57* (2), S658-73.

35. Metscher, B. D., MicroCT for developmental biology: a versatile tool for high-contrast 3D imaging at histological resolutions. *Dev Dyn* **2009,** *238* (3), 632-40.

36. Ban, M. J.; Park, J. H.; Kim, J. W.; Park, K. N.; Lee, J. Y.; Kim, H. K.; Lee, S. W., The Efficacy of Fibroblast Growth Factor for the Treatment of Chronic Vocal Fold Scarring: From Animal Model to Clinical Application. *Clin Exp Otorhinolaryngol* **2017,** *10* (4), 349-356.

37. Deniset-Besseau, A.; Duboisset, J.; Benichou, E.; Hache, F.; Brevet, P.-F.; Schanne-Klein, M.-C., Measurement of the Second-Order Hyperpolarizability of the Collagen Triple Helix

and Determination of Its Physical Origin. *The Journal of Physical Chemistry B* **2009,** *113* (40), 13437-13445.

38. Stoller, P.; Reiser, K. M.; Celliers, P. M.; Rubenchik, A. M., Polarization-Modulated Second Harmonic Generation in Collagen. *Biophysical Journal* **2002,** *82* (6), 3330-3342.

39. Chen, F.; Tillberg, P. W.; Boyden, E. S., Expansion microscopy. **2015,** *347* (6221), 543-548.

40. Mondal, P. P.; Diaspro, A., Lateral resolution improvement in two-photon excitation microscopy by aperture engineering. *Optics Communications* **2008,** *281* (7), 1855-1859.

41. Chen, B. C.; Legant, W. R.; Wang, K.; Shao, L.; Milkie, D. E.; Davidson, M. W.; Janetopoulos, C.; Wu, X. F. S.; Hammer, J. A.; Liu, Z.; English, B. P.; Mimori-Kiyosue, Y.; Romero, D. P.; Ritter, A. T.; Lippincott-Schwartz, J.; Fritz-Laylin, L.; Mullins, R. D.; Mitchell, D. M.; Bembenek, J. N.; Reymann, A. C.; Bohme, R.; Grill, S. W.; Wang, J. T.; Seydoux, G.; Tulu, U. S.; Kiehart, D. P.; Betzig, E., Lattice light-sheet microscopy: Imaging molecules to embryos at high spatiotemporal resolution. *Science* **2014,** *346* (6208), 439-+.

42. Fahrbach, F. O.; Gurchenkov, V.; Alessandri, K.; Nassoy, P.; Rohrbach, A., Light-sheet microscopy in thick media using scanned Bessel beams and two-photon fluorescence excitation. *Optics Express* **2013,** *21* (11), 13824.

43. Cella Zanacchi, F.; Lavagnino, Z.; Faretta, M.; Furia, L.; Diaspro, A., Light-Sheet Confined Super-Resolution Using Two-Photon Photoactivation. *PLoS ONE* **2013,** *8* (7), e67667.

44. Suehiro, A.; Bock, J. M.; Hall, J. E.; Garrett, C. G.; Rousseau, B., Feasibility and acute healing of vocal fold microflap incisions in a rabbit model. *The Laryngoscope* **2012,** *122* (3), 600-605.

45. Nolte, L.; Antonopoulos, G. C.; Rämisch, L.; Heisterkamp, A.; Ripken, T.; Meyer, H., Enabling second harmonic generation as a contrast mechanism for optical projection tomography (OPT) and scanning laser optical tomography (SLOT). *Biomed. Opt. Express* **2018,** *9* (6), 2627-2639.

Preface to Chapter 4

In the previous chapters, we demonstrated applications of nonlinear microscopy to hematology and virtual histology to present novel histological techniques. In Chapter 2, we utilized the enhanced THG resonance effect of hemoglobin and hemozoin to detect both red blood cells and malaria parasites within infected cells in the same channel. In Chapter 3 we implemented virtual histology by two photon fluorescence and second harmonic generation to visualize extracellular matrix components such as natively auto fluorescent elastin and collagen, respectively.

In this chapter, we explore the nonlinear optical properties of three common histological stains; Hematoxylin & Eosin, Verhoeff-Van-Gieson (VVG) and Sirius Red, on human skin and liver tissue sections. Using two photon fluorescence, we explore the native autofluorescence of unlabeled tissue and the resulting fluorescence from histologically stained tissue. We also employ second harmonic generation to highlight the collagen structure of the tissue samples. Finally, we identified two novel resonant THG harmonophores within VVG and Sirius Red stained tissue, that can be used to image elastic fibers, cell nuclei and collagen by THG with high specificity and contrast.

This chapter has been published as an article in *Analyst* (Kazarine et al. 2019).

4 Nonlinear Microscopy of Common Histological Stains Reveals THG Harmonophores

Alexei Kazarine †[a], Angelica A. Gopal †[a,b], Paul W. Wiseman*[a,c]

[a]Department of Chemistry, McGill University, 801 Sherbrooke St. West, Montreal, QC, H3A 0B8, Canada

[b]Department of Physiology, McGill University, 3655 Promenade Sir William Osler, Montreal, QC, H3G 1Y6, Canada

[c]Department of Physics, McGill University, 3600 University St., Montreal, QC, H3A 2T8, Canada

†These authors contributed equally to this work.

4.1 Abstract

Since its invention over a hundred years ago, histological analysis using coloured dye staining remains the gold standard for histopathology. While these stains provide critical information for a variety of diagnostic purposes, they offer limited two-dimensional histological information. Extending classical histological analysis to three dimensions requires novel imaging approaches such as multiphoton microscopy. Multiphoton microscopy enables multimodal, three-dimensional imaging of histologically stained samples. Specifically, third harmonic generation (THG), a nonlinear optical process in which three incident photons are combined into one by the sample, allows high contrast imaging of tissues stained with absorbing dyes, which in turn act as harmonophores. While this technique has previously been applied to hematoxylin and eosin (H&E) tissue sections, we extend this approach to other commonly used histological stains to demonstrate further potential applications of the technique. We demonstrate THG imaging of both human skin and liver tissue stained with H&E, Verhoeff-Van Gieson (VVG) and Picrosirius Red stains. We find that these stains provide excellent contrast as THG harmonophores, enabling high resolution imaging of histological samples. THG imaging of the Verhoeff stain enables easy

detection of elastic fibers while Picrosirius Red acts as an effective harmonophore for imaging collagen fibers of all sizes.

4.2 Introduction

Medical diagnostics have relied on histological staining for the last century thanks to its ability to easily contrast different tissue elements using brightly coloured stains.[1] The most popular tool in histopathology is the hematoxylin (H) and eosin (E) stain, most commonly referred to as H&E.[2] Hematoxylin is a dye extracted from the logwood tree. Its oxidized form, hematin, is combined with an aluminium salt to form haemalum, a complex that has a high affinity for chromatin in nuclei.[3] Its application in histology results in cell nuclei being stained a deep purple colour. Eosin Y, a fluorescent dye, is used to provide contrast by counterstaining basic amino acids, resulting in extracellular matrix elements, connective tissue and cytoplasm being stained a light pink colour.[4] In combination, H&E's ability to differentiate between cells and extracellular tissue elements has made it into the gold standard of histopathological analysis.

Other histological stains provide contrast for different tissue elements. For example, the Verhoeff stain effectively highlights elastic fibers in addition to nuclei by colouring them black.[5] Its counterstain, the Van Gieson stain, is used to differentiate collagen fibers in red and other tissue elements in yellow.[6] Together, these techniques form the Verhoeff-Van- Gieson (VVG) stain, an effective technique for identifying elastic tissue disorders, particularly in dermatology.[7]

Another useful method for revealing extracellular collagen is the Picrosirius Red stain, a combination of Sirius Red, a poly-azobenzene dye, with an aqueous saturated picric acid solution. This technique highlights collagen in bright red, with other tissue elements being stained in yellow.[8] While similar to the Van Gieson stain, Picrosirius Red serves as an important alternative

due to its improved stability and its ability to enhance the birefringence of collagen, improving its specificity when combined with polarization microscopy.[9] In this fashion, Picrosirius Red has been used for quantitative histological determination of collagen in various tissues.[10]

Histological investigations are usually performed with basic white light microscopy. However, the tissues under examination need to be thinly sectioned to avoid out-of-focus blur, providing only a limited two-dimensional snapshot of the tissue. As tissues exist in a three-dimensional (3D) structure, histologists are required to subjectively determine which projections to take during sectioning to ensure representative sampling. 3D reconstruction must either be done mentally during visualization of the slices or computationally after laborious imaging of consecutive sections. Pathological examinations could benefit from 3D histological information,[11] with improved spatial resolution and better image contrast than that provided by light microscopy.

Nonlinear microscopy[12–16] is a technique that is fast gaining notoriety in the world of biological imaging thanks to its multimodal nature and ability to conduct deep 3D imaging. It utilizes ultrafast lasers to induce multiple photon-matter interactions, that results in the visualization of multiphoton fluorescence and other nonlinear optical contrast mechanisms such as second harmonic generation (SHG) and third harmonic generation (THG).[17] SHG is the generation of emitted light at exactly twice the frequency of excitation light in a nonlinear optical material.18 In tissue, this intrinsic nonlinear property arises in dense non-centrosymmetric structures such as collagen fibers and muscle.[19] THG, a phenomenon in which three excitation photons are combined into a single photon presenting three times the incident frequency, occurs from optical heterogeneities within the sample.[20] THG has been used to visualize many intrinsic interfaces in tissue, including lipid/water interfaces such as myelin,[21] cell membranes[22] and other lipid bodies.[23]

Nonlinear microscopy has become an essential technique to conduct label-free histology via SHG and THG.[24–26]

However, using labels for nonlinear contrast mechanisms such as THG is becoming a topic of interest as it allows for increased specificity while retaining the inherent three-dimensional imaging capability. Materials that exhibit high second and/or third order nonlinear susceptibilities have been called harmonophores.[27] These harmonophores exploit resonant effects during the multiphoton interaction process to significantly enhance emission while maintaining low incident power. Several intrinsic THG harmonophores have been discovered, including hemoglobin[28] and hemozoin.[29–31] In addition, hematoxylin has been found to present significant THG susceptibility, likely due to resonance effects thanks to its nature as an absorptive dye.[32–34]

In this study, we performed trans nonlinear imaging of unlabelled and histologically stained human skin and liver tissue sections, and demonstrated that in addition to H&E, other histological dyes used in elastic and collagen staining also have the ability to induce strong THG signals in stained tissues. For the first time, we have observed that tissue components stained by VVG and Sirius Red act as THG harmonophores. Elastic fibres and cell nuclei exhibit a strong THG signal upon VVG staining, while Van Gieson labelled collagen exhibits two photon fluorescence (TPF). Collagen stained with Picrosirius Red demonstrates strong third order nonlinear susceptibility through its intense THG signal at low excitation power.

4.3 Methods

4.3.1 Nonlinear Microscopy

Nonlinear microscopy of the histological samples was achieved using a customized upright multiphoton microscope (FV1200 MPE, Olympus Canada Inc., ON, Canada) as shown in Figure

4-1. The system is equipped with two ultrafast laser excitation sources that provide ~200 fs pulses: a Ti:sapphire laser (Mira 900F, Coherent, CA, USA) tuned for excitation at 780 nm and an optical parametric oscillator (Mira OPO, Coherent, CA, USA) configured for excitation at 1150 nm. Switching between the two sources is accomplished through two motorized flip mirror mounts (MFF101, Thorlabs, NJ, USA). Laser excitation power is controlled by a custom computerized variable attenuator composed of a half wave rhomb retarder (FR600HM, Thorlabs, NJ, USA) mounted in a motorized rotational stage (PRM1Z8, Thorlabs, NJ, USA) combined with a Glan-Laser polarizer (GL10, Thorlabs, NJ USA). Excitation laser power is measured immediately prior to beam entrance to the microscope using a thermal power sensor and console (S175C/ PM100D, Thorlabs, NJ, USA). The polarization of the excitation beam is selected after power control using an achromatic quarter waveplate (AQWP10M-980, Thorlabs, NJ, USA) mounted on a rotational cage mount (CRM1, Thorlabs, NJ, USA). A 25× 1.05 NA water immersion multiphoton objective (XLPL25XWMP, Olympus Canada Inc., Ontario, Canada) focuses the excitation light on the histological tissue samples. The light emitted in the forward direction is collected with a 0.9 NA dry top lens condenser and directed towards two photomultiplier (PMT) detectors after splitting by a dichroic mirror. A 770 nm short pass infrared-blocking filter (FF01-770/SP32, Semrock, New York, USA) is used to block scattered excitation light.

THG imaging was conducted using the OPO (1150 nm, 15–55 mW) for excitation and a 400 nm filter (380–420 nm filter, ET400/40X, Chroma Technology, Vermont, USA) for detection. SHG and TPF imaging was achieved by excitation with the Ti:sapphire laser (780 nm, 8–35 mW). SHG was collected using the same filter as THG, while TPF was collected using three channels: "blue" (460–500 nm filter, BA460-500, Olympus Canada Inc., Ontario, Canada), "green" (515–555 nm filter, BA515-555, Olympus Canada Inc., Ontario, Canada) and "red" (570–630 nm filter, ET600-60, Chroma

Technology, Vermont, USA). SHG was collected at the same time as the "red" TPF channel, while "blue" and "green" were collected together. Two dichroic mirrors (TP550LPXR and TP505LPXR, Chroma Technology, Vermont, USA) were used to separate the channels within each set. Brightfield images were acquired on the same imaging setup using a color CMOS camera (DCC1645C, Thorlabs, New Jersey, USA).

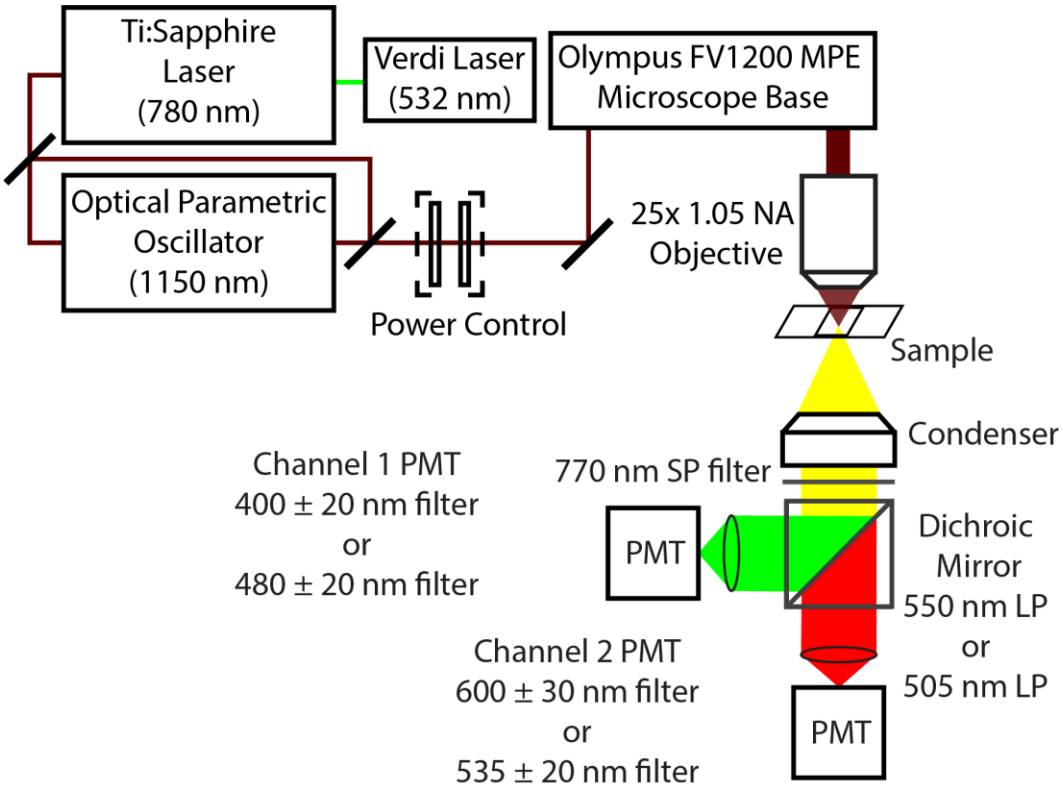

Figure 4-1: Experimental nonlinear microscopy imaging setup. Abbreviations: PMT, photomultiplier tube; SP, short pass; LP, long pass. Briefly, the Verdi laser pumps the Ti:sapphire laser, which can either be used directly for imaging or directed to an optical parametric oscillator to achieve higher excitation wavelengths. Both laser outputs are directed into a power and polarization control module prior to entry to the microscope base.

4.3.2 Tissues and Histological Staining

Human skin (TTR003-25EA) and liver (TTR012-25EA) control tissue sections were obtained from MilliporeSigma, ON, Canada along with all histological reagents unless otherwise specified. Each set of tissue sections was first deparaffinized using passages in xylene. H&E staining was

performed using Harris hematoxylin solution (HHS16) and alcoholic eosin Y solution (HT110116) in accordance with the "HHS" Sigma- Aldrich procedure. VVG staining was achieved using the HT25A elastic stain kit in accordance with the "HT25" Sigma- Aldrich procedure. Picrosirius Red staining solution was performed using a Sirius Red (3655548) solution in saturated picric acid (P6744). Each stain was performed on separate, sequential sections of each tissue type.

4.4 Results and Discussion

4.4.1 Nonlinear Microscopy of Unlabelled Tissue Highlights Collagen *via* SHG

We first performed nonlinear microscopy of unlabelled tissue sections to evaluate the features observable through native two photon autofluorescence, SHG and THG. We first excited the unlabelled skin and liver samples with 780 nm illumination to visualize TPF and SHG (Figure 4-2).

Figure 4-2A and B displays blue TPF exhibited by skin tissue sections where Figure 4-2A shows part of the epidermis and the underlying dermis and Figure 4-2B displays the reticular dermis, mostly composed of type I collagen and elastic fibers. The autofluorescence exhibited in this channel seems to be largely nonspecific with the exception of elastic fibers, which are composed of intrinsically auto-fluorescent elastin.17 Figure 4-2C and D displays blue TPF of liver tissue sections, specifically connective tissue associated with portal areas within the liver. Figure 4-2E–H highlights the green TPF while Figure 4-2I–L represents the red TPF emitted by the skin and liver tissue sections. Elastin is emphasized more prominently in the green TPF of the skin sections (Figure 4-2E and F) while red blood cells are readily observable in the green and red TPF of liver sections (Figure 4-2K and L).

SHG imaging of both tissue types (Figure 4-2M–P) efficiently highlights fibrillar collagen within the skin dermis and connective tissue of the liver portal areas. It has been shown previously that SHG is a vital tool of label-free nonlinear microscopy, due to its high specificity for non-centrosymmetric materials with high second order nonlinear susceptibility such as collagen and to a lesser extent muscle.[35–38] In our study, we use the SHG channel as the control channel, to track readily observable fibrillar collagen structures within the skin dermis samples and the liver connective tissue samples.

The samples were then excited with 1150 nm illumination to observe THG, highlighting the presence of optical heterogeneities within the tissues (Figure 4-2Q–T). Most prominently, THG reveals the stratified squamous keratinized epithelium (keratinocytes) in skin samples (Figure 4-2Q), in addition to red blood cells in the liver tissue sections, visible thanks to their highly resonant hemoglobin content[28,39] (Figure 4-2T). Elastic fibers (Figure 4-2R) also provide a slightly above background THG signal (Figure 4-2R).[40] While THG is useful for unlabelled imaging of lipids, interfaces, and highly resonant harmonophores, its capabilities in label-free histological investigations are restricted due to low specificity outside of resonant harmonophores.

Overall, while nonlinear microscopy of unlabelled tissue sections readily visualizes collagen and native tissue autofluorescence though SHG and TPF respectively, it does not provide sufficient specificity and contrast for full histological investigations. It also appears that native tissue autofluorescence can be seen across all three of the TPF channels that were imaged, providing no additional information. As such, we will not be including the blue TPF channel in subsequent figures.

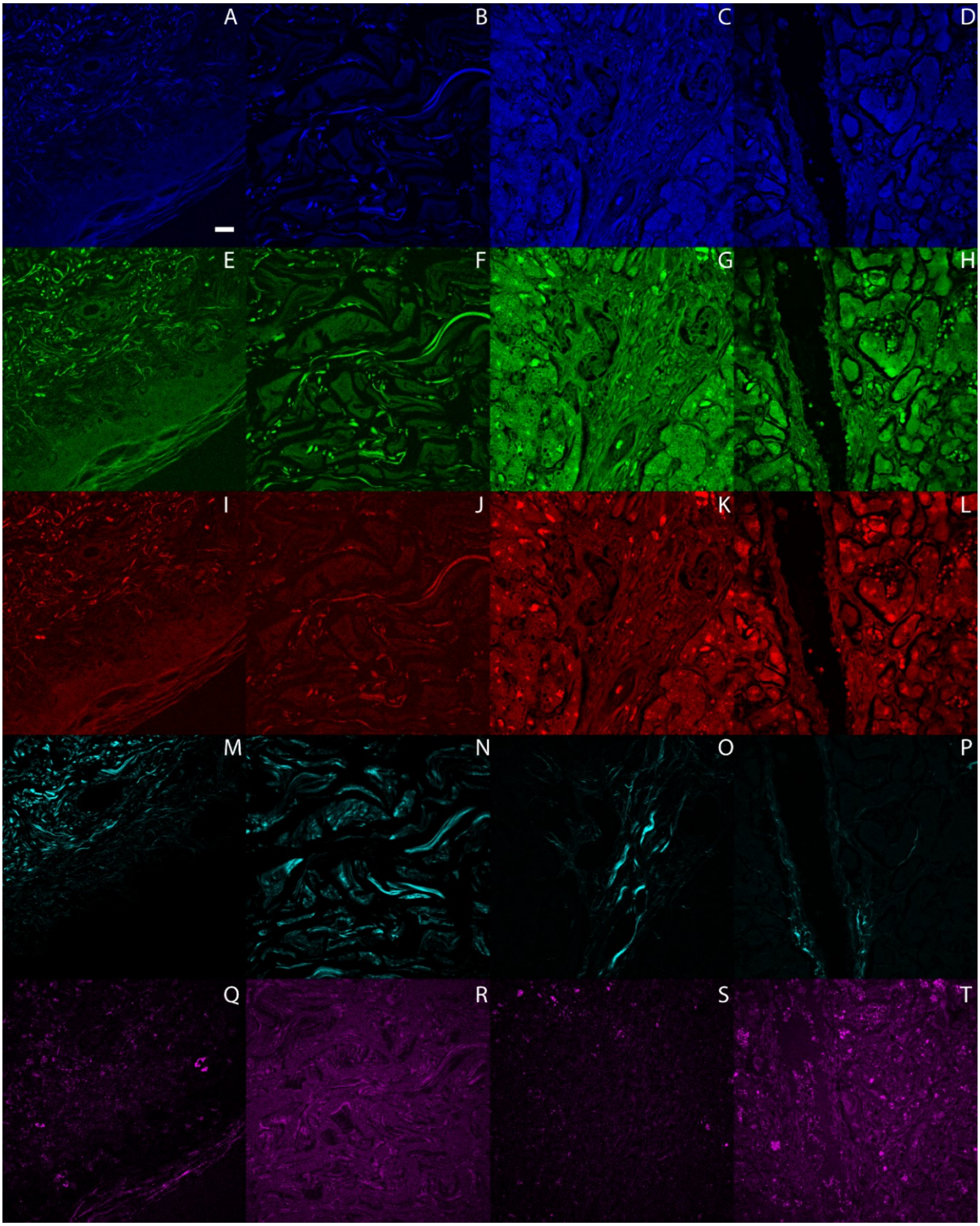

Figure 4-2: Nonlinear microscopy of unlabeled skin and liver tissue sections. First and second columns: skin; third and fourth columns: liver. A–D: Blue TPF; E–H: green TPF; I–L: red TPF; M–P: SHG; Q–T: THG. A–P are excited by 780 nm while Q–T were excited by 1150 nm. Global scale bar in A is 10 μm.

4.4.2 H&E Stained Tissue Sections Visualized by Nonlinear Microscopy Reveals High Contrast Nuclear Imaging via THG

The first histological stain that was investigated is H&E, the most widely used stain in histopathology. Two skin samples and two liver samples were stained and imaged first with white light microscopy (Figure 4-3A–D). The H component resulted in cell nuclei in both tissue types being stained a deep purple while other tissue elements including collagen and cellular cytoplasm were dyed pink by the E component. Figure 4-3A shows part of a hair follicle, while Figure 4-3B displays sweat glands, both structures located in the reticular dermis in skin samples. Figure 4-3C demonstrates part of a liver lobule with red blood cells (stained red-pink, no nuclei) and hepatocytes (nuclei in purple). Figure 4-3D showcases a portal area including hepatocytes and Kupfer cells (nuclei in dark purple/black).

TPF imaging of these H&E stained samples can be found in Figure 4-3E–H (green TPF) and Figure 4-3I–L (red TPF). The features displayed in these channels are those most stained with eosin Y, a highly fluorescent dye that binds to basic amine acid residues. 41 Cell cytoplasm (top) and collagen fibers (bottom) are visible in Figure 4-3E. Figure 4-3F displays staining extracellular tissue elements, most notably collagen (later verified by SHG) and elastin. In the liver, hepatocyte cytoplasm is readily visualized in addition to red blood cells within the sinusoids (Figure 4-3G). Figure 4-3H again demonstrates cytoplasm and extracellular matrix staining. The aforementioned features are similarly displayed in the red TPF channel (Figure 4-3I–L).

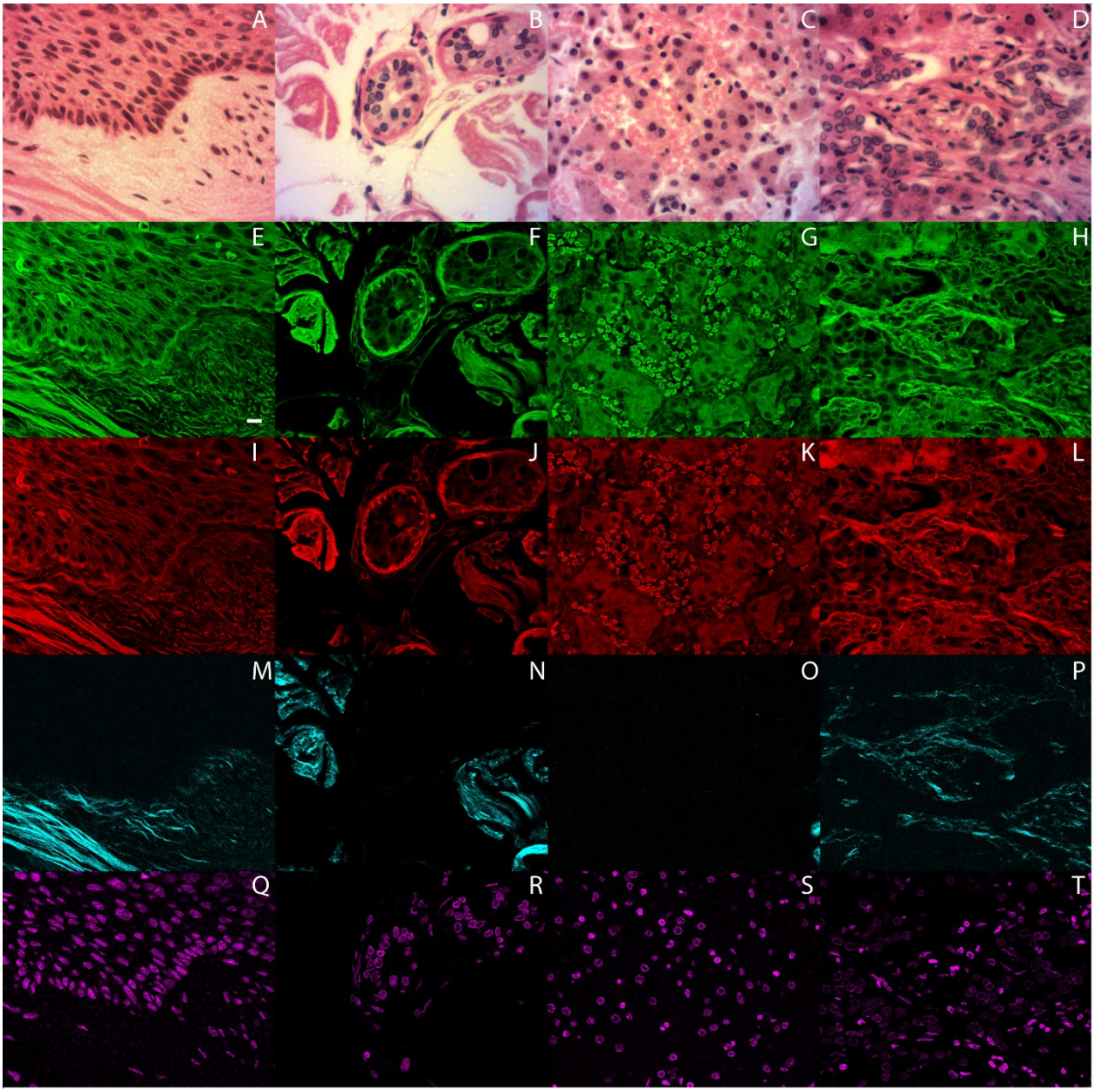

Figure 4-3: Nonlinear microscopy of H&E stained skin and liver tissue sections. First and second columns: skin; third and fourth columns: liver. A–D: White light microscopy; E–H: green TPF; I–L: red TPF; M–P: SHG; Q–T: THG. E–P are excited by 780 nm while Q–T were excited by 1150 nm. Global scale bar in E is 10 µm.

Figure 4-3M–P illustrates SHG imaging of the H&E stained tissue sections where the SHG signal is readily attributed to the presence of fibrillar collagen and not enhanced by the H&E staining.

On the other hand, THG imaging (Figure 4-3Q–T) exhibits clear contrast of cellular nuclei stained by hematoxylin. It has been previously shown that hematoxylin presents strong resonance enhancement of THG as the virtual transition states of the THG process when excited at 1230 nm correspond to real electronic energy states of the molecule.[33] Specifically, hematoxylin possesses absorbance bands at two and three times the fundamental excitation frequency (second and third virtual states). As we excited our H&E samples at 1150 nm, these correspond to 575 nm and 383 nm, respectively, which are included in the absorbance spectrum of hematoxylin. [34] It has previously been shown that aggregation of hemalum complexes within cell nuclei significantly increases THG emission.[33]

To verify the power dependency of the SHG and THG channels, we collected SHG/THG emission at different incident laser powers. As can be seen in Figure 4-4, the SHG signal grows with a second order dependence ($x^{1.95}$) while THG follows a third order power dependence ($x^{3.02}$) verifying that the THG channel is indeed capturing THG emission.

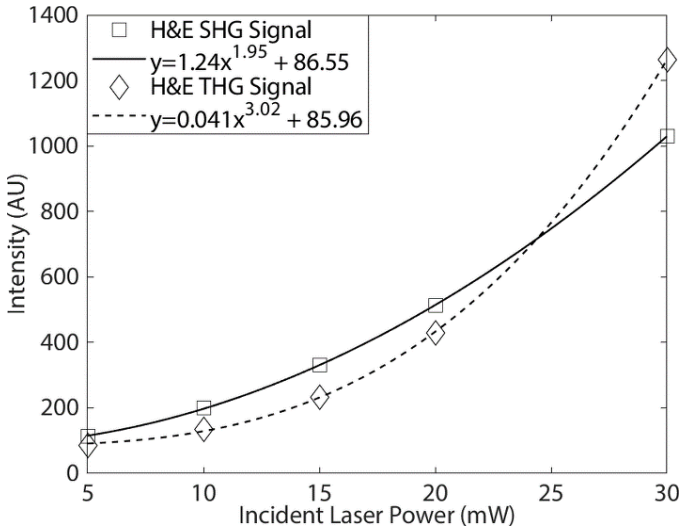

Figure 4-4: Power curve of H&E stained tissue samples showing the second order dependency of SHG emission and third order dependency of THG emission.

4.4.3 Nonlinear Microscopy of Verhoeff-Van-Gieson (VVG) Stained Tissue Sections Highlights Elastic Fibers and Cell Nuclei by THG

Next, we investigated the nonlinear properties of VVG stained skin and liver tissue sections. We first visualized the stained tissue sections with white light microscopy (Figure 4-5A–D). The Verhoeff component of the stain colours both elastic fibers and cell nuclei in black. The Van Gieson component, composed of picric acid and acid fuchsin, provides a pink counterstain to collagen and other extracellular components. Figure 4-5A presents the epidermal layer of a skin section, whereas Figure 4-5B demonstrates a sweat gland in the reticular dermis. Figure 4-5C and D shows interlobular connective tissue within the liver sections containing elastic fibers stained in black.

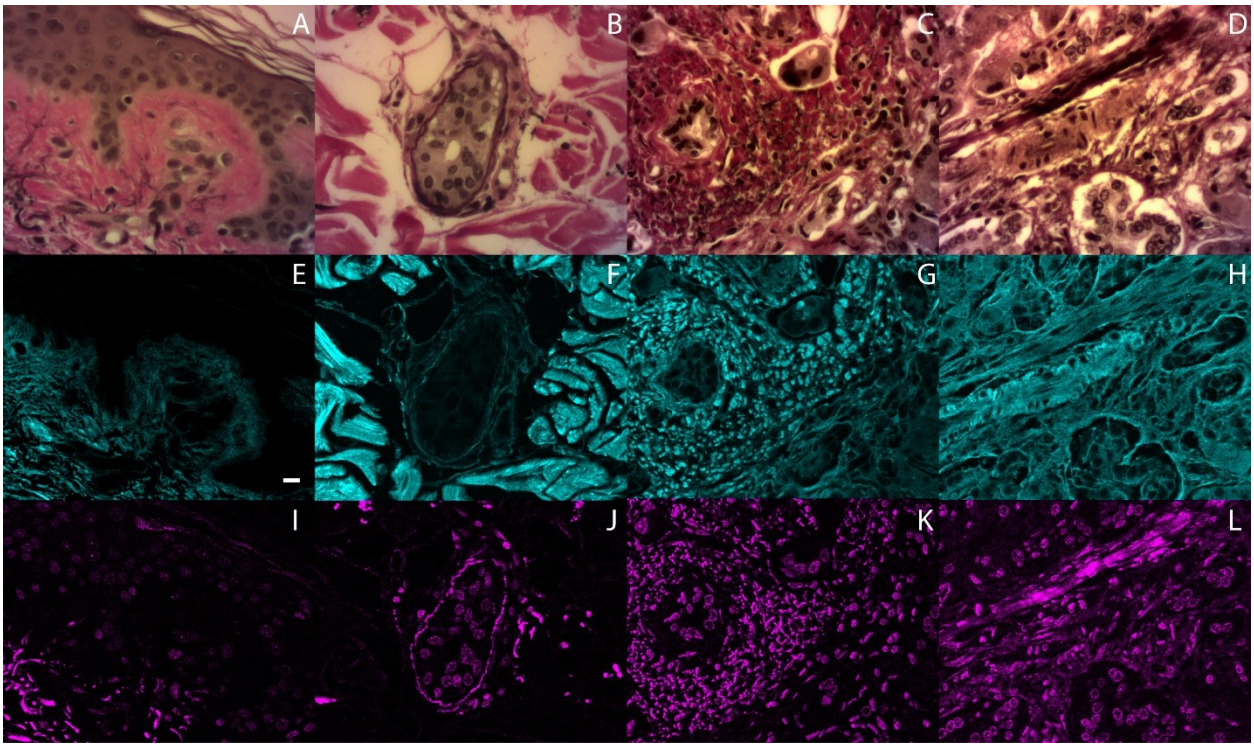

Figure 4-5: Nonlinear microscopy of VVG stained skin and liver tissue sections. First and second columns: skin; third and fourth columns: liver. A–D: White light microscopy; E–H: SHG + red TPF (570–630 nm); I–L: THG; E–L are excited by 1150 nm. Global scale bar in E is 10 μm.

During initial experiments, significant photobleaching and damage was observed when tissue sections were illuminated at 780 nm at low power (15 mW). Therefore, we limited our excitation to 1150 nm illumination for our examinations of VVG. Figure 4-5E–H shows emission in the range of 570–630 nm, which covers both SHG and red TPF emission within the same channel. The features exhibited within skin tissue sections show a combination of SHG signal from fibrillar collagen fibers previously shown in H&E and unlabelled tissue samples along with fluorescence from the acid fuchsin (pink) stained tissue elements. This includes all forms of collagen and other extracellular matrix elements. In addition, we expect some contribution from native tissue autofluorescence in red TPF. Acid fuchsin is known to act as a fluorophore when excited at 543 nm, which is within the two photon excitation range at 1150 nm.[42]

Figure 4-5I–L demonstrates THG imaging of VVG stained tissue sections where we observe significant emission from Verhoeff stained tissue components in both skin and liver tissue. Specifically, we readily observe cell nuclei (Figure 4-5I and J) and stained elastic fibers (Figure 4-5J–L). As the Verhoeff stain primarily consists of a iron hematoxylin complex,[5] which binds readily to elastic fibers, it is apparent that the binding of these complexes to elastic tissue displays significant third order nonlinear susceptibility, enabling us to visualize them by THG. The resonance enhancement process likely proceeds similarly to the hematoxylin component of H&E staining, where real energy levels within the molecule coincide with the second and third virtual transition states of the THG process.

To verify if the emission in the 380–420 nm channel is due to THG, we conducted a power dependency study (Figure 4-6), where we observed a third order dependency ($x^{3.01}$) associated with the VVG-THG signal. To the best of our knowledge, this is the first application of VVG as a THG harmonophore for high contrast elastic fiber and nuclei imaging.

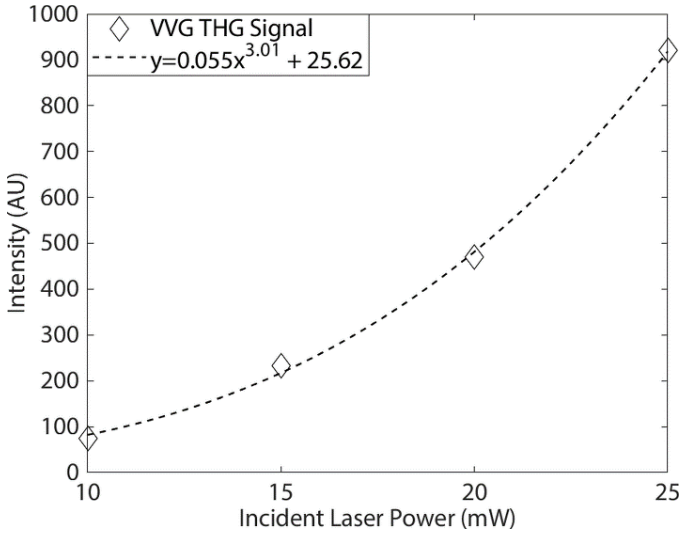

Figure 4-6: Power curve of VVG stained tissue samples showing the third order dependency of THG emission.

4.4.4 Picrosirius Red Acts as a Highly Selective Collagen Specific THG Harmonophore

Picrosirius Red is a stain regularly used for histological analysis of collagen content in tissue.[43] The stain consists of Sirius Red, an azo dye also known as direct red 80. The dye is mixed with a saturated solution of picric acid prior to application, which enhances the intensity of the stain. Collagen within tissue stained with Picrosirius Red appears as bright red against a yellow background. During staining, the elongated, anionic structure of the Sirius Red dye molecule binds to cationic collagen fibers, also enhancing the natural birefringence of collagen.[8]

In our next experiment, we stained skin and liver tissue sections with Picrosirius Red and first examined them with white light microscopy. Figure 4-7A and B demonstrates the staining of skin tissue samples where Figure 4-7A shows a section of the epidermis and underlying dermis while Figure 4-7B highlights a blood vessel within the dermis. Figure 4-7C and D shows staining of connective tissue within liver sections where Figure 4-7C presents part of a portal triad.

We then performed nonlinear microscopy using 780 nm excitation to evaluate TPF and SHG of the tissue sections. Figure 4-7E–H displays green TPF of skin and liver tissue sections, respectively. The green TPF signal imaged seems to be largely due to nonspecific autofluorescence within the tissues as previously seen in the unlabelled tissue sections (Figure 4-2E–H). However, the red TPF of the tissue sections most prominently show the Picrosirius Red staining, highlighting areas of collagen that were stained bright red in the dermis (Figure 4-7I and J), around a blood vessel in the skin (Figure 4-7J), and in the connective tissue of the liver (Figure 4-7K and L). It has been shown that Picrosirius Red staining observed in fluorescent imaging displays a highly specific and sensitive, red fluorescent signal for the evaluation of collagen in tissue sections.[44] In addition to the highly specific collagen signal, we observe weak nonspecific autofluorescence similar to that seen in the green TPF channel.

Figure 4-7M–P displays the SHG signal from the 780 nm excitation where we observe fibrillar collagen within the skin and liver sections. The areas highlighted by SHG seem to correspond well to the features observed in the red TPF (Figure 4-7I–L). Most notably, the contrast obtained by SHG appears to be more selective of larger collagen fibers (Figure 4-7N) whereas the Sirius Red TPF highlights a larger number of fibers, including smaller bundles of collagen (Figure 4-7J). This is likely due to the size dependent nature of SHG signal from collagen fibers. As such, when

detection sensitivity is adjusted below signal saturation, only the larger fibers can be visualized due to their strong signal and weaker signals from smaller fibers may not be visualized. This effect does not occur for Sirius Red stained collagen since the fluorescence is equally attributed to all collagen fiber sizes.

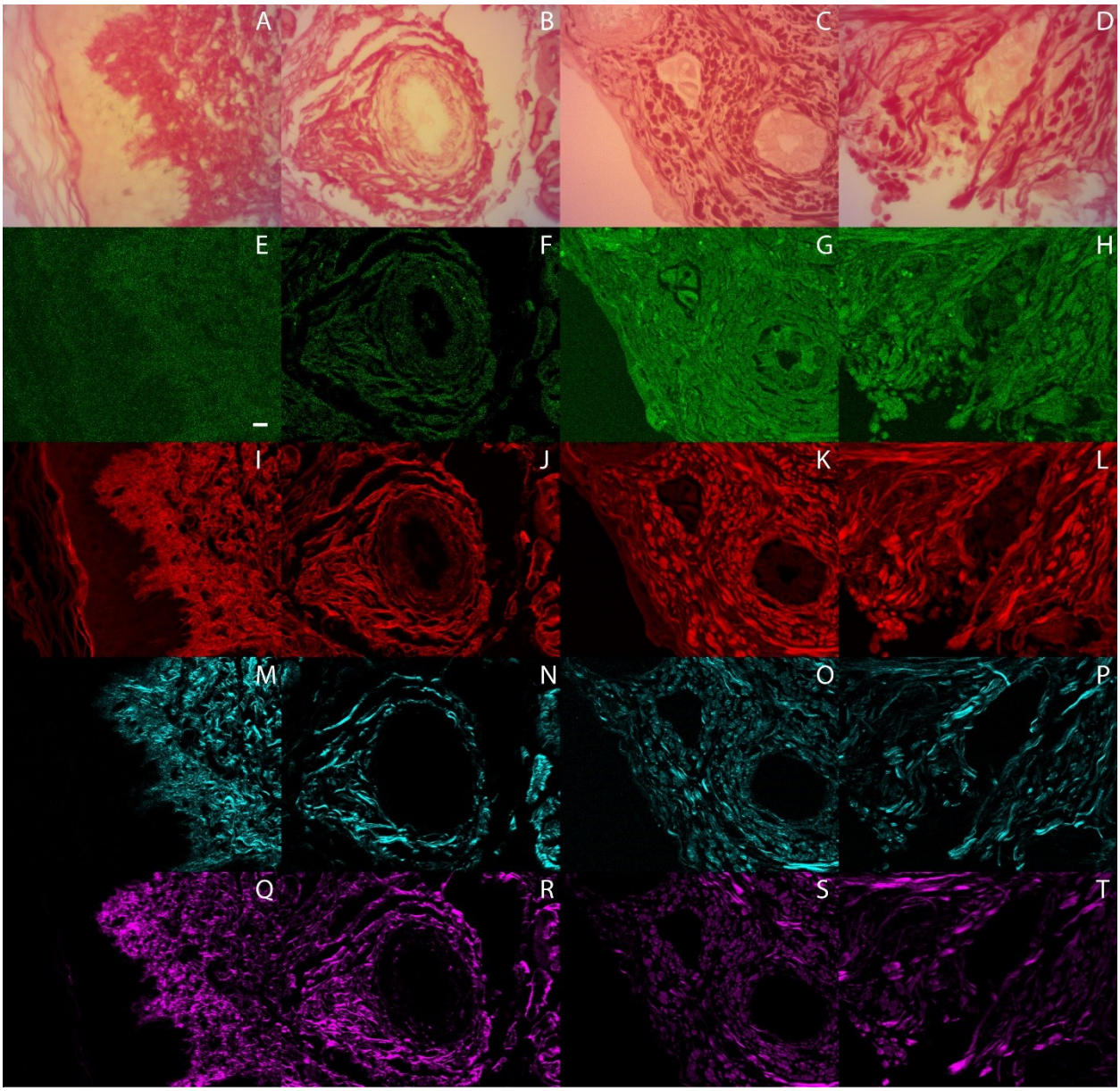

Figure 4-7: Nonlinear microscopy of Picrosirius Red stained skin and liver tissue sections. First and second columns: skin; third and fourth columns: liver. A–D: White light microscopy; E–H: green TPF; I–L: red TPF; M–P: SHG; Q–T: THG. E–P are excited by 780 nm while Q–T were excited by 1150 nm. Global scale bar in E is 10 µm.

Finally, we excited the Sirius Red stained tissue sections with 1150 nm to collect THG images (Figure 4-7Q–T). Unlike the unlabeled tissue sections in Figure 4-2Q–T, where we only observed weak THG signal at 45 mW excitation, Sirius Red staining provided significant THG emission up to PMT saturation at a third of the power (15 mW). The features exhibiting THG emission overlap with the collagen detected by SHG while demonstrating a larger number of fibers similar to the red TPF. As such, it appears that the collagen stained with Picrosirius Red exhibits a high third order nonlinear susceptibility to be visualized by THG. In comparison to the features seen by red TPF, THG provides increased contrast of the collagen against a significantly lower background due to the specificity needed for THG emission. We did not observe any autofluorescence in the THG channel in comparison to the red TPF. To validate the origin of the contrast mechanisms detected within the SHG and THG channels, we performed a power dependency study (Figure 4-8). The SHG signal held a quadratic power dependency ($x^{1.93}$) while the THG signal showed a cubic power dependency ($x^{2.95}$). To the best of our knowledge, this is the first application of Picrosirius Red as a THG harmonophore for collagen detection.

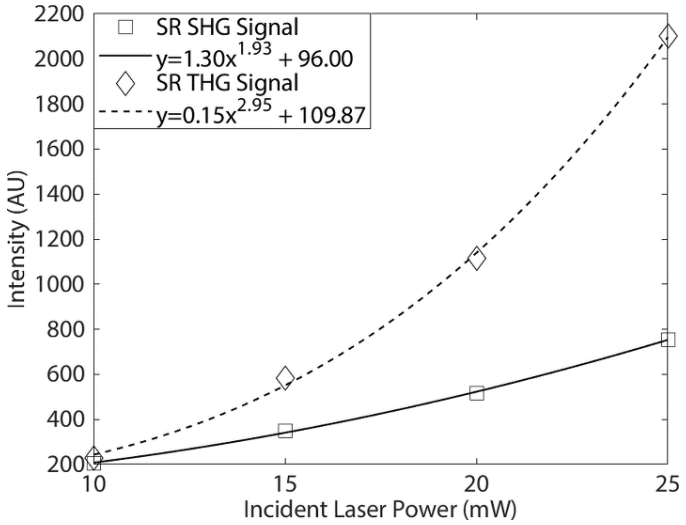

Figure 4-8: Power curve of Picrosirius Red stained tissue samples showing the second order dependency of SHG emission and third order dependency of THG emission.

In comparison to the traditional SHG-based detection of collagen, THG of Picrosirius Red provides greater detail across all fiber sizes, higher signal and is less sensitive to fiber orientation within the tissue. SHG emission is highly dependent on the fiber orientation in regards to the laser polarization.[45] In addition, SHG is not sensitive to fibers that are oriented parallel to the laser propagation direction.[46] In contrast, THG emitted by a harmonophore such as Sirius Red is not subject to these limitations.

The origin of the significant third order nonlinear susceptibility displayed by Sirius Red is not yet known. Azobenzene dyes, such as Disperse Red 1, have been shown to exhibit third order nonlinear susceptibility, which has been attributed to the trans–cis transition within the dye molecule.[47,48] Sirius Red is a poly-azo dye, suggesting that it could benefit from the same mechanisms as other azobenzene dyes for nonlinear susceptibility. Additionally, resonance through electronic nonlinearity could enhance this effect. It can be suggested that there is overlap between the virtual states invoked by THG and the real electronic energy levels of Sirius Red. Specifically, the molecule presents an absorbance peak at 528–529 nm with significant absorbance until 560 nm (ref. 49) as well as a smaller shoulder around 372 nm. This could result in overlap with the second (575 nm) and third (383 nm) virtual states involved with 1150 nm excitation, leading to a resonance enhancement of THG emission. An additional factor for the nonlinear susceptibility of Sirius Red could be due to the enhanced birefringence of collagen by the dye molecule. It has been shown that THG can occur in the bulk of birefringent materials thanks to enhanced phase matching conditions.[50] By using circular polarization excitation along with a polarization analyzer at the detector, THG could be used to evaluate the birefringence of materials.[51]

As THG requires ultrafast laser excitation, that can be used to simultaneously investigate multiple modalities, it is important to consider the thermal impact of multiphoton excitation on the sample. Commonly, this would require the use of nanothermal indicators,[52] such as quantum dots, with spectral detection capabilities, to properly evaluate the thermal impact at the 3D focal volume. In mouse brain tissue, it has been estimated that two photon microscopy produces around 1.8 °C increase per 100 mW excitation.[53] As our method utilizes excitation powers ranging from 8 mW to 55 mW, we expect the thermal impact to be minor provided there is no linear absorbance of the excitation wavelength in the tissue.

THG imaging presents improved resolution over white light microscopy thanks to its use of a tightly focused laser beam and the cubic dependence of its point spread function on excitation light intensity.[14] The resolution of THG imaging could be significantly improved through the use of image scanning microscopy (ISM) schemes where the point detector is replaced with an array of photodetectors.[54] This enables computational pixel reassignment that can enhance spatial resolution. ISM has previously been demonstrated for two photon microscopy and second harmonic generation imaging.[55,56]

To increase the specificity of THG harmonophore based histology beyond the selectivity offered by traditional histological dyes, targeted attachment of harmonophores through different labelling modalities could be explored. Cellular organelles have been specifically labelled with gold nanoparticles that act as plasmon-resonant harmonophores for THG.[57] In addition, lipid-enclosed quantum dots functionalized with antibodies have been used to detect cellular receptors in breast cancer cells via THG imaging.[58] Most recently, carotenoid- based labels that act as THG harmonophores have been used to label specific cell structures.[59]

The use of THG to visualize harmonophores in common histological dyes brings several potential advantages to medical diagnostics. THG imaging enables better contrast than white light microscopy, along with the inherent possibility for 3D imaging. In addition, visualizing histological features such as cell nuclei and collagen reorganization in separate detection channels enables easier quantification by cell counting and area segmentation. A THG based approach could be automated for direct objective evaluation of histological features.

4.5 Conclusion

In this work, we identified two new applications of common histological dyes as third harmonic generation harmonophores for specific and high contrast imaging: Verhoeff Van Gieson and Sirius Red. The techniques were demonstrated using human skin and liver tissue sections and characterized by multimodal nonlinear microscopy, specifically two photon fluorescence, second harmonic generation and third harmonic generation imaging. We verified hematoxylin as a THG harmonophore for high contrast nuclear staining in accordance to previous studies. We distinguished that the iron hematoxylin of the Verhoeff stain acts as a strong THG harmonophore in tissue, where it binds to elastic fibers and cell nuclei. We also demonstrated that Sirius Red presents significant third order nonlinear susceptibility upon binding to collagen in tissue samples, allowing for enhanced resonance and highly specific high contrast collagen detection by THG.

The utilisation of THG imaging to visualize common histological dyes presents great potential for three-dimensional histological imaging at low cost due to the extremely low power requirements for resonant THG imaging. Other histological dyes could be examined as potential THG harmonophores through electronic resonance enhancement, rendering them potentially powerful tools for the future of three dimensional histology.

Acknowledgements

The authors gratefully acknowledge Discovery Grant support from the Natural Sciences and Engineering Research Council of Canada for P. W. W. (RGPIN-2017-05005). The authors would like to thank the Canada Foundation for Innovation for infrastructure support (229251).

4.6 References

1. G. Musumeci, *J. Histol. Histopathol.*, 2014, **1**(1), 5.
2. M. Titford, *Biotech. Histochem.*, 2005, **80**, 73–78.
3. B. D. Llewellyn, *Biotech. Histochem.*, 2009, **84**, 159–177.
4. A. H. Fischer, K. A. Jacobson, J. Rose and R. Zeller, *CSH Protocols*, 2008, DOI: 10.1101/pdb.prot4986.
5. F. H. Verhoeff, *J. Am. Med. Assoc.*, 1908, **L**, 876–877.
6. J. Van Gieson, *N. Y. Med. J.*, 1889, **50**, 57–60.
7. V. Kazlouskaya, S. Malhotra, J. Lambe, M. H. Idriss, D. Elston and C. Andres, *J. Cutaneous Pathol.*, 2013, **40**, 211–225.
8. L. C. Junqueira, G. Bignolas and R. R. Brentani, *Histochem. J.*, 1979, **11**, 447–455.
9. L. F. Nielsen, D. Moe, S. Kirkeby and C. Garbarsch, *Biotech. Histochem.*, 1998, **73**, 71–77.
10. P. Whittaker, R. A. Kloner, D. R. Boughner and J. G. Pickering, *Basic Res. Cardiol.*, 1994, **89**, 397–410.
11. L. Teodori, A. Crupi, A. Costa, A. Diaspro, S. Melzer and Tarnok, *J. Biophotonics*, 2017, **10**, 24–45.
12. R. Carriles, D. N. Schafer, K. E. Sheetz, J. J. Field, R. Cisek, V. Barzda, A. W. Sylvester and J. A. Squier, *Rev. Sci. Instrum.*, 2009, **80**, 081101.
13. K. W. Dunn and P. A. Young, *Nephron Exp. Nephrol.*, 2006, **103**, e33–e40.

14. J. Squier and M. Muller, *Rev. Sci. Instrum.*, 2001, **72**, 2855– 2867.

15. R. M. Williams, W. R. Zipfel and W. W. Webb, *Curr. Opin. Chem. Biol.*, 2001, **5**, 603–608.

16. W. R. Zipfel, R. M. Williams and W. W. Webb, *Nat. Biotechnol.*, 2003, **21**, 1369–1377.

17. W. R. Zipfel, R. M. Williams, R. Christie, A. Y. Nikitin, T. Hyman and W. W. Webb, *Proc. Natl. Acad. Sci. U. S. A.*, 2003, **100**, 7075–7080.

18. P. Bianchini and A. Diaspro, *J. Biophotonics*, 2008, **1**, 443– 450.

19. P. J. Campagnola, A. C. Millard, M. Terasaki, P. E. Hoppe, J.Malone and W. A. Mohler, *Biophys. J.*, 2002, **82**, 493–508.

20. B. Weigelin, G. J. Bakker and P. Friedl, *J. Cell Sci.*, 2016, **129**, 245–255.

21. M. J. Farrar, F. W. Wise, J. R. Fetcho and C. B. Schaffer, *Biophys. J.*, 2011, **100**, 1362–1371.

22. N. Olivier, M. A. Luengo-Oroz, L. Duloquin, E. Faure, T. Savy, I. Veilleux, X. Solinas, D. Debarre, P. Bourgine, A. Santos, N. Peyrieras and E. Beaurepaire, *Science*, 2010, **329**, 967–971.

23. D. Debarre, W. Supatto, A. M. Pena, A. Fabre, T. Tordjmann, L. Combettes, M. C. Schanne-Klein and E. Beaurepaire, *Nat. Methods*, 2006, **3**, 47–53.

24. A. M. Streets, A. Li, T. Chen and Y. Huang, *Anal. Chem.*, 2014, **86**, 8506–8513.

25. H. Tu, Y. Liu, D. Turchinovich, M. Marjanovic, J. Lyngso, J. Laegsgaard, E. J. Chaney, Y. Zhao, S. You, W. L. Wilson, B. Xu, M. Dantus and S. A. Boppart, *Nat. Photonics*, 2016, **10**, 534–540.

26. S. You, Y. Sun, E. J. Chaney, Y. Zhao, J. Chen, S. A. Boppart and H. Tu, *Biomed. Opt. Express*, 2018, **9**, 5240–5252.

27. D. Tokarz, R. Cisek, N. Prent, U. Fekl and V. Barzda, *Anal. Chim. Acta*, 2012, **755**, 86–92.

28. G. O. Clay, A. C. Millard, C. B. Schaffer, J. Aus-Der-Au, P. S. Tsai, J. A. Squier and D. Kleinfeld, *J. Opt. Soc. Am. B*, 2006, **23**, 932–950.

29. A. Kazarine, F. Baakdah, A. A. Gopal, W. Oyibo, E. Georges and P. W. Wiseman, *Anal. Chem.*, 2019, **91**, 2216–2223.

30. U. Tripathy, M. Giguere-Bisson, M. H. Sangji, M. J. Bellemare, D. S. Bohle, E. Georges and P. W. Wiseman, *Anal. Bioanal. Chem.*, 2013, **405**, 5431–5440.

31. J. M. Belisle, S. Costantino, M. L. Leimanis, M. J. Bellemare, D. S. Bohle, E. Georges and P. W. Wiseman, *Biophys. J.*, 2008, **94**, L26–L28.

32. A. Tuer, L. Bakueva, R. Cisek, J. Alami, D. J. Dumont, J. Rowlands and V. Barzda, Enhancement of third harmonic contrast with harmonophores in multimodal nonlinear microscopy of histological sections, *Proc. SPIE 6860, Multiphoton Microscopy in the Biomedical Sciences VIII*, 2008, 686005, DOI: 10.1117/12.763509.

33. A. Tuer, D. Tokarz, N. Prent, R. Cisek, J. Alami, D. J. Dumont, L. Bakueva, J. Rowlands and V. Barzda, *J. Biomed. Opt.*, 2010, **15**, 026018.

34. C. H. Yu, S. P. Tai, C. T. Kung, W. J. Lee, Y. F. Chan, H. L. Liu, J. Y. Lyu and C. K. Sun, *Opt. Lett.*, 2008, **33**, 387–389.

35. E. Brown, T. McKee, E. diTomaso, A. Pluen, B. Seed, Y. Boucher and R. K. Jain, *Nat. Med.*, 2003, **9**, 796–800.

36. R. M. Kottmann, J. Sharp, K. Owens, P. Salzman, G. Q. Xiao, R. P. Phipps, P. J. Sime, E. B. Brown and S. W. Perry, *Respir. Res.*, 2015, **16**, 61.

37. M. Yildirim, K. P. Quinn, J. B. Kobler, S. M. Zeitels, Georgakoudi and A. Ben-Yakar, *Scanning*, 2016, **38**, 684–693.

38. T. Boulesteix, E. Beaurepaire, M. P. Sauviat and M. C. Schanne-Klein, *Opt. Lett.*, 2004, **29**, 2031–2033.

39. I. Saytashev, R. Glenn, G. A. Murashova, S. Osseiran, D. Spence, C. L. Evans and M. Dantus, *Biomed. Opt. Express*, 2016, **7**, 3449–3460.

40. C. H. Yu, S. P. Tai, C. T. Kung, I. J. Wang, H. C. Yu, H. J. Huang, W. J. Lee, Y. F. Chan and C. K. Sun, *Opt. Express*, 2007, **15**, 11167–11177.

41. R. W. Horobin and J. A. Kiernan, *Conn's biological stains: a handbook of dyes, stains and fluorochromes for use in biology and medicine*, BIOS Scientific Publishers, 2002.

42. Z. Burdikova, M. Capek, P. Ostasov, J. Machac, R. Pelc, E. A. Mitchell and L. Kubinova, *Microsc. Microanal.*, 2010, **16**, 735–746.

43. C. Segnani, C. Ippolito, L. Antonioli, C. Pellegrini, C. Blandizzi, A. Dolfi and N. Bernardini, *PLoS One*, 2015, **10**, e0144630.

44. K. A. Wegner, A. Keikhosravi, K. W. Eliceiri and C. M. Vezina, *J. Histochem. Cytochem.*, 2017, **65**, 479–490.

45. P. Stoller, K. M. Reiser, P. M. Celliers and A. M. Rubenchik, *Biophys. J.*, 2002, **82**, 3330–3342.

46. B. Wen, K. R. Campbell, B. L. Cox, K. W. Eliceiri, R. Superfine and P. J. Campagnola, *Opt. Lett.*, 2015, **40**, 3201–3204.

47. R. Rangel-Rojo, S. Yamada, H. Matsuda and D. Yankelevich, *Appl. Phys. Lett.*, 1998, **72**, 1021–1023.

48. L. Brzozowski and E. H. Sargent, *J. Mater. Sci.: Mater. Electron.*, 2001, **12**, 483–489.

49. R. W. Dapson, C. Fagan, J. A. Kiernan and T. W. Wickersham, *Biotech. Histochem.*, 2011, **86**, 133–139.

50. D. Oron, E. Tal and Y. Silberberg, *Opt. Lett.*, 2003, **28**, 2315–2317.

51. D. Oron, D. Yelin, E. Tal, S. Raz, R. Fachima and Y. Silberberg, *J. Struct. Biol.*, 2004, **147**, 3–11.

52. M. Quintanilla and L. M. Liz-Marzán, *Nano Today*, 2018, **19**, 126–145.

53. K. Podgorski and G. Ranganathan, *J. Neurophysiol.*, 2016, **116**, 1012–1023.

54. C. B. Muller and J. Enderlein, *Phys. Rev. Lett.*, 2010, **104**, 198101.

55. I. Gregor, M. Spiecker, R. Petrovsky, J. Grosshans, R. Ros and J. Enderlein, *Nat. Methods*, 2017, **14**, 1087–1089.

56. C. J. R. Sheppard, M. Castello, G. Tortarolo, G. Vicidomini and A. Diaspro, *J. Opt. Soc. Am. A*, 2017, **34**, 1339–1350.

57. D. Yelin, D. Oron, S. Thiberge, E. Moses and Y. Silberberg, *Opt. Express*, 2003, **11**(12), 1385–1391.

58. C.-F. Chang, C.-Y. Chen, F.-H. Chang, S.-P. Tai, C.-Y. Chen, C.-H. Yu, Y.-B. Tseng, T.-H. Tsai, I. S. Liu, W.-F. Su and C.-K. Sun, *Opt. Express*, 2008, **16**(13), 9534–9548.

59. D. Tokarz, R. Cisek, M. Garbaczewska, D. Sandkuijl, X. Qiu, B. Stewart, J. D. Levine, U. Fekl and V. Barzda, *Phys. Chem. Chem. Phys.*, 2012, **14**, 10653–10661.

5 Conclusions

The study of tissue using microscopy and histological staining has been widely implemented in biomedical fields since its introduction over a century ago to conduct pathological investigations. To this day, conventional histological analysis remains a critical tool in biomedical research and medical diagnostics. Despite technological advances in other areas of biophotonics, histological staining remains as the gold standard for histopathological examination. Significant research is being conducted to modernize the practice of histology by extending tissue evaluation to the third dimension to improve accuracy and increase throughput.

The work described in this thesis implements novel techniques based on nonlinear microscopy to answer biomedical questions in hematology, tissue engineering and histology. We tackled challenges in malaria detection, virtual histology of vocal folds and uncovered new harmonophores from existing histological staining protocols for use in nonlinear imaging. We hope that these techniques, which present effective alternatives to conventional histological methods, advance the future of histopathology.

Chapter 2 presented a novel malaria detection method based on automated blood smear analysis by third harmonic generation image scanning cytometry (THGISC). It was previously shown that hemozoin, a digestive byproduct of the malaria parasite during its blood lifecycle, exhibited extremely intense and specific third harmonic generation (THG) signal. The strong nonlinear susceptibility of hemozoin was attributed to electronic resonance effects where real energy electronic states existing within the molecule coincide with the energy levels of the virtual states of the nonlinear THG process. Using this molecular property, we developed a new approach to automated malaria detection where we can detect both single red blood cells and hemozoin from

malaria parasites within a single channel in a label-free manner. In contrast to traditional malaria detection, which relies on manual observation by a trained and experienced microscopist, our method utilizes automated image segmentation and cell counting to quickly determine the level of parasitemia in thin blood smears.

We have demonstrated this technique using lab-grown parasites at different lifecycle stages in addition to whole blood patient samples collected in field clinics in Nigeria. The ability to rapidly measure parasitemia by THGISC could potentially allow easy confirmation of diagnosis following symptoms in addition to permitting the tracking of treatment progress in diagnosed patients, which could allow personalized medication and dosage adjustments. However, the main limitation of our technique is the prerequisite for an ultrafast mode-locked excitation laser, carrying a significant initial expense. A more economical option would be to use a single wavelength fiber laser instead of the tunable OPO that was used in our demonstration. With the rapid progress in laser oscillator development/optimization, we hope that ultrafast laser sources will become more widely accessible and available. Due to the cost and power requirements of the laser, this technique is more suitable to hospitals and clinics, where a straightforward higher throughput method would be useful for patient evaluations throughout treatment, permitting earlier health care interventions.

In Chapter 3, a new multimodal approach to vocal fold histology is introduced through a combination of label-free nonlinear microscopy and nano computed tomography. Human vocal folds present a unique anatomical structure that enables speech. This fragile structure, composed of primarily of extracellular matrix components, is prone to scarring as a result of disease, injury, overuse or surgery. Vocal fold scarring can significantly decrease quality of life through inhibiting

proper phonation during speech. The regeneration of vocal fold tissue after injury poses a significant tissue engineering challenge due to the complex microarchitecture of the tissue.

To provide a three-dimensional (3D) histological solution, we combined nonlinear microscopy with nano computed tomography to visualize rabbit vocal folds. We constructed detailed 3D volume renders of whole vocal folds, highlighting the collagen and elastin microstructure of the vocal fold lamina propria in addition to the surrounding muscle, cartilage and blood vessels. The ultrastructural information obtained with this technique is comparable to traditional histology for evaluating connective tissue without requiring mechanical tissue sectioning. Using this approach, a rabbit vocal fold wound model could be established for quantitative evaluation of tissue regeneration therapies.

Chapter 4 investigates common histological dyes using nonlinear microscopy to evaluate their potential use as nonlinear labels i.e. harmonophores. Harmonophores are molecules that exhibit significant nonlinear susceptibility enabling them to emit high intensity signals during harmonic generation. Hemozoin, a molecule explored in Chapter is an excellent example of a harmonophore that enables its effective use in malaria detection. The utilization of harmonophores in THG imaging is of great interest due to their high selectivity and strong signals that can be effectively combined with the innate three-dimensional optical sectioning capabilities of nonlinear imaging.

Hematoxylin, part of the hematoxylin and eosin (H&E) stain, was previously found to act as an efficient THG harmonophore for nuclear staining. We verified this capability using human skin and liver tissue sections and compared it to unlabeled tissue sections. We then identified two novel THG harmonophores within other conventional histological dyes. Iron hematoxylin in the Verhoeff-Van-Gieson (VVG) stain was found to exhibit significant THG signal upon illumination

with 1150 nm excitation. This complex selectively labels elastic fibers and cell nuclei in tissue and is suspected to possess a similar nonlinear resonance property as shown by the haemalum complex obtained after H&E staining. Sirirus Red, a poly-azo dye used as part of the picrosirius red stain, was also found to be an excellent THG harmonophore that can be used to selectively label collagen fibers of all sizes. To our knowledge, this was the first time that the VVG and picrosirius red stains were identified as THG harmonophores.

In conclusion, this thesis demonstrates several novel histological techniques that exploit the numerous advantages of nonlinear microscopy to solve such biomedical problems as automated malaria diagnosis, virtual histology and the identification of highly selective labels for THG imaging in tissue sections. We developed two new biomedical imaging approaches using nonlinear microscopy and revealed new THG harmonophores within common and inexpensive histological stains.

Future work should focus on the advancement of these techniques to reach their full potential. THGISC could be extended to a flow cytometry approach through advancements in high speed line scanning. As THG is an interface effect that requires the sample being imaged to be on the same scale as the laser beam for maximum sensitivity, the traditional flow cytometry configuration of widefield illumination would be impractical. Therefore, continuous line scanning to capture all incoming RBCs would be required, with potential improvements through the application of Bessel beam illumination. For more economically viable options, implementation of this technique with cheaper single wavelength fiber laser sources should also be further explored.

Virtual histology through nonlinear microscopy could be improved through the utilization of mid-infrared sources to excite three photon fluorescence instead of two photon fluorescence for

deeper imaging and better signal. Currently, we have utilized the two-photon fluorescence approach in combination with optical tissue clearing to reach millimeter depths in tissues. In contrast, using three photon technology with adaptive optics, one could potential image up to an order of magnitude deeper with the final limitation being the working distance of the objective. Our current virtual histology approach is presently being used to quantitatively evaluate wound healing in rabbit vocal folds at various stages of the healing process.

Finally, the use of THG harmonophores found in common histological dyes could be easily expanded to the third dimension. This would enable highly selective staining of histological features of interest with a high signal to noise readout by THG. Implementing this approach in thicker tissue samples could enable 3D virtual histology by THG at low cost. Other histological dyes sharing common molecular characteristics as the ones investigated should be evaluated as potential THG harmonophores.

The expansion and application of nonlinear microscopy techniques has significantly advanced since the development of the first multiphoton microscope nearly 30 years ago. The results presented in this thesis demonstrate the powerful capabilities of nonlinear microscopy to conduct multimodal histological examinations in three dimensions and will hopefully guide future technological advancements and applications in biomedical research.

6 Appendix A

Supporting Information:

Malaria Detection by Third Harmonic Generation Image Scanning Cytometry

Alexei Kazarine,† Fadi Baakdah,‡ Angelica A. Gopal,† Wellington Oyibo,§ Elias Georges,‡

and Paul W. Wiseman*,†,‖

†Department of Chemistry, McGill University, 801 Sherbrooke Street West, Montreal, Quebec H3A 0B8, Canada

‡Institute of Parasitology, McGill University, Sainte Anne de Bellevue, Quebec H9X 3 V9, Canada

§ANDI Centre of Excellence for Malaria Diagnosis, College of Medicine, University of Lagos, Idi-Araba, Lagos 100254, Nigeria

‖Department of Physics, McGill University, 3600 University Street, Montreal, Quebec H3A 2T8, Canada

Figure A-1: MATLAB application for red blood cell counting and hemozoin detection by THGISC image analysis.

Figure A-2: Validation of method performance using acridine orange nuclear staining on cultured *P. falciparum* parasites.

Figure A-3: Validation of method performance using DAPI nuclear staining on cultured *P. falciparum* parasites.

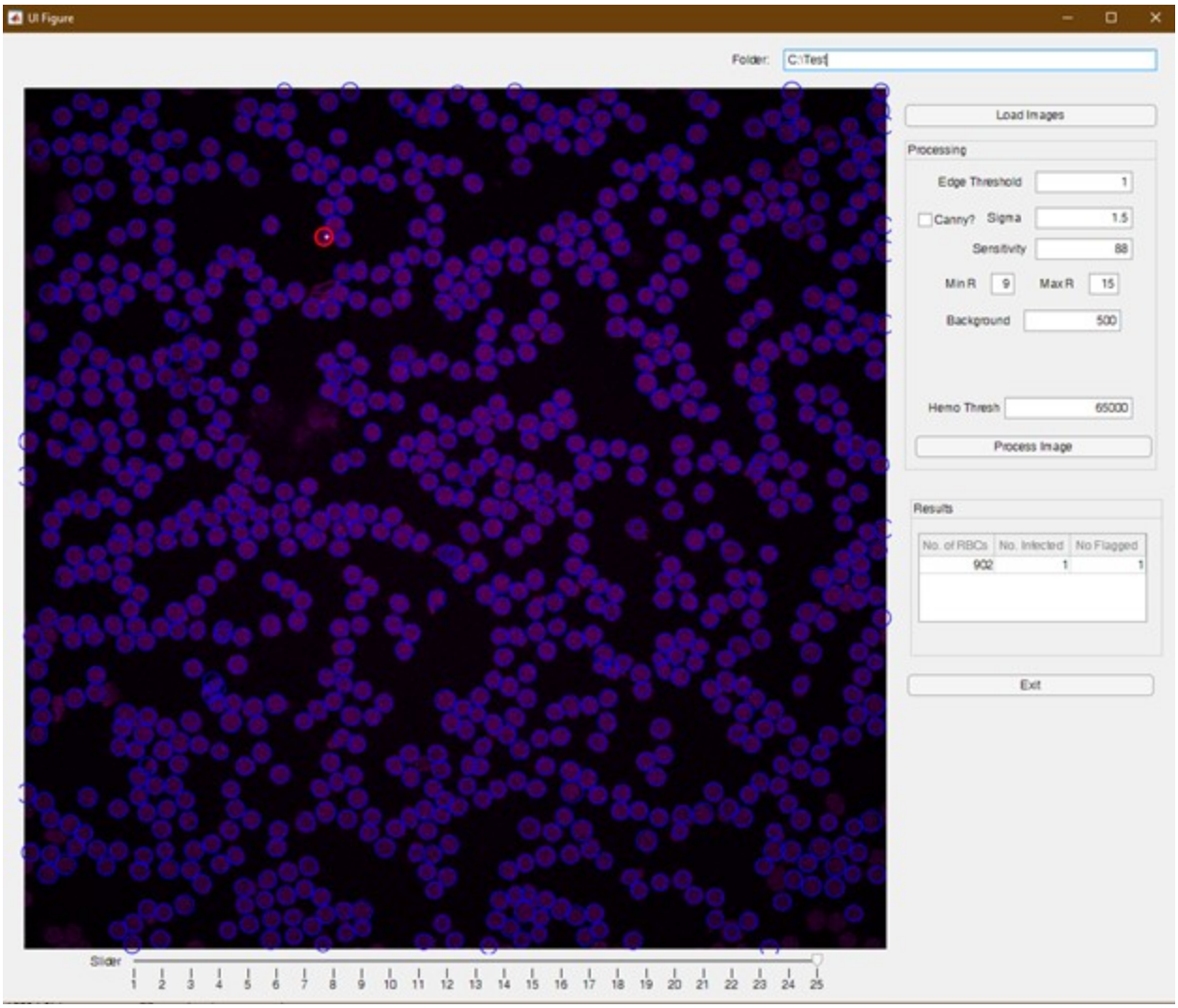

Figure A-1: MATLAB application for red blood cell counting and hemozoin detection by THGISC image analysis. This application allows images to be loaded in bulk. After the user selects an image using the bottom slider, the RBC counting via circular Hough transform (*imfindcircles* function in MATLAB) is conducted at the same time as hemozoin detection via an intensity threshold after clicking on the "Process image" button. The RBC counting can be made more or less sensitive using the **Edge Threshold** (circle detection), **Sigma** (of the gaussian filter) and **Sensitivity** (circle detection) parameters. The circle size can be specified using the **Min R** and **Max R** parameters. The hemozoin detection threshold can be set using the **Hemo Thresh** parameter (in counts). The **Background** parameter sets a background level above which cells should be detected. The Canny edge detection algorithm can be applied in pre-processing to assist with circle detection using the **Canny?** checkbox. The program output results in a table that specified the number of RBCs detected, the number of infected RBCs found, and the total number of objects flagged as hemozoin.

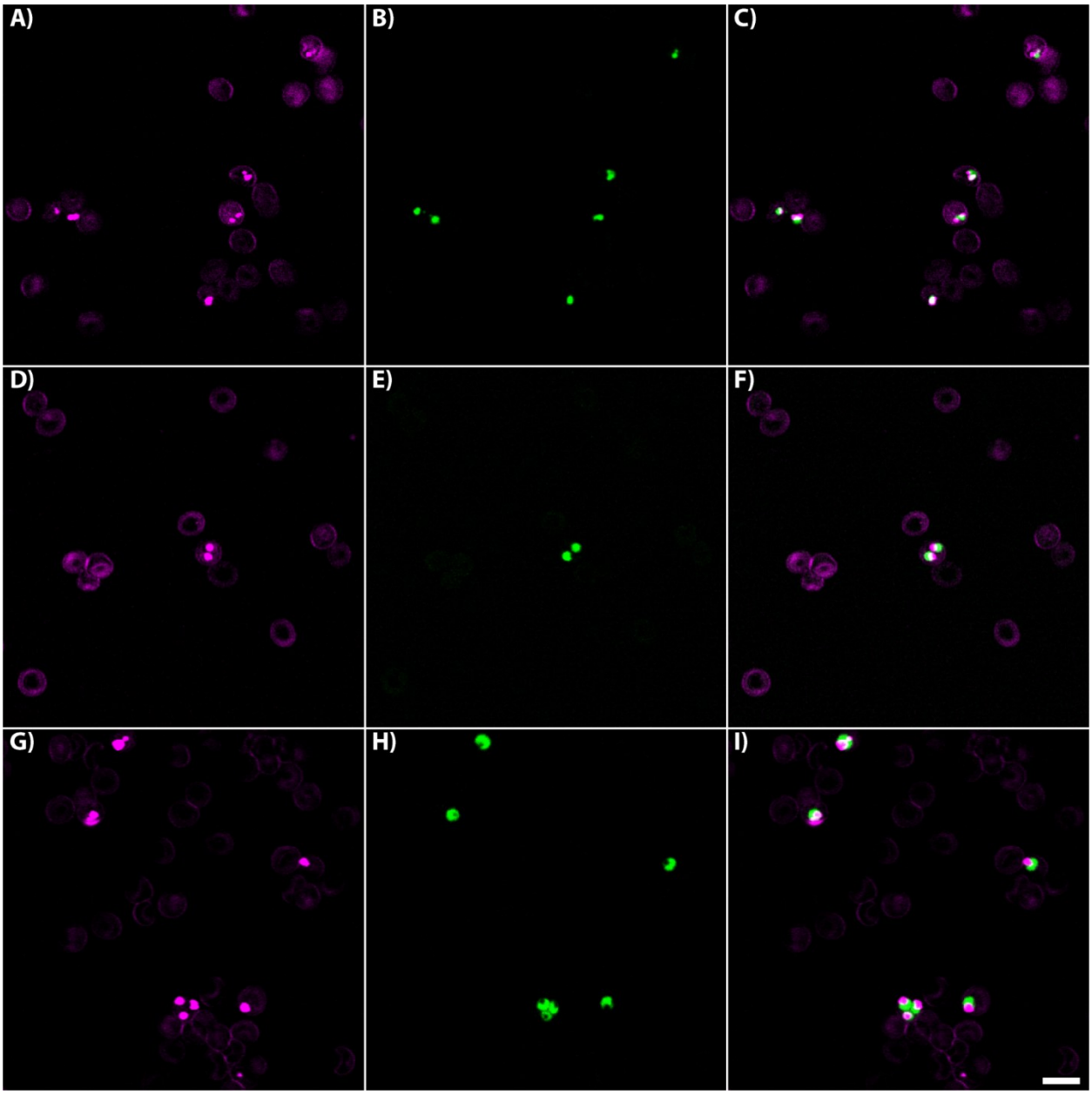

Figure A-2: Validation of method performance using acridine orange nuclear staining on cultured *P. falciparum* parasites at the: A)-C) Ring, D)-F) Trophozoite, and G)-I) Schizont stages. Magenta: THG signal, Green: TPF acridine orange. Scale bar: 10 μm.

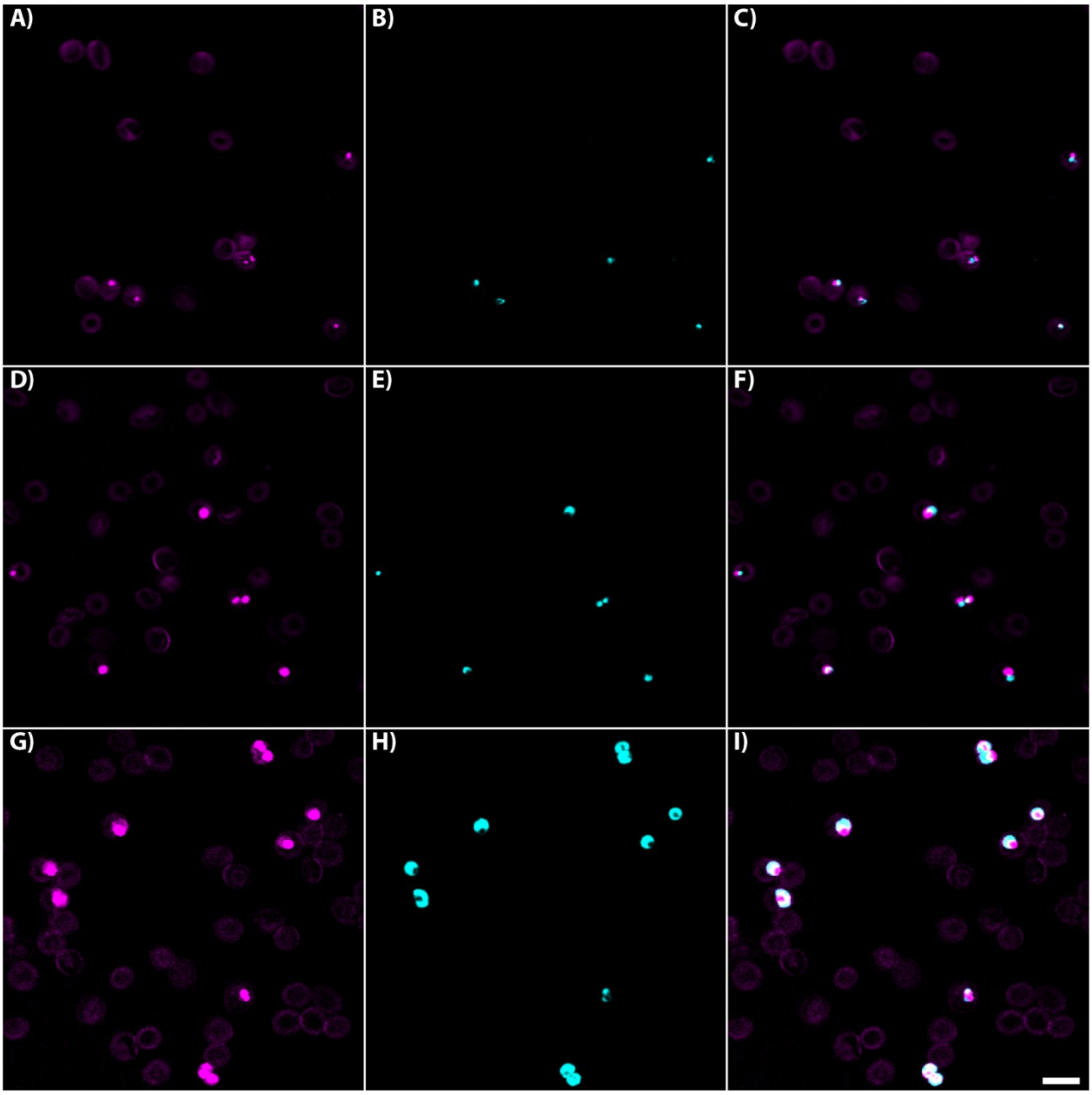

Figure A-3: Validation of method performance using DAPI nuclear staining on cultured *P. falciparum* parasites at the: A)-C) Ring, D)-F) Trophozoite, and G)-I) Schizont stages. Magenta: THG signal, Cyan: TPF DAPI. Scale bar: 10 μm.